AIAA Undergraduate Team Aircraft Design Competition

Final Design Report

Team Gunbus

University of Illinois at Urbana-Champaign

AE 443: Aircraft Systems Design

Submission Date: May 14th, 2021

Figure 1: Team Gunbus

Table 1: Team Member Contributions

Team Member	**Primary Discipline(s)**	**Secondary Discipline(s)**	**AIAA Number**	**Signature**
Drake Dutz	Team Lead & Mass Properties	Interior Design	905777	
Tanner Hoyt	Aerodynamics	Avionics	1230162	
Vera Liu	Structures	Loads & Dynamics	905874	
Gabriel Aaron	Propulsion	Landing Gear	1036610	
Eric Moy	Performance	Cost & Ordnance	1230331	
Patryk Sokolowski	Stability and Control	Acoustics	1229832	
Jacob Crow	Systems	Configuration & Certification	1230128	
Jason Merret	Faculty Advisor		155270	

Contents

Acronyms

AC = Aerodynamic Center
AIAA = American Institute of Aeronautics and Astronautics
APU = Auxiliary Power Unit
AR = Aspect Ratio
BL = Butt Line (Station Coordinate)
CAD = Computer-Aided Design
CFD = Computational Fluid Dynamics
CFRP = Carbon Fiber Reinforced Plastic
C.G. = Center of Gravity
CRICM = Common Infrared Countermeasures
dB = Decibels
DRR = Design Readiness Report
ESHP = Equivalent Shaft Horsepower
EBHA = Electrical Back-up Hydraulic Actuator
FADEC = Full Authority Digital Electronic Control
FBW = Fly By Wire
FOD = Foreign Object Damage
GFRP = Glass Fiber Reinforced Plastic
KEAS = Knots, Equivalent Airspeed
KTAS = Knots, True Airspeed
MPH = Miles Per Hour
MPU = Micro Power Unit
MTOW = Maximum Takeoff Weight
NACA = National Advisory Committee for Aeronautics
PDR = Preliminary Design Report
PRSOV = Pressure Relief Shut-off Valve
P&WC = Pratt & Whitney Canada
RFP = Request for Proposal
SFC = Thrust-Specific Fuel Consumption
SHP = Shaft Horsepower
SOV = Shut-off Valve
SR = Speed Range
TOC = Top of Climb
TOFL = Takeoff Field Length
UIUC = University of Illinois at Urbana-Champaign

Nomenclature

$\frac{C}{4}$ = Quarter Chord
α = Angle of Attack
C_D = Drag Coefficient
C_{D_0} = Zero-lift Drag Coefficient
C_{D_i} = Induced Drag Coefficient
C_L = Lift Coefficient, finite span wing
c_l = Lift Coefficient, infinite span wing
C_M = Moment Coefficient, finite span wing
c_m = Moment Coefficient, infinite span wing
L/D = Lift to Drag Ratio
λ = Wing Taper Ratio
δ_{Flap} = Flap Deflection Angle
q = Dynamic Pressure
S_{wet} = Wetted Area
S_{ref} = Reference Wing Area

List of Figures

List of Tables

Executive Summary

This report presents team Gunbus's final design for a light attack aircraft in response to the 2021 AIAA Undergraduate Team Aircraft Design RFP. Motivation for this request arose during the wars in Iraq and Afghanistan, where expensive, highly advanced fighters were used to eliminate relatively minor threats. There was a clear disconnect between what aircraft were needed and what was available. The project objective is to design an affordable light attack aircraft capable of providing close air support on short notice. The aircraft must be able to takeoff and land on austere fields and complete some missions only feasible by attack helicopters.

More specifically, the aircraft shall takeoff and land over a 50 ft obstacle in less than 4,000 ft when operating from austere fields at density altitude up to 6,000 ft. This must be accomplished while carrying at least 3,000 lb of armament, an integrated gun, and two crew members. Performance requirements include a service ceiling above 30,000 ft and a service life of 15,000 hours over 25 years. Other considerations include survivability, overall value, mission flexibility, and provisions to carry additional weaponry.

The proposed aircraft design is the result of a multidisciplinary effort between Gunbus's seven UIUC Aerospace Engineering undergraduate students. The final aircraft configuration includes a single fuselage design, powered by two wing mounted PT6 turboprop engines. The wing is low mounted with an AR of 8.1. The wingspan is 45 ft, and the aircraft MTOW is 14,447 lb. The tail is chosen to be conventional, similar to that of the baseline aircraft, the Embraer Super Tucano. Initially, the Super Tucano appeared to be a satisfactory candidate for the RFP, but a closer look shows it lacks in performance, service life, and ability to perform some missions only attack helicopters can. The proposed aircraft is designed to exceed the baseline in performance, reliability, payload capacity, and overall value. The current cost is $22,962,000 per aircraft for production of 250 aircraft, but the cost varies significantly based on the amount produced.

To achieve this objective, team Gunbus broke down the design process into three sections. The first section was conceptual design, in which the major aircraft characteristics were chosen. The second section was preliminary design, where most of the design work resided. The third section was detailed design, in which the design was heavily analyzed and design parameters were fine tuned. This process reflected common industry practice and allowed team Gunbus to set intermediate goals and ultimately design an aircraft which satisfied all RFP requirements and objectives.

Figure 2: Gunbus Aircraft

1 Introduction

1.1 Background Information

Light attack aircraft are capable of finding, tracking, and attacking targets to support ground forces for purposes such as counter-insurgency, reconnaissance, and ground attack. The Vietnam War and the Korean War from the 1950's to the 1970's posed geographical and environmental challenges in terms of air defense, which fueled the requirements for light attack aircraft to account for "jungle fighting" versatility. In contrast to the realities from the 20th century, modern day air combat is no longer dominated by air-to-air combat. Innovation in technology has enabled the defense industry to deliver more capable and efficient aircraft. Air defense is elevated by electronic warfare and highly-maneuverable, network-capable technology [3].

1.2 Motivation and Objectives

The motivation for this design project is to design an affordable, light attack aircraft that can operate from short, austere fields near the front lines and perform missions that are currently only feasible with attack helicopters. Today's missions still demand a highly maneuverable aircraft that can loiter and fly at low speeds, enabling the pilots to visually acquire a target and attack effectively. Light-attack aircraft can operate on remote airstrips with little maintenance. The U.S. Air Force's goal is to acquire an affordable light-attack plane optimized for these types of missions [4].

1.3 Design Philosophy

The preliminary design stage involves extensive market research and trade studies of existing light attack aircraft designs that meet the requirements similar to that of the AIAA design competition. Similarity analysis conducted on the Rockwell OV-10 Bronco and the Embraer 314 Super Tucano provides the team with historical data and calculations that helped to construct a baseline for the aircraft design. From these similarity analyses, the Gunbus team arrived at a conceptual design to iterate and improve upon. The goal of this design project is to produce an innovative design that incorporates the strengths of existing aircraft with emerging technologies that will enhance the aircraft performance and capabilities.

2 Concept of Operations

2.1 Requirements

Alongside the designated mission profiles, a set of requirements have been given in the AIAA RFP. In the table below, these requirements are listed along with recommended objectives. Team Gunbus placed high importance on meeting both the requirements and objectives when designing the aircraft. In addition to the requirements in the RFP, the Gunbus team shall meet other requirements that will be derived at the system level to increase fidelity in the performance and overall aircraft design.

Table 2: RFP General Requirements

Type	Description
Requirement	Austere Field Performance: Takeoff and landing over a 50 ft obstacle in 4,000 ft when operating from austere fields at density altitude up to 6,000 ft with semi-prepared runways such as grass or dirt surfaces with California Bearing Ratio of five
Requirement	Payload: 3,000 lb of armament
Requirement	Integrated gun for ground targets
Requirement	Service life: 15,000 hours over 25 years
Requirement	Service ceiling: 30,000 ft
Requirement	Crew: Two, both with zero-zero ejection seats
Requirement	The aircraft shall be able to descend from cruise altitude to loiter altitude within 20 minutes of climb initiation
Requirement	Perform the design mission laid out in the RFP
Requirement	Perform the ferry mission laid out in the RFP
Requirement	Aircraft shall accommodate enough reserve fuel so that the aircraft is capable of climbing to and maintaining loiter altitude for 45 minutes
Objective	Survivability: Consideration for survivability, such as armor for the cockpit and engine, reduced infrared and visual signatures, and countermeasures (chaff, flares, etc.)
Objective	Provisions for carrying/deploying a variety of weapons, including rail-launched missiles, rockets, and 500 lb (maximum) bombs
Objective	Design should be certifiable for military standard airworthiness (MIL-STD-516C) and consistent with guidance provided in the Joint Service Specification Guides (JSSGs)

2.2 Mission Profiles

As a light attack aircraft, the primary mission will be to conduct close air support missions on enemy troops, vehicles, shelters, and possibly other aircraft. The design mission that has been presented in the RFP is illustrated below in Figure 3. This design mission includes the capability of carrying ordnance for a required distance, loitering on site for a designated time, and then returning to base without deploying stores. As an additional measure for mission and safety assurance, the aircraft should also carry enough reserve fuel to loiter for some time before consuming all usable fuel. Furthermore, the aircraft should be able to conduct a ferry mission in which the aircraft can cruise a longer distance without conducting a mission along the way. An example of this is moving the aircraft from one base to another. In order to draft a sound proposal, it is required to meet every component of these mission profiles.

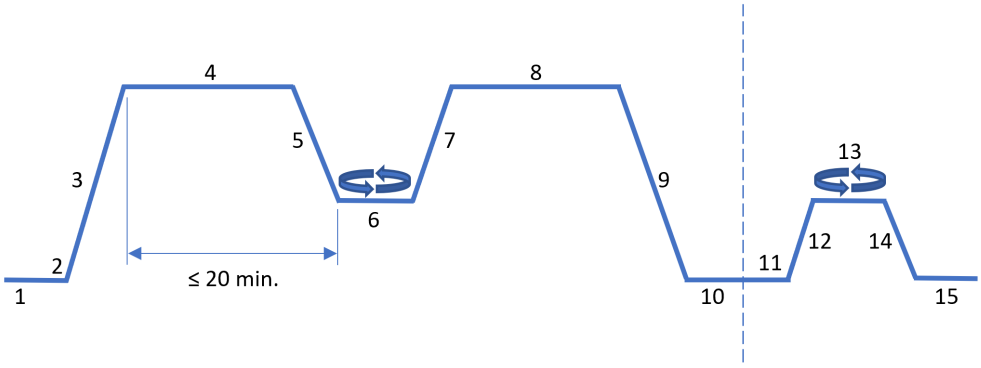

Design Mission
1. Warm Up / Taxi [5 min.]
2. Take Off [50 ft Obstacle, ≤ 4,000 ft]
3. Climb [≥ 10,000 ft]
4. Cruise [100 nmi]
5. Descent [3,000 ft]
6. Loiter [4 hours]
7. Climb [≥ 10,000 ft]
8. Cruise [100 nmi]
9. Descent / Landing [50 ft obstacle, ≤ 4000 ft]
10. Taxi / Shutdown [5 min.]

Reserve Mission
11. Take Off [50 ft Obstacle, ≤ 4,000 ft]
12. Climb [3,000 ft]
13. Loiter [45 min.]
14. Descent / Landing [50 ft obstacle, ≤ 4000 ft]
15. Taxi / Shutdown [5 min.]

Figure 3: Profile of the Design Mission

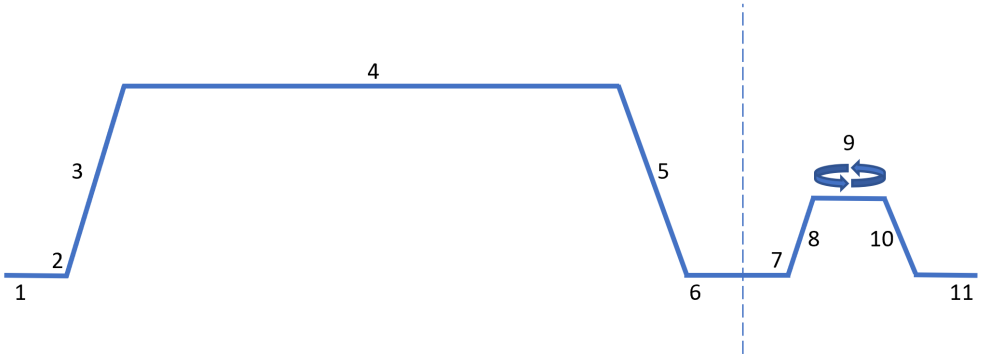

Ferry Mission
1. Warm Up / Taxi [5 min.]
2. Take Off [50 ft Obstacle, ≤ 4,000 ft]
3. Climb [≥ 18,000 ft]
4. Cruise [900 nmi, best range speed]
5. Descent / Landing [50 ft obstacle, ≤ 4000 ft]
6. Taxi / Shutdown [5 min.]

Reserve Mission
7. Take Off [50 ft Obstacle, ≤ 4,000 ft]
8. Climb [3,000 ft]
9. Loiter [45 min.]
10. Descent / Landing [50 ft obstacle, ≤ 4000 ft]
11. Taxi / Shutdown [5 min.]

Figure 4: Profile of the Ferry Mission

3 Sizing Analysis

3.1 Similarity Analysis

The initial step when conducting the similarity analysis was to research successful current and past light attack aircraft, which operated on a variety of propulsion systems (turbojet, turbofan, turbofan with an afterburner, and turboprop). After gathering preliminary performance data, a spreadsheet was created to catalog and compare the different aircraft and their propulsion systems. The aircraft requirements listed above in Section 2 were extracted from the Excel spreadsheet and were used to choose the seed aircraft. Using historical data and the data shown below in Table 3, it was determined that the turbofan and turboprop engines were most efficient. Therefore, a closer analysis of these two systems was conducted. In the end, the turboprop aircraft, the Super Tucano, was chosen as the seed aircraft due to its high performance on austere fields and at lower air speeds when compared to the A-10. Additionally, the Super Tucano configuration provided more structural efficiency and less drag when compared the OV-10 Bronco.

Table 3: Sizing Analysis

Aircraft	Propulsion System	TOFL, ft	Payload, lb	Service Life, hr	Service Ceiling, ft	Crew
MB-339[5]	Turbojet	1,805	4,000	10,000	46,000	1
OV-10 Bronco[6][7]	Turboprop	2,799	3,702	3,000	26,000	2
Super Tucano[8]	Turboprop	2,950	3,417	12,000	35,000	2
A-10[9][10]	Turbofan	3,937	16,000	12,000	45,000	1
HAL Tejas[11]	Turbofan w/ afterburner	5,577	11,700	10,000	50,000	1
Aero L-159[12]	Turbofan	2,231	5,159	8,000	43,300	1

Exceeds Given Requirement
Below Given Requirement

3.2 Aircraft Sizing

Once the Super Tucano was chosen as the seed aircraft, the initial sizing parameters listed below in Table 4 were defined. The initial parameters for the wingspan and fuselage length were chosen while referencing the Super Tucano. The wing span and fuselage length of the Super Tucano were increased in order to accommodate a twin engine configuration. The increase in size would also allow the team to place more armament under the wings. Using the described requirements, the values for the payload weights, along with the range and balance field length, were determined. For this aircraft sizing, the PT6A-135A engine was chosen, further explained in Section 5, and a fixed-engine sizing was completed. Unlike a rubber engine sizing, the thrust and weight of the engine was known. As shown in Table 4, the parameter values that were chosen for the preliminary configuration are similar to the values that are currently used for the configuration of the aircraft.

Table 4: Sizing Parameters

Parameter	Initial Configuration Value	Preliminary Configuration Value
Fuselage Length	40 ft	40 ft
Wing Span	40 ft	45 ft
Payload Margin	3,000 lb	3,000 lb
Empty Weight	7,055 lb	6,929 lb
Range	1,000 nmi	1,000 nmi
Balance Field Length	3,900 ft	3,174 ft
Takeoff Thrust	1,323 lbf	1,323 lbf

Using the sizing parameters and a constraint diagram, the aircraft's preliminary configuration was calculated for a variety of aspect ratios and wing areas. After analyzing the fuel weight, empty weight, and max ramp weight plots, the aircraft's aspect ratio and wing area were selected. These values were determined by choosing a configuration which not only increased the available max ramp weight, but also decreased the fuel and empty weights. The constraint diagram was especially useful for choosing a wing area and is shown in Figure 5. However, the team chose not to design for the lowest HP/W as the engine was fixed and the aircraft weight would potentially increase as the design process progressed.

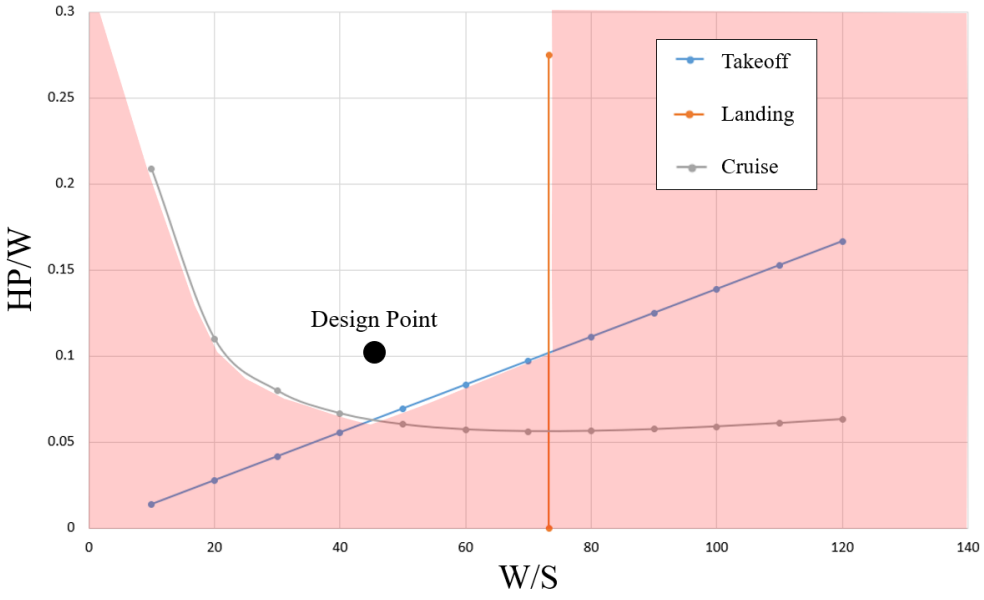

Figure 5: Constraint Diagram

The max L/D was calculated by using the XFLR5 airfoil analysis tool and was compared to to the value calculated within the sizing spreadsheet. Since the values were similar, this signified that the team's calculations were correct. The key preliminary parameters are listed below in Table 5. After further analysis

and changes to the aircraft configuration, the initial parameters of the aircraft changed and the current configuration parameters are discussed in Section 4.

Table 5: Preliminary Sizing Results

Parameter	Value
Aspect Ratio	6.4
Wing Area	250 ft^2
L/D	14.12
C_{Lmax}	1.6
Empty Weight	6,500 lb
Fuel Weight	1,500 lb
Max Ramp Weight	11,000 lb

3.3 Trade Studies

The trade studies listed below were conducted with preliminary design ideas that were created during the beginning of the aircraft design process. For the first trade study, the empty, fuel, and max takeoff weights were compared between a twin engine, conventional aircraft and a twin engine, twin boom aircraft. In order to obtain the plot that is shown below in Figures 4, rubber engine sizing was used. The aircraft's parameters, such as wing span, engine thrust, fuselage length, and max payload weight, were kept consistent to compare the two aircraft configurations. To account for the extra surfaces on the twin boom configuration, the area and weight approximations of the twin booms were included in the wetted area and fuselage weight calculations. After calculating the sized aircraft for a variety of aspect ratios and wing areas, the difference between the weights of the different configurations was calculated. On average, the twin boom had a 6.55% lighter empty weight and a 6.27% lighter max takeoff weight, but it had a 6.06% heavier fuel weight. Using the lower fuel weight and max takeoff weight data, along with historical data it was determined that the conventional twin engine configuration was more efficient and better suited for the presented requirements.

The second trade study was used to compare a twin and a single engine conventional aircraft. For this trade study, the key parameters: engine thrust and max payload weight were kept the same to determine the difference in weights of the designed single and twin engine aircraft. Similar to the first trade study, a rubber engine was used to size the aircraft and the resulting empty, fuel, and max takeoff weights were plotted, as shown in Figure 5, with varying wing areas and aspect ratios. After comparing the two figures, it was calculated that on average the twin engine configuration had a 3.44% heavier empty weight, a 10.25% heavier fuel weight, and a 5.88% heavier max takeoff weight. For this project a double engine configuration was

chosen despite the extra weight because it provides redundancy increasing the survivability of the aircraft.

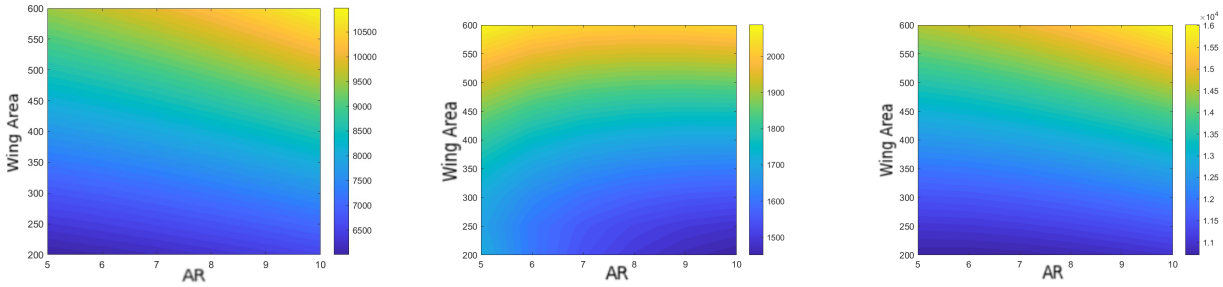

(a) Empty Weight, lb (b) Fuel Weight, lb (c) Max Takeoff Weight, lb

Figure 6: Twin Engine, Conventional Aircraft Configuration

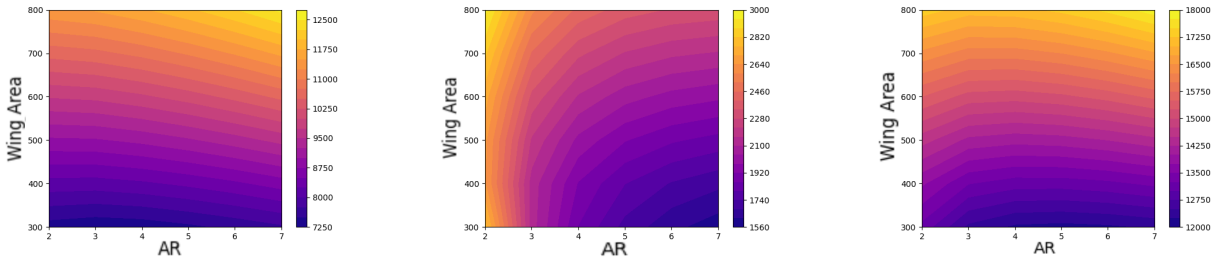

(a) Empty Weight, lb (b) Fuel Weight, lb (c) Max Ramp Weight, lb

Figure 7: Single Engine, Conventional Aircraft Configuration

4 Configuration

4.1 Considered Configurations

Shown below in Figure 8 are the four configurations that were heavily considered in the sizing and qualitative analyses. The primary configuration option considered were a low wing with a single engine, a low wing with a twin engine, a high wing with a single engine, or a high wing with a twin engine.

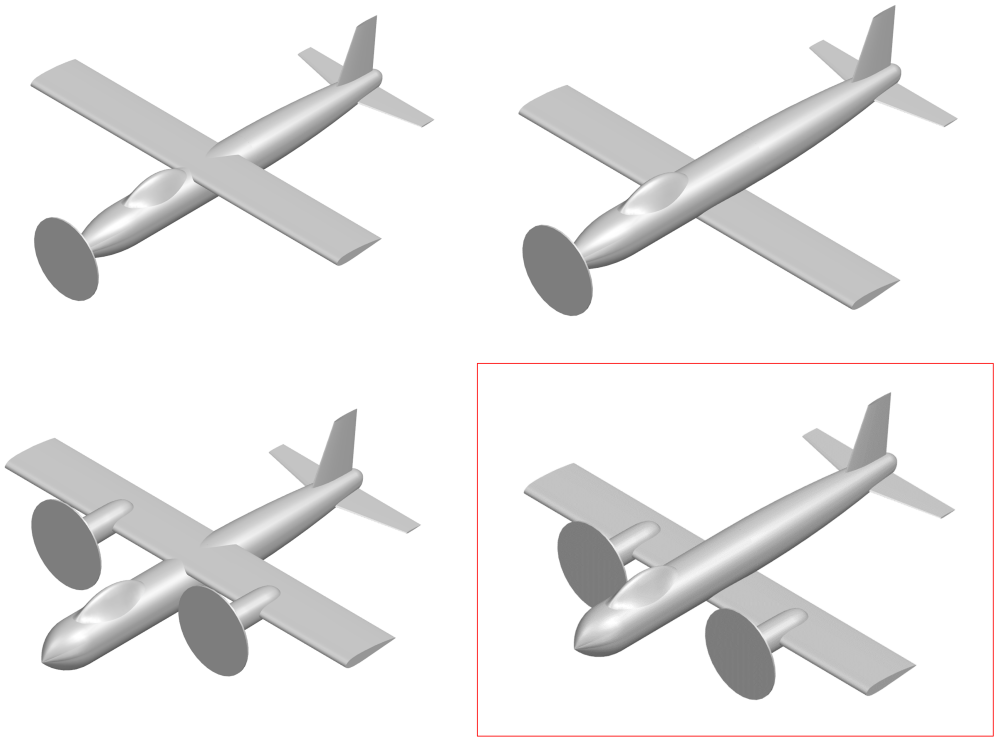

Figure 8: Configurations considered in early design

4.2 Configuration Rationale

After going through the initial similarity and sizing exercises, a baseline configuration for the aircraft could be determined through quantitative and qualitative analysis. A trade study was conducted for a twin-boom aircraft but eventually ruled out quantitatively, which was discussed in Section 3, and qualitatively. For the twin-boom design, there were no apparent benefits to performance while also creating increased structural complexity. Additionally, concerns for survivability in the case the a single boom is lost helped to rule out the twin-boom configuration. After deciding on the single boom design, the next factor for consideration was the number of power sources. Using the sizing and performance analyses, it was determined that both options could meet the requirements for an aircraft slightly larger than the Super Tucano. For the aircraft engines, a single nose mounted engine or two wing mounted engines were considered. A second engine allows for continued thrust as well as electrical power production due to another engine generator. The disadvantages for this configuration include more maintenance and higher initial cost due to having two engines. In the end, the twin-engine configuration was chosen due to the desirability of having continued power in case of engine failure given the likely hostile environments that the aircraft will face. For the tail configuration, a conventional tail was chosen because the control surfaces are centrally located, out of the path of the

propeller wash. Also, the conventional tail was chosen over a T-tail and cruciform tail as it is easier to manufacture. Lastly, a V-tail was ruled out due to it being a more complex system of control due to both surfaces providing pitch and yaw. Additionally, and most overwhelmingly, the V-Tail was ruled out due to a history of unreliability as well as a compromise in safety. The wing placement was chosen as a low wing for a variety of factors, one being that a high wing would add weight to the aircraft due to additional structural support. Important benefits of a low wing that were considered were shorter landing gear, which leads to weight savings, as well as better take-off performance due to ground effect. Some draw backs of a low wing include potentially less visibility and a decrease in in-flight stability. Lastly, the landing gear configuration was determined to be a tricycle configuration with the forward gear under the nose and the two rear gear housed under the engine cowlings on the wings. This configuration was chosen because it provides stability on the ground, better visibility, and utilizes wing space by putting the gear in a position that could not be used as a hard-point in the twin-engine configuration. The placement and design of the landing gear will be discussed later in Section 9.4.

4.3 Final Configuration

The current configuration of the aircraft is shown below in Figure 9, as well as the important dimensions of the aircraft. The current configuration is similar to that of the baseline with no major configuration changes. The current version includes refinement such as preliminary structural design, ordnance configuration, engine integration, systems and a detailed outer mold line. The overall configuration of the aircraft will not change in the future and any further work will be left for analysis and design verification.

Table 6: Notable Configuration Parameters

Parameter	Value
Wingspan	45 ft
Length	38 ft 8 in.
Wing Area	280 ft^2
Aspect Ratio	7.23
Root Airfoil	NACA 4415
Tip Airfoil	NACA 4412
Height	14 ft 8 in.
C/4 Sweep	-1.59 deg
Mean Chord	76 in.
Taper Ratio	0.667
Wing MAC	6 ft 4 in.
Horizontal Tail Area	83.05 ft^2
Vertical Tail Area	35.61 ft^2

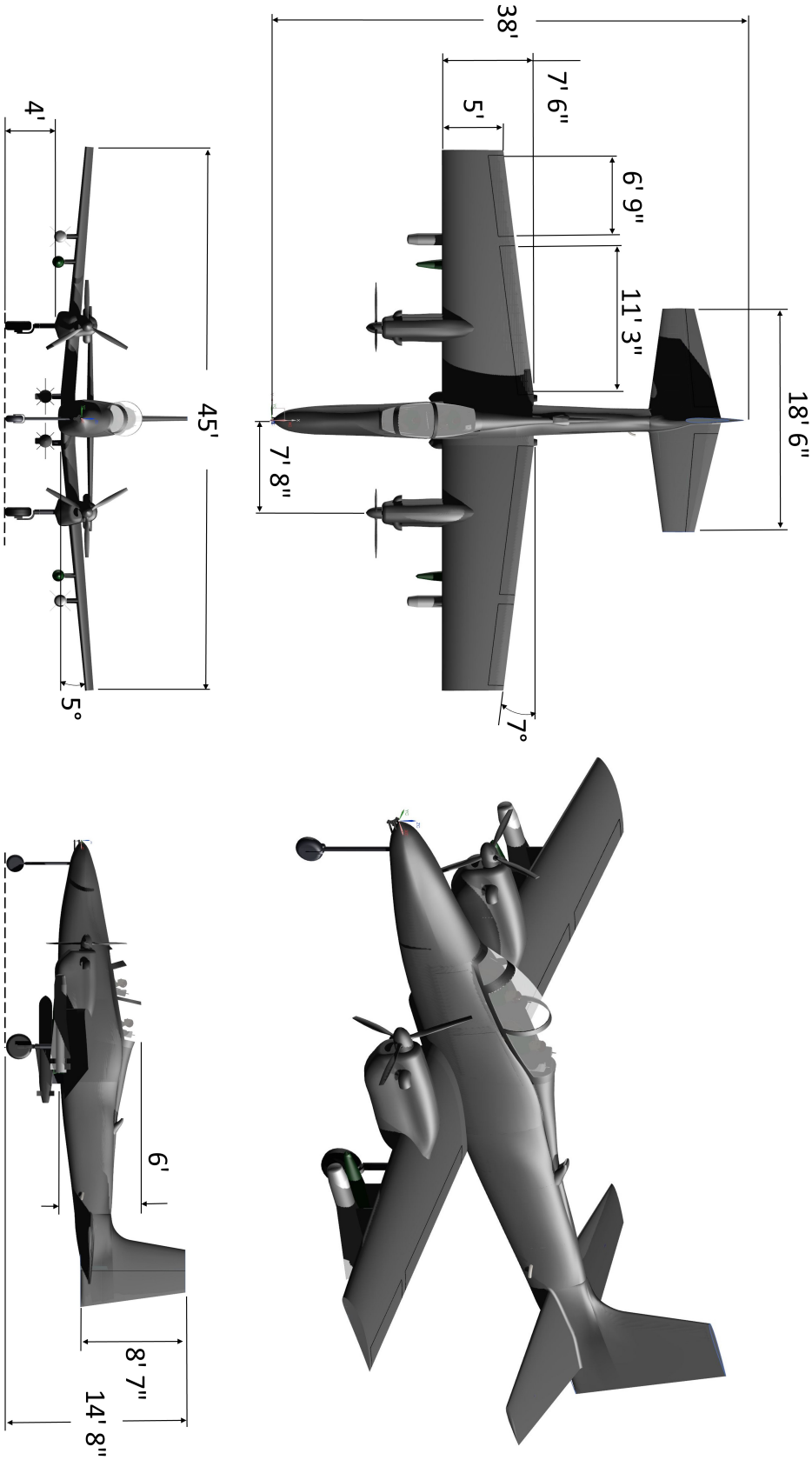

Figure 9: FDR Configuration 3-View

4.4 Internal Configuration

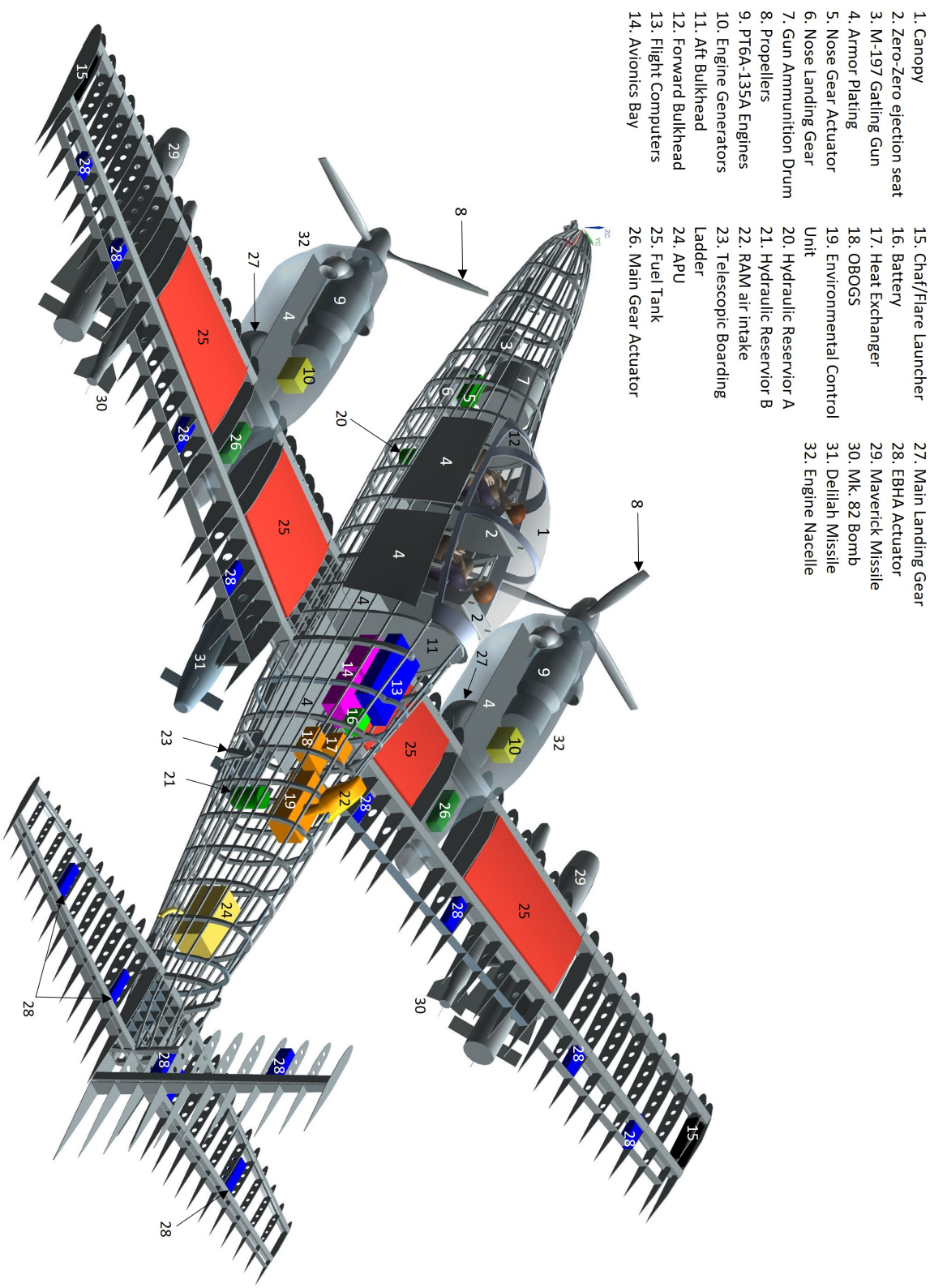

Figure 10: Aircraft Internal Configuration

4.5 Flight Deck Configuration

The aircraft interior is focused primarily on functionality, and the layout is loosely based on the Super Tucano. Multifunction displays and joystick control are compact, making them a good choice for the limited cockpit space. Two Martin Baker US16T ejection seats are chosen for the crew, satisfying the requirement for zero-zero ejection. The interior layout is shown below in Figure 11.

1. Head-up display
2. Armament panel
3. Stand-by instruments
4. Multifunction display
5. Central display
6. Landing gear controls
7. GPS
8. Autopilot director
9. Engine controls
10. Joystick
11. Environmental controls
12. Rudder Pedal
13. Fuel panel
14. Audio selection panel
15. Exterior lights
16. Miscellaneous controls

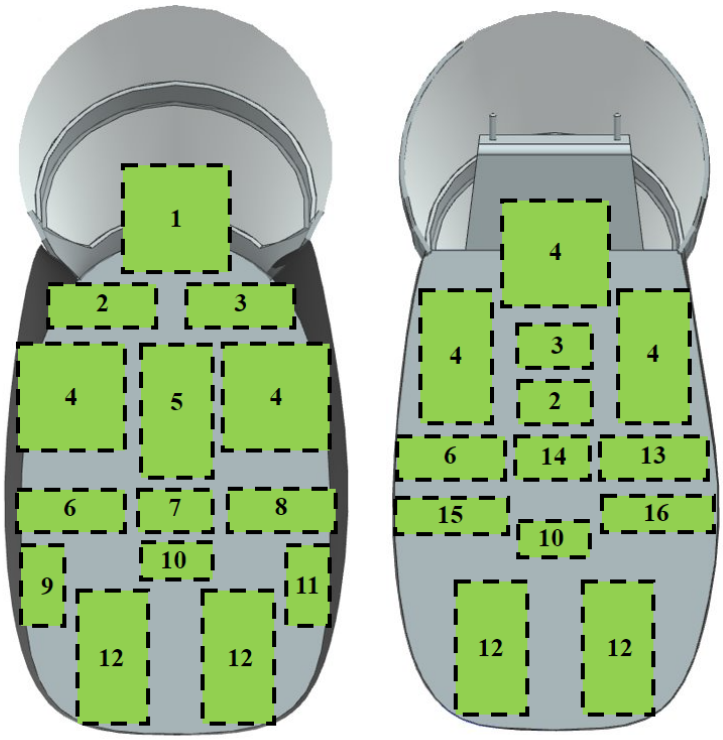

Front Instrument Panel Rear Instrument Panel

Figure 11: Cockpit Layout

Another consideration for the interior design was to ensure the pilot viewing angles were adequate. The team managed to exceed the goal of an 11 degree frontwards viewing angle, as the viewing angle is currently set to 13.5 degrees. This angle could be further increased by lowering the aircraft's nose, but doing so would increase the risk of having visibility issues caused by the integrated gun's smoke. Additionally, the side viewing angle is 15 degrees and primarily limited by the engine. Overall, both angles exceed the requirements and are shown in Figures 12 and 13.

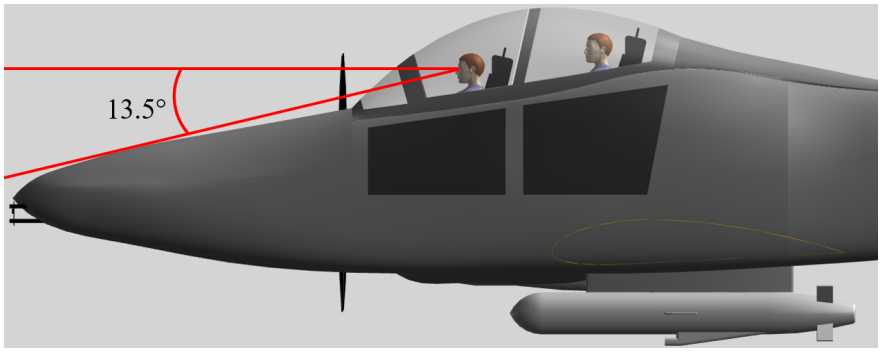

Figure 12: Frontwards Viewing Angle

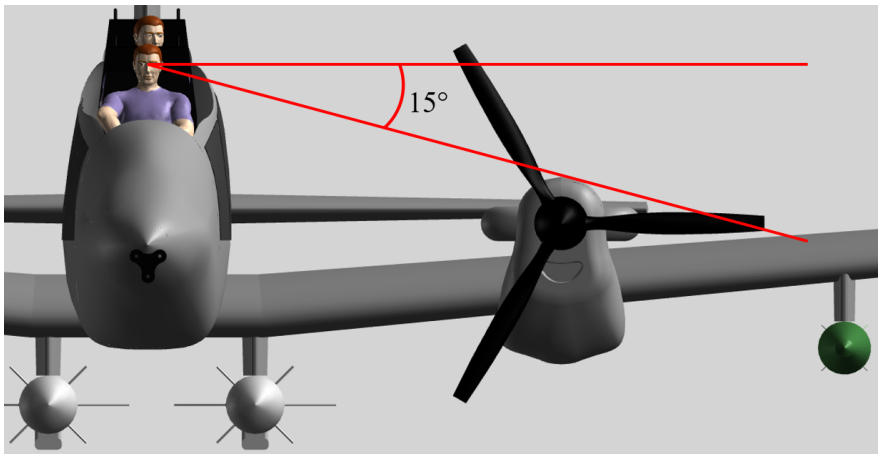

Figure 13: Side Viewing Angle

5 Propulsion

5.1 Propulsion Philosophy

Our similarity analysis on the light attack role revealed that turbojet and turboprop engines were most commonly used. From analysis, both engine types could theoretically work for our application, but it was decided that a turboprop engine would better satisfy the conditions imposed in the RFP. When it comes to cost, turboprop engines are on average cheaper to operate than turbojets. This is not only because they burn less fuel, but also because there are overall less moving parts, making them more reliable and less expensive to maintain. They are also more suited to austere environments, with turbojets usually needing longer paved runways and being more conducive to the ingestion of FOD. While it is possible to prevent FOD ingestion in turbojet engines, it may add weight or necessitate a change in configuration. In terms of efficiency, turboprops are more efficient than any other type of propulsion for our design velocity range, which includes the "low-and-slow" flight common to attack helicopters. The only major trade off is flight

altitude. Whereas a turboprop engine usually has a service ceiling of around 30,000 ft, a turbojet can maintain efficiency higher up in the flight levels. However, the RFP only dictates a minimum service ceiling of 30,000 ft, so a turboprop engine was considered appropriate for this specification. Electric propulsion was briefly considered but ruled out for several reasons. The main adverse factors were the weight of all the necessary systems, as well as the complexity of repairing a module in the field, especially where reliability and ease of maintenance are of significant importance.

As previously mentioned, a twin engine configuration was selected over a single engine for several reasons. One benefit is the improved safety thanks to the redundancy in propulsion. Given **P**, the probability that one engine fails during flight, the probability that one of the two installed engines fail is **2P**. However, the probability that both engines experience a failure is reduced to $\mathbf{P^2}$. According to Gerzanics [13], the PT6 family of engines has suffered less than one engine failure per 651,126 flight hours, on average. Assuming the events are independent, the engine failure probabilities for design and ferry missions based on historical data are summarized in Table 7 below.

Table 7: Failure Probabilities

Failure of:	1 of 1 Engines	1 of 2 Engines	2 of 2 Engines
Theoretical:	**P**	**2P**	$\mathbf{P^2}$
Per Flight Hour:	0.00015 %	0.0003 %	2.4×10^{-10} %
Design Mission:	0.00083 %	0.0017 %	1.3×10^{-9} %
Ferry Mission:	0.00081 %	0.0016 %	1.3×10^{-9} %

Do note that these are idealized probabilities, and that they do not account for extreme factors such as combat damage. The probability of a single engine failure in a twin configuration may be higher than in a single engine configuration, but the advantage of this redundancy is that the aircraft can still fly back to base on only one engine. This added safety measure is critical to the survivability of our aircraft.

5.2 Engine Selection

Table 8: Engine Candidates

Model	Application	Power, hp	SFC / hr	Weight, lb
P&WC PT6A-25C [14]	Embraer Tucano	750	0.595	355
P&WC PT6A-135A [14]	Cessna Conquest	750	0.585	347
P&WC PT6A-66 [15]	Piaggio P.180 Avanti	850	0.62	456
Honeywell TPE331-10 [16]	North American OV-10 Bronco	940	0.534	385

To choose an appropriate propulsion system for our given missions, a similarity analysis of turboprop engines was conducted using engines with mostly similar use cases. Of the four candidates, three are Pratt & Whitney Canada PT6 variants due to its wide use and popularity for both civilian and military applications. While the -25C and -135A have small form factors, the -66 and Honeywell TPE331 series are larger and more powerful, despite the latter having the lowest Specific Fuel Consumption (SFC) of all those in contention. Following preliminary performance calculations, it was determined that 750 HP per engine was largely sufficient to satisfy the Austere Field Performance requirement. Therefore, the PWC PT6A-135A was selected over the other candidates for its higher efficiency and lower dry weight compared to the similarly sized -25C.

The FAA-certified power ratings and specifications for the PT6A-135A can be seen in Table 9. From this data, basic performance charts such as the available power at various altitudes and average SFC were plotted over a range of airspeeds (see Figures 14 and 15). These were obtained by scaling similar charts from McCormick [17] for an engine in the same family.

Table 9: PT6A-135A Engine Specifications

Parameter	Value
Maximum Continuous SHP (ESHP) @ Sea Level [14]	750 (787)
Takeoff SHP(ESHP), 5 min. @ Sea Level [14]	750 (787)
Maximum Reverse SHP [14]	720
Maximum Envelope Length, in. [18]	62
Maximum Envelope Diameter, in. [18]	19

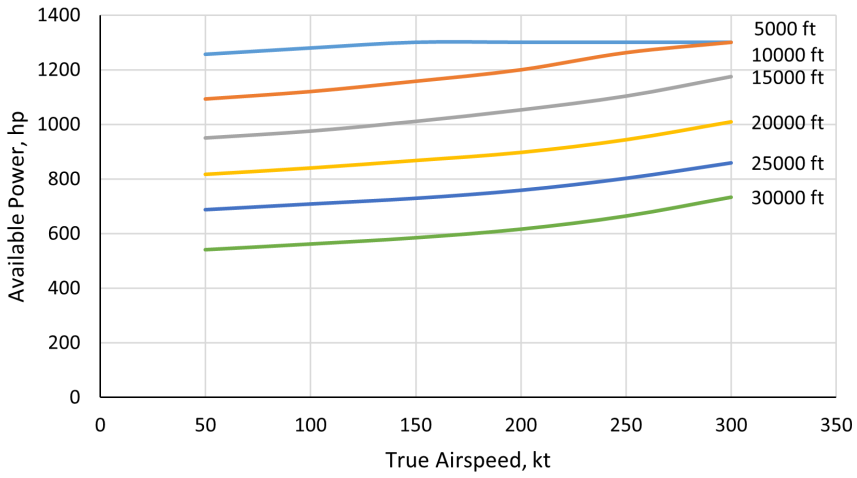

Figure 14: PT6A-135A Available Power vs. True Airspeed

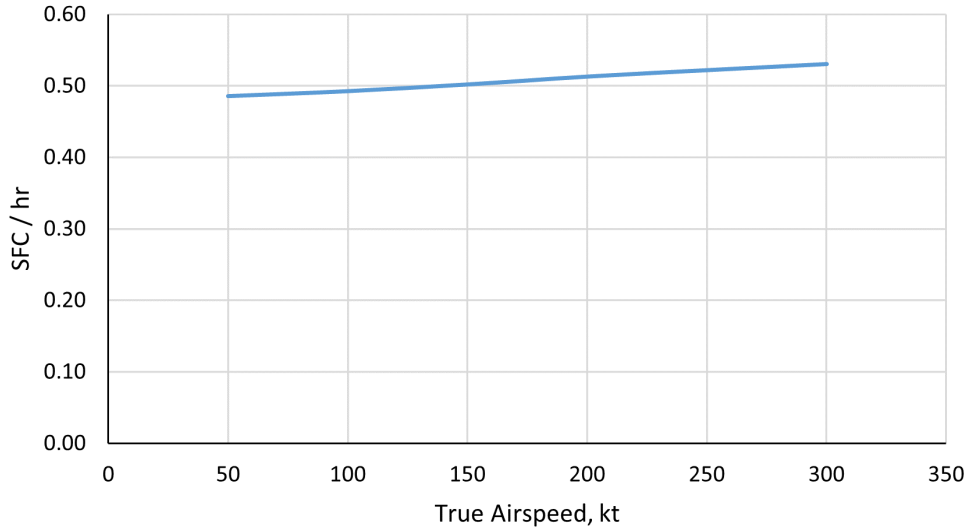

Figure 15: PT6A-135A Averaged SFC vs. True Airspeed

5.3 Engine Installation

The engines are housed in nacelles, which are designed to house all the necessary components and accessories. The nacelles straddle the wing structure at BL 92 (92 inches outboard from centerline) to allow for at least 20 inches of clearance with respect to the fuselage. The engine is mounted slightly above the forward wing spar, leaving enough spacing for an air inlet between the engine block and the gear stowage area. The inlet makes it way under the engine and brings air into the engine's intake, which is located at its rear. The intake features a thin mesh to prevent any FOD from entering the compressor stage and damaging interior components. The PT6A expels air through exhausts pipes on either side, providing an additional 93 lb. of jet thrust. These exhausts have an added benefit of propelling high-speed air onto the upper wing surface, generating supplementary lift. Side and front views of the nacelle, along with the interior layout, can be seen in Figures 16 and 17.

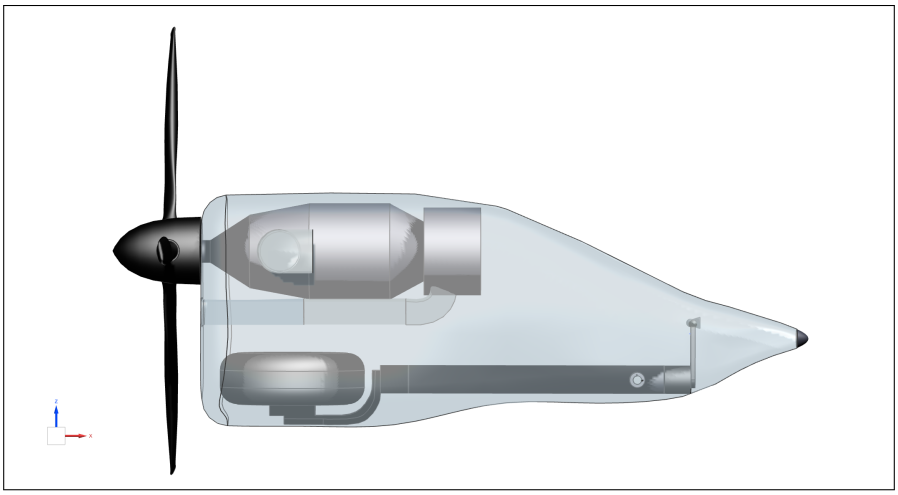

Figure 16: Nacelle Side View

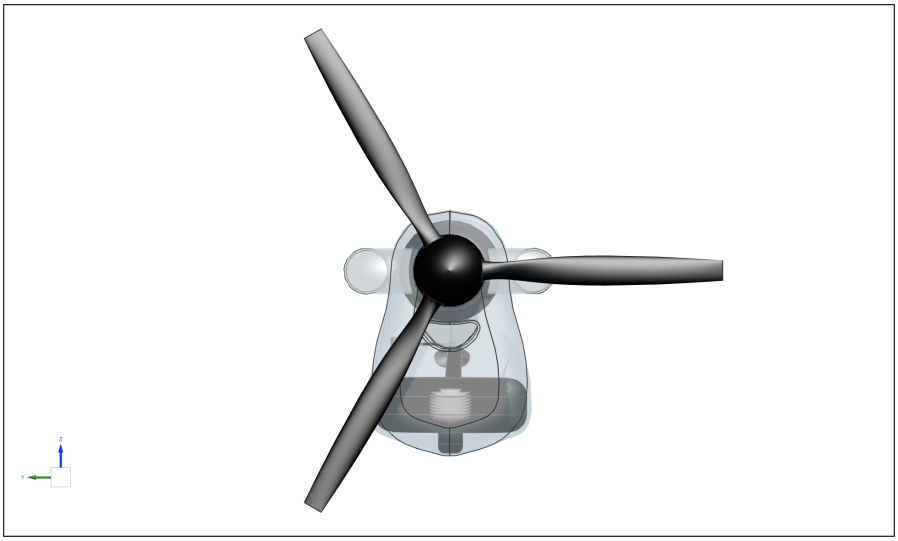

Figure 17: Nacelle Front View

5.4 Propeller Selection

Typically, a long two-bladed propeller is considered to be most efficient. However, given the fuselage and ground clearance restrictions, it was determined that a three-bladed propeller would provide adequate thrust while staying within the cockpit clearance constraint. In order to get the most out of an engine, it must pair well with the selected propeller. Therefore, after research into PT6A propeller pairings, it was decided that the Hartzell HC-B3TN three-bladed propeller would be used to convert engine horsepower into thrust-horsepower. The specifications for this set of propellers is presented in Table 10.

Table 10: Propeller Specifications

Parameter	Value
Make	Hartzell Propeller
Model	HC-B3TN
Blade Model	T9073D-0
Blade Diameter, in. [19]	90
Blade Material [19]	Aluminium Alloy
Weight, lb. [19]	110

6 Aerodynamics

6.1 Airfoil Selection

6.1.1 Airfoil Trade Study

To begin the airfoil selection, a number of similar aircraft that fit this class of aircraft were compiled along with their respective airfoils, shown below in Table 11. The North American Aviation AT-6 Texan was chosen as a similar aircraft as well as the Air Tractor AT-802L Longsword. The A-10 thunderbolt II was also chosen for comparison though it represents an airframe with a payload capacity beyond the scope of the RFP. To explore the option of using different similar aifoils along the span, the NACA 4412 was chosen to compare to the similar airfoil used on the AT-802L, the NACA 4415.

Table 11: Similar Aircraft and Respective Airfoils [2]

Aircraft	Root Airfoil	Tip Airfoil
A-10 Thunderbolt II	6716	6713
AT-6 Texan	2215	4415
AT-802L	4415	4415

As a preliminary comparison, the airfoils were simulated using XFLR5 over a range of angles of attack $-5^\circ < \alpha < 17^\circ$ at a Reynolds number of 10×10^6. The airfoil coefficients of lift, moment, and the lift to drag ratio of were then compared using Figure 18.

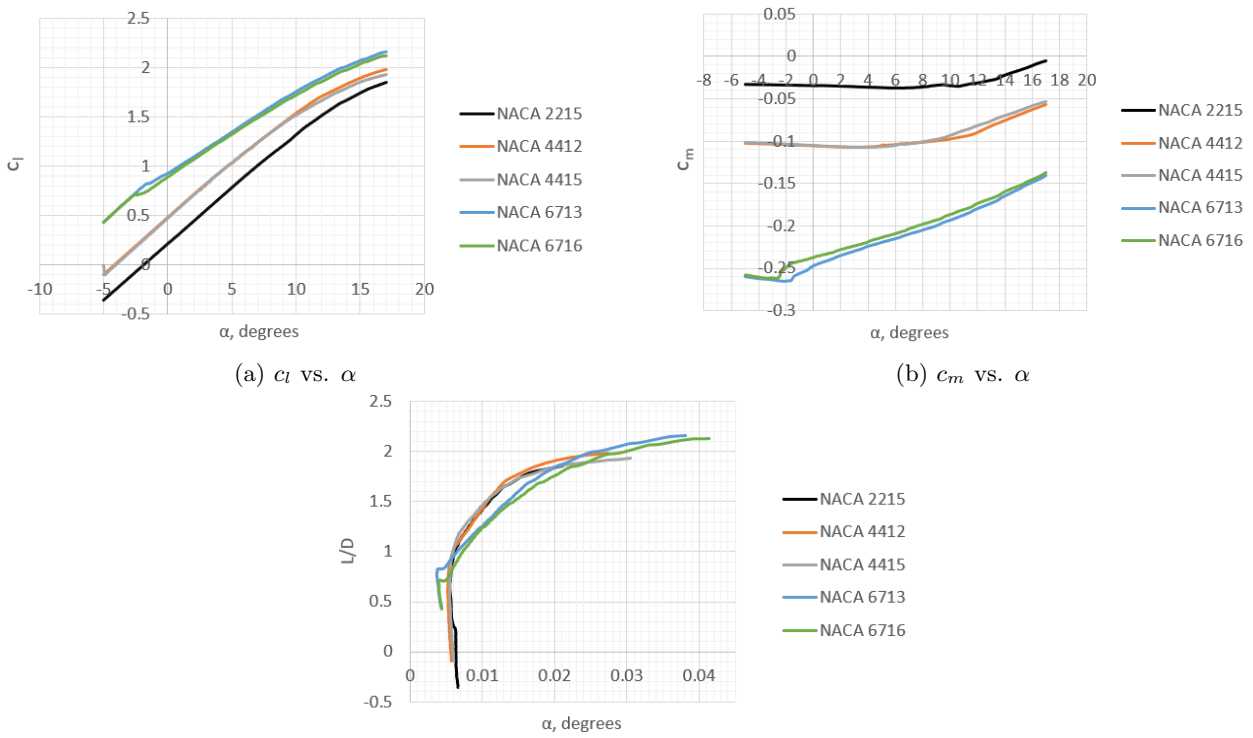

(a) c_l vs. α

(b) c_m vs. α

(c) L/D vs. α

Figure 18: Airfoil Trade Study Data from XFLR5

Analyzing the L/D data shown in Figure 18c, we see that all of the chosen airfoils perform similarly enough that it is difficult for one to justify choosing a particular airfoil over another. To proceed, the other coefficients were analyzed. To minimize the trim drag, the highly cambered NACA 6713 and 6716, having greater magnitudes of moment coefficient (Figure 18b), were removed from consideration first. While the NACA 2215 provides the smallest magnitude of moment coefficient, it is clear from Figure 18a that the airfoil does not provide as much lift as the others. For this reason, the NACA 4412 and 4415 were chosen for further analysis.

Additionally, airfoil selection and comparison methods given by the Warsaw University of Technology [20] were used to validate this selection. Included in this method is a general selection flow chart, Figure 19, that was used to ensure that the chosen airfoils allow the aircraft meet the takeoff, landing, and overall design requirements for the aircraft.

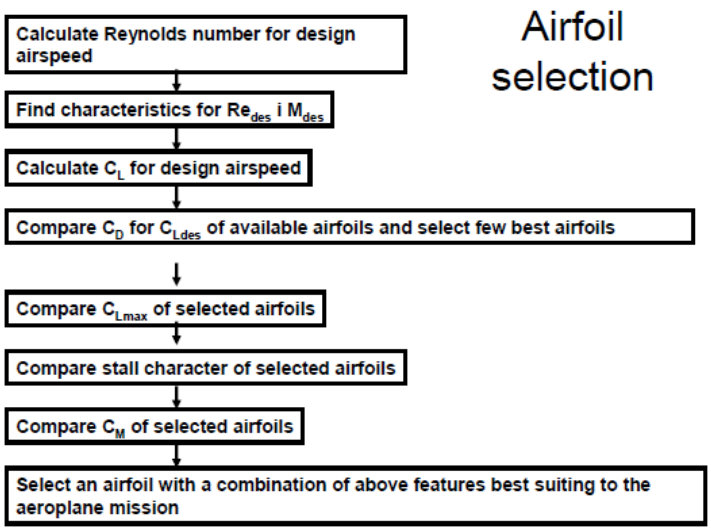

Figure 19: Airfoil Selection Criteria.

6.1.2 Selection Validation

To verify the airfoil data collected from XFLR5, this data was compared to wind tunnel data for these airfoils. Plots for the wind tunnel data were retrieved from Abbott and Von Doehnhoff [1], and are shown below in Figure 20. *NOTE:* The c_m calculated from XFLR5 is calculated about the aerodynamic center, $c_{m_{a.c.}}$. The wind tunnel data for this quantity are shown in Figure 20 (b) and (d) for the NACA 4412 and 4415, respectively.

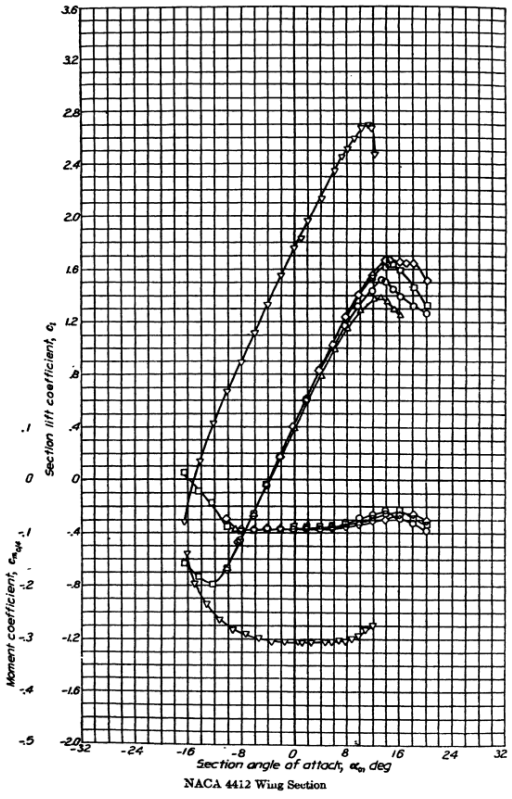

(a) NACA 4412 c_l and c_m vs. α

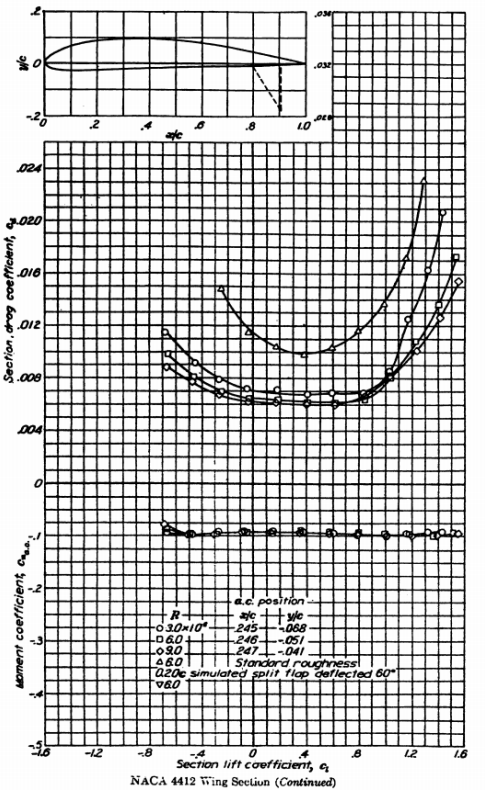

(b) NACA 4412 c_l and c_m vs. α

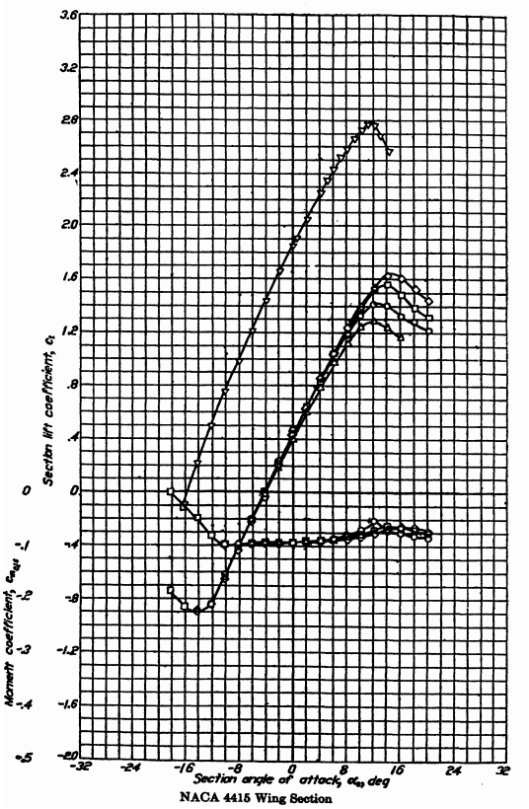

(c) NACA 4415 c_l and c_m vs. α

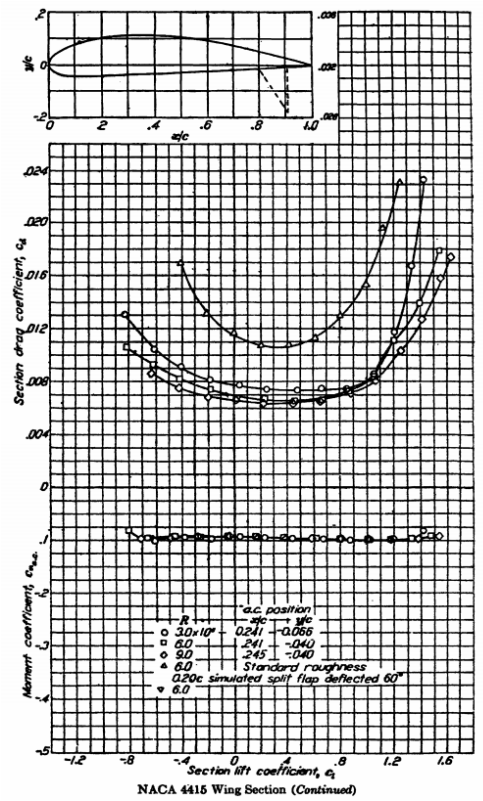

(d) NACA 4412 c_l and c_m vs. α

Figure 20: NACA 4412 and 4415 Wind Tunnel Data [1].

With the understanding that XFLR5 and XFOIL are unable to accurately predict stall characteristics, as seen by comparing Figure 18a and Figures 23d and 23c, the stall angle of attack is assumed to occur at the angles given from the data in Abbott. The stall of the NACA 4412 and NACA 4415 is assumed to occur at $\alpha = 14°$. This stall angle of attack will be useful in further performance analyses to characterize the maximum values of the wing performance coefficients.

6.2 Wing Design

From the airfoil selection trade study, it was determined that the wing would employ the NACA 4415 at the root and the NACA 4412 at the tip. This choice was made to obtain a more elliptical lift distribution, and thus a more efficient wing.

To simplify the construction of the wing, a straight leading-edge design was chosen. This design is acceptable due to the low-speed regime in which the aircraft will operate where wave drag and shock waves will not occur. To increase the efficiency of the wing further by more closely matching an elliptical lift distribution, the wing is designed with a taper ratio of $\lambda = 0.667$. Additionally, with a fixed wing area, this allows a larger wingspan and thus a higher aspect ratio. With a higher aspect ratio, the induced drag of the wing is decreased. To prevent premature wingtip stall with the tapered wing design, the wingtip has a geometric twist of $-2°$. This tip washout will help retain roll authority in stall or near-stall conditions.

6.3 High Lift Devices

6.3.1 High Lift Device Overview

To help meet the required landing distance prescribed in the RFP, slotted flaps were chosen for this application. Slotted flaps will provide a large increase in lift necessary to meet this requirement while minimizing the added complexity from a high lift system. Simpler flap designs were considered such as a plain flap or a split flap, but, in general, flow separation occurs at much lower angles of attack due to the simpler, non-slotted design. Additionally, leading edge high lift devices such as slats were considered, though not implemented in the design. Taking into consideration the added complexity and maintenance requirements relative to the performance increase, leading edge devices were determined to be impractical for this application.

6.3.2 Sizing and Geometry

The sizing for the slotted flaps was estimated by conducting a similarity analysis with different light attack aircraft aircraft. Furthermore, slotted flaps increase the coefficient of lift at takeoff and landing by

providing a ΔC_L of 1.1-1.7 [21]. From preliminary performance calculations this range was sufficient for the listed landing and takeoff requirements.

Table 12: Flap Dimensions

Parameter	Value
Total Span	22.50 ft
Span Ratio	0.50
Total Surface Area	28.35 ft^2
Root/Tip Chord	1.26 ft
Chord Ratio	0.20
Deflection Angle	$0° > \delta_{flap} > 30°$

To arrive at the flap configuration described by the parameters above in Table 12, a method presented in the Aeronautical Sciences Journal was used [21]. For this method, the flap to wing span ratio was used to determine the span of the designed flap. The chord length, which was also calculated for the sizing of the ailerons discussed in Section 8, is constant throughout the entire flap. Additional flap dimensions are listed below in Table 12, while an image of the flap configuration is shown below in Figure 21. In conjunction with this method, flap to wing span ratios of other aircraft in this class were compared. These values are given in Table 13. The flap span ratio of the Gunbus aircraft was chosen to be 0.50 which is in the valid range for this class of aircraft given in the Aeronautical Sciences Journal method. This value was chosen to be slightly higher than the average value found in the similarity analysis (Table 13) to further aid in meeting the takeoff requirement from austere fields without any added complexity. Furthermore, performance calculations given in Section 7 show that this flap configuration is capable of exceeding the minimum takeoff and landing distance requirements, in part due to the high engine power of the Gunbus.

To aid in the survivability of the aircraft in combat situations, a flap hinge mechanism was designed and modeled, shown in Figure 22. This hinge mechanism allows actuation of the flaps without exposing parts of the hinge to enemy fire. Additionally, this eliminates protuberance drag from any protruding hinge linkages.

Table 13: Flap Span Ratio Analysis

Aircraft	Flap Span Ratio
Super Tucano	0.41
T-6 Texan II	0.49
Air Tractor AT-802	0.43
OV-10 Bronco	0.39
Aero L-159	0.44
A-10 Thunderbolt II	0.44
Average	0.43
Gunbus	0.5

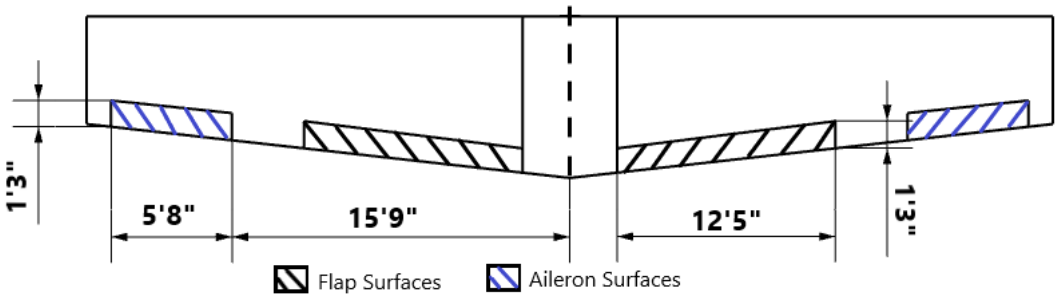

Figure 21: Flap and Aileron Dimensions

(a) Stowed Flap.

(b) Deployed Flap.

Figure 22: Example Flap Mechanism

6.4 Drag Buildup

6.4.1 Calculated Drag Estimates

Table 14: Drag Breakdown

Drag Component	**Drag Contribution**
$C_{D_{O,Friction}}$	0.02164
$C_{D_{O,Ordnance}}$	0.0031
$C_{D_{O,Pylons}}$	0.0024
$C_{D_{O,Gear}}$	0.0104
$\Delta C_{D_{Flap\,15,takeoff}}$	0.0140
$\Delta C_{D_{Flap\,30,landing}}$	0.0435
$C_{D_{i_{TOC}}}$	0.0019
$C_{D_{i_{MTOW}}}$	0.0018
$C_{D_{i_{Landing,max}}}$	0.0015
$C_{D_{Trim.Takeoff}}$	0.0064
$C_{D_{Trim,Cruise}}$	0.0064
$C_{D_{Trim,Landing}}$	0.0053
Totals	
$C_{D_{Takeoff,MTOW}}$	0.0598
$C_{D_{TOC}}$	0.0355
$C_{D_{Landing,max}}$	0.0878

The drag values tabulated below in Table 14 were determined using drag estimation methods from Raymer [22] and Roskam [23] as described in the subsections below. To obtain the worst-case drag scenarios, the ordnance drag was added into all the drag totals to represent a possible mission in which the aircraft returns to base without dropping ordnance. Similarly, for the takeoff induced drag estimation, the MTOW is used, and the weight at TOC is used to represent the highest induced drag due to lift during cruise. Further explanation of the drag estimation methods is given in the following sections.

6.4.2 Wing and Plane Drag Estimation

Using the cruise condition of 330 KTAS at 10,000 ft, the 3D wing was simulated in XFLR5 using a 3D panel method. From this simulation, the induced drag of the wing at each angle of attack was estimated for each segment of flight. Using the calculated weight at top of climb, $W_{TOC} = 13,676\ lb$, the induced drag was calculated to obtain maximum induced drag that would be experienced during the cruise region.

Similarly, the worst-case drag contributions due to lift during both takeoff and landing were calculated using the highest calculated weights for these segments where $W_{MTOW} = 14,447\ lb$ is given in Section 10 and $W_{landing} = 11,392\ lb$ as described in the preceding subsection.

To estimate the drag component due to trim, the induced drag on the horizontal tail was estimated in XFLR5 using the tail incidence angles required for trim determined later in Section 8.4.

Initially, the zero lift drag due to skin friction was estimated using methods Chapter 12 of Raymer [22] along with $\frac{S_{wet}}{S_{ref}} = 5.128$ measured from the CAD model. As a more robust estimation method, the form factor method for component drag buildup given in the same chapter from Raymer [22] was used.

Using the flap sizing estimates from Section 21 above, methods from Section 4.6 of Roskam [23] were employed to estimate the drag contributions due to the extension of the flaps. These drag coefficient increments were determined using the chosen flap deflection of 15 degrees for takeoff and 30 degrees for landing.

6.4.3 Ordnance and Protuberance Drag

Drag due to ordnance and ordnance mounting pylons was estimated once again using methods in Raymer Chapter 12 [22]. With the D/q drag coefficients from Raymer and the six-pylon configuration of the aircraft, the drag due to the ordnance mounting pylons was estimated. The drag component due to the extended landing gear was estimated similarly using the drag coefficient per frontal area of the landing gear in Raymer.

Additionally, using a chosen ordnance loadout discussed later in Section 12, the drag component due to ordnance was estimated. This ordnance loadout includes two Delilah missiles, two Maverick missiles, and two MK-82 bombs. The drag components due to ordnance and protuberance is tabulated above in Table 14.

6.5 Aircraft Aerodynamic Performance

6.5.1 Lift, Drag, and Moment Coefficients

Using the aircraft simulation from XFRL5 along with the drag increment due to the different flap deflection angles calculated from Section 4.6 of Roskam [23], the coefficient of drag polar was estimated below in Figure 23. Similarly, using Section 8.2 of Roskam, the moment coefficient increment due to flap deflection was estimated. Additionally, the lift curve due to flap deflection was estimated using methods from both Section 8.1 of Roskam and Chapter 12 of Raymer [22]. The maximum lift coefficient increment used was determined by averaging the estimate from both of these sources to provide a balanced estimate. The aircraft polars are given below in Figure 23.

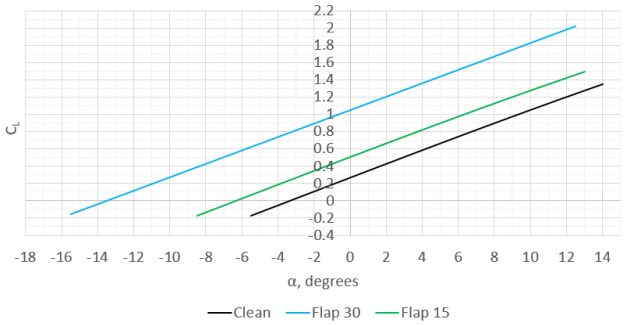

(a) Aircraft C_L vs. α

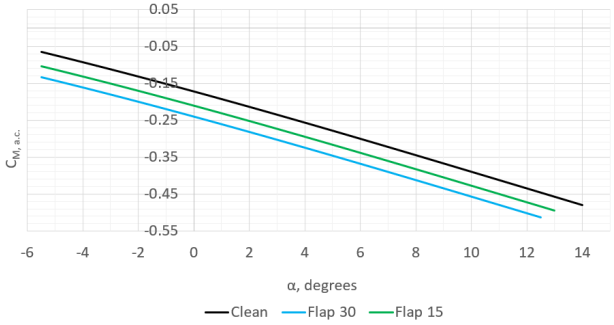

(b) Aircraft C_M vs. α

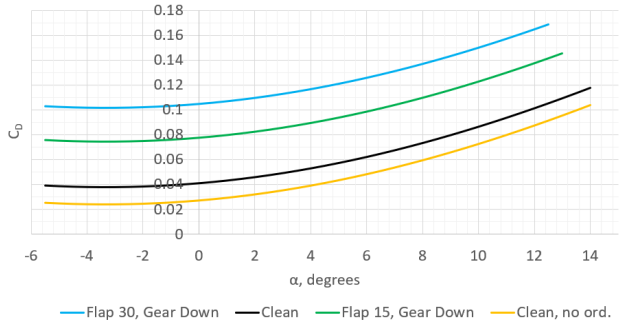

(c) Aircraft C_D vs. α

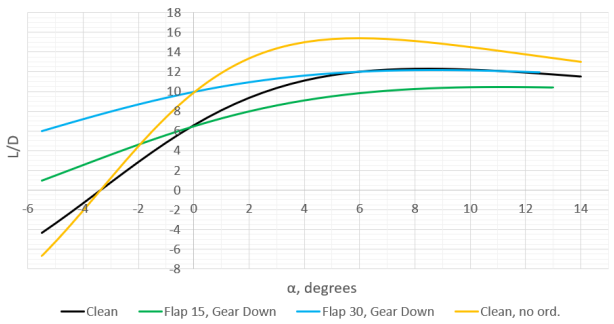

(d) Aircraft L/D vs. α

Figure 23: Aircraft Performance Polars

With the aircraft coefficients calculated over a range of angles of attack during each segment of flight, key parameters for each segment can be collected. These parameters are tabulated below in Table 15. For each segment, these parameters were evaluated for the steady level flight case at the start weight of the segment.

Table 15: Key Segment Information

Parameter	**Takeoff (MTOW)**	**Cruise**	**Cruise, No Ord.**	**Landing (With Ordnance)**
$\alpha, degrees$	8	-0.5	-2	-2
$C_{D_{Tot.}}$	0.105	0.040	0.025	0.102
C_L	1.156	0.202	0.158	0.911

6.5.2 Estimation Methods and Limitations

The current model for determining aircraft polars described in the preceding section is limited in that it does not account for lift and moment effects from the fuselage and nacelles. It does however include a drag coefficient component due to the fuselage and nacelles. Because the wing and stabilizer dominate the lift and moment polars, the lift and moment effects of the fuselage were determined to be out of the scope of this stage of aerodynamic design.

7 Performance

7.1 Required Performance

Table 16: Performance Requirements

Requirement	Design Mission	Ferry Mission
Takeoff/Landing Length	Less than 4,000 ft	
Takeoff/Landing Obstacle	50 ft obstacle	
Cruise Distance	$\geq$ 200 nm	$\geq$ 900 nm
Cruise Altitude	$\geq 10,000$ ft	$\geq 18,000$ ft
Loiter Time	4 hrs	N/A
Reserves	Sufficient for 3,000 ft climb	
Reserves	Sufficient for 45 min loiter	

The performance requirements and targets are listed in Table 16. These are the general attributes for both missions that need to be accounted for in the performance of the aircraft. For a time visual for the design and ferry missions refer to Figure 3 and 4 in Section 2. The design mission is more stringent than the ferry mission due to a heavier payload and more extensive mission profile. Thus, if the aircraft is able to carry out the design mission, it is more than likely able to complete the ferry mission.

7.2 Expected Performance

For the design mission, the aircraft cruises at 330 kt for the required 100 nmi within 20 minutes. The most efficient flight speed and longest loiter duration is determined from flight coefficients found in Figure 24.

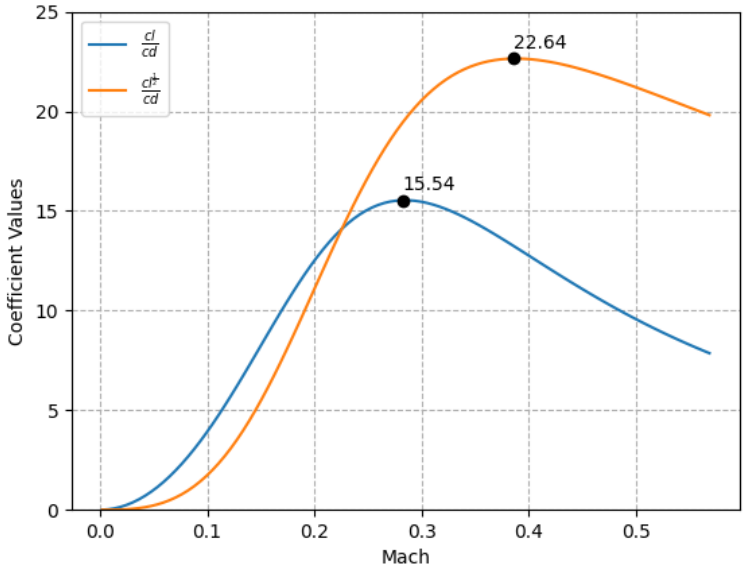

Figure 24: Flight Coefficients

The max range is given at 0.28 Mach or 186 KTAS, and the max loiter is given at 0.38 Mach or 253 KTAS. The other cruise segments that do not have a time constraint have a speed of 280 KTAS. This is chosen as a trade study was done with the AT6 Wolverine and A29 Super Tucano. The two comparable planes have lower cruise speeds at altitude, and for the Gunbus aircraft being produced by 2025, speed is more of an important factor compared to efficiency. The flight envelope is shown in Figure 25.

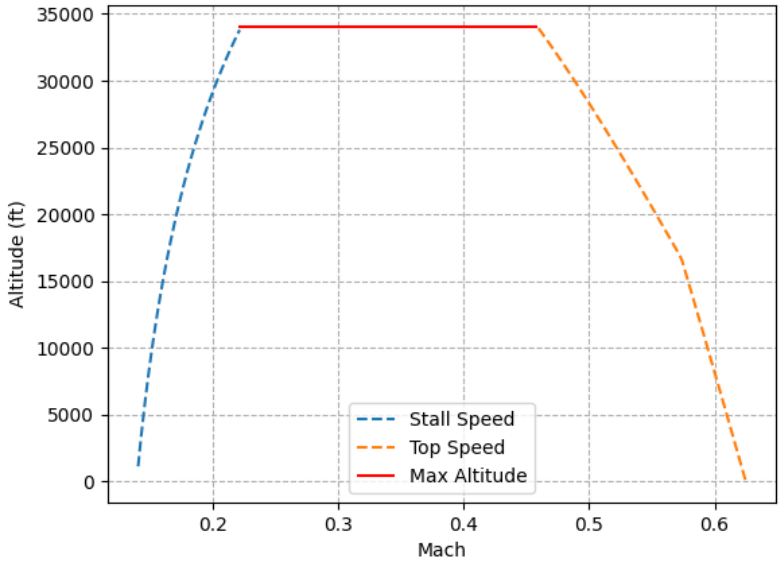

Figure 25: Flight Envelope

Using the excess power model, the max velocity, min velocity, rate of climb, and service ceiling were determined. The range of the max payload (design mission) was determined using a time step method to calculate each segment of the mission. The cruise altitude was determined from the highest specific fuel consumption. Table 17 lists the performance attributes of the aircraft from these calculations.

Table 17: Performance Parameters

Parameter	Value
Max Velocity (SL)	413 kt
Min Velocity (SL)	93 kt
Max Rate of Climb (SL)	3,268 ft/min
Service Ceiling	34,000 ft
Range	1,041 nmi
Cruise Altitude	15,000 ft

7.3 Takeoff & Landing Performance

The calculations for takeoff and landing distance are calculated at max takeoff weight and after second descent of the design mission, respectively. Since the aircraft must be able to takeoff from an austere field, a rolling resistance coefficient of 0.04 is used. The distances for both the design and ferry missions are tabulated in Tables 18 and 19. This includes the 50 ft obstacle during both takeoff and landing.

Table 18: Takeoff Performance

Mission	Rolling Resistance*	Takeoff Distance, ft	Ground Roll, ft	Takeoff Velocity, ft/s
Design	0.04	2,525	672	182
Ferry	0.04	2,275	532	174

Table 19: Landing Performance

Mission	Resistance Coefficient (Braking/Reverse)*	Landing, ft	Ground Roll, ft
Design	0.45	2,777	739
Ferry	0.45	2,499	585

7.4 Range Performance

The time step for both the design and ferry missions were used to calculate the final range of the aircraft. Figure 26 shows the range as a function of payload weight. The dotted lines indicate the range for a particular segment. However, the payload weight can be taken at any point to find a given range. The data is tabulated in Table 20. One notable finding is from the ferry mission payload weight to zero weight, there is little effect on the range compared to max payload to ferry mission. There is diminishing return for not carrying a payload, most likely due to constant weight in the forms of engine, structures, and fuel. This is subject to change if less fuel is carried while also reducing the payload.

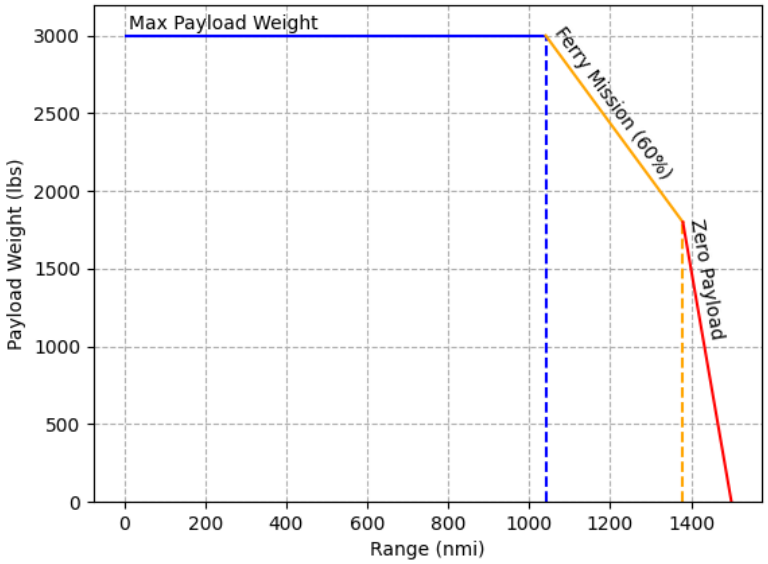

Figure 26: Payload Range

Table 20: Payload Range Data

Max Payload Range (nmi)	Max Gerry Range (nmi)	Zero Payload Range (nmi)
1,041	1,379	1,499
+0%	+32%	+43%

Range-speed is similar to the flight coefficients. This snapshot was taken at cruise altitude with no payload which gives the desired range of 1,499 nmi when the cruise speed is at 0.33 Mach.

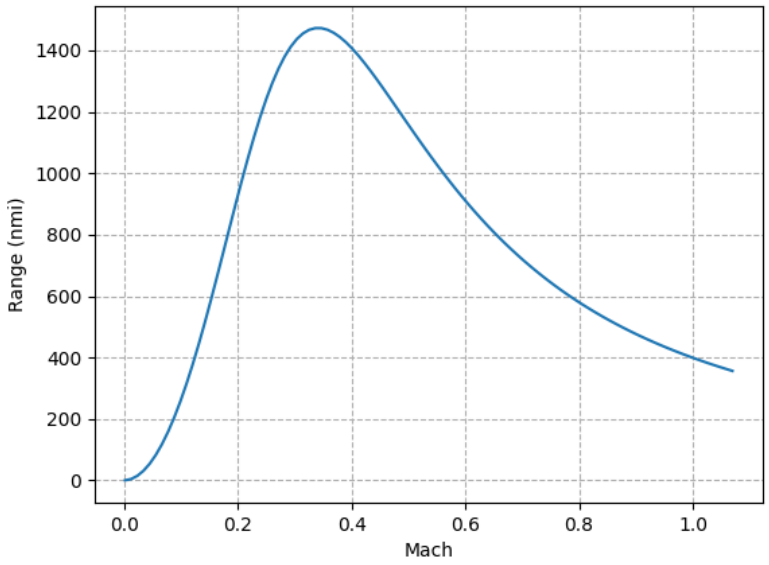

Figure 27: Speed Range

The SR is the distance traveled divided by the specific fuel consumption. This relation to altitude was used to calculate the optimal cruising altitude which is located at the highest SR value. The optimal cruising height using this relation is 15,000 ft with an efficiency of 0.77 kts/lb/hr given the max payload and max fuel capacity. Although the change in weight may effect the values, it will not effect the optimal cruising altitude or shape of the curve. The relation is plotted in Figure 28.

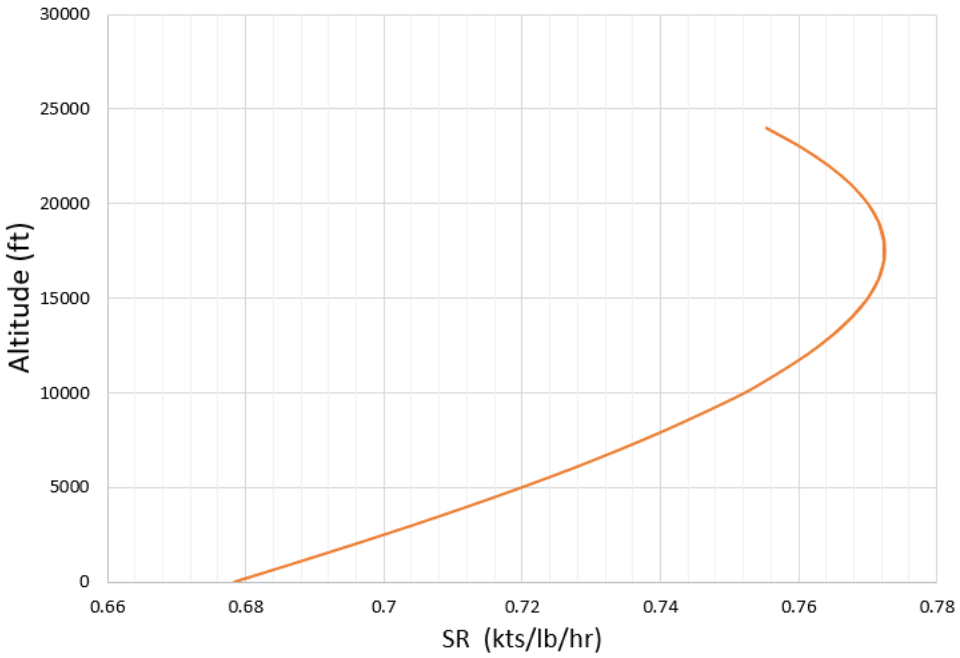

Figure 28: SFC vs Altitude

7.5 Fuel Burn & Drag

The total fuel burn and average drag per segment are compared in Tables 21 and 22. Since the design mission is more constrained requirements of the two, it is shown that the maximum drag experienced is at the first cruise in the design mission. This is due to the increase speed demanded by the time constraint given by the requirements. Since the maximum payload is carried in the design mission compared to the 60% of the ferry mission, the design mission burns a total of 2,005 lb of fuel, approximately 200 lb more than the ferry mission.

7.5.1 Ferry Mission

Table 21: Ferry Mission Fuel Burn and Drag

Mission Segment	Total Fuel Burn per Segment, lb	Average Drag per Segment, lb
Warmup, Taxi, Takeoff	70	287
Climb	132	741
Cruise	1,366	837
Descent	10	784
Landing & Taxi	34	264
Reserves	201	652
Totals	1,813	3,566

7.5.2 Design Mission

Table 22: Design Mission Fuel Burn and Drag

Mission Segment	Total Fuel Burn per Segment, lb	Average Drag per Segment, lb
Warmup, Taxi, Takeoff	95	355
Climb 1	75	565
Cruise 1	255	1.402
Descent 1	5	1,014
Loiter	850	929
Climb 2	62	870
Cruise 2	249	1,375
Descent 2	4	1,087
Landing & Taxi	55	320
Reserves	355	1,087
Totals	2,005	9,004

7.6 Climb Analysis

The aircraft is expected to climb at 15,000 ft given the initial MTOW at 100% engine power. The climb results are tabulated in Table 23. The main performance parameters during this segment are the angle of climb and rate of climb. Since both the engines are operating at full capacity there is approximately two to four times the power available compared to the power required to overcome drag at every time step of climb.

Equations 1 and 2, found in Raymer, were used in the calculation presented in the table below.

$$\gamma = sin^{-1}\left[\frac{550\text{BHP}\eta_p}{VW} - \frac{D}{W}\right] \tag{1}$$

$$V_v = \frac{550\text{BHP}\eta_p}{W} - \frac{DV}{W} \tag{2}$$

Table 23: Design Mission Climb Data

Parameter	Value	Units
Rate of Climb	29.36*	ft/s
Angle of Climb	7.26*	degrees
Lift-to-Drag	15.57*	
Total Time to Climb	8.21	min

*Average values taken across the entire segment

7.6.1 Descent

The aircraft is operated at 5% throttle to achieve the following descent values.

Table 24: Design Mission Descent Data

Parameter	Value	Units
Rate of Climb	-18.47*	ft/s
Angle of Climb	-3.93*	degrees
Lift-to-Drag	16.82*	
Total Time to Descent	10.11	min

*Average values taken across the entire segment

7.7 Trade Studies

Two notable aircraft with similar missions have the performance values shown in Table 25. The Gunbus aircraft has increased ranged and higher max speed among its competitors. Although the recommended cruise speed is on par with similar aircraft, if a mission requires a higher speed, the aircraft will be able to handle it. One notable trade off is the simplicity of a one engine design as seen in the A-29 and AT-6. However, team Gunbus is willing to accept increased maintenance cost for the benefit of engine redundancy and increased performance.

Table 25: Performance Trade Study

Aircraft	Range, nmi	Combat Range, nmi	Ferry Range, nmi	Service Ceiling, ft	Cruise Speed, kts	Max Speed, kts	Stall Speed, kts
Gunbus	1,041	400 nm	1,379	34,000	280	413	85
A-29	720	300	1,542	35,000	280	320	80
AT-6	900	N/A	N/A	31,000	280	316	80

8 Stability and Control

The design of this aircraft features a conventional tail configuration. This configuration was chosen over a V-tail and a T-tail because it not only offers a simplistic design and flight control system integration, but it also does not have the deep stall tendencies and added structural weight that are present in T-tail configurations [24]. For this aircraft, a symmetrical airfoil was selected because of its shape allows the pilot to effectively use the rudder and elevator in both operating directions [25]. The possible airfoils that were considered were the NACA 0009, NACA 0010, and the NACA 0012. The different airfoils were compared by looking at the drag polar curves corresponding at a constant Reynolds Number. From the data, it was calculated that the NACA 0009 airfoil, even though it is thinner than the other airfoils, had the smallest lift to drag coefficient since it had the largest amount of drag [26]. The NACA 0012 and 0010 both had similar coefficient of lift to drag values. For a fixed coefficient of drag value of 0.06, the corresponding coefficient of lift for the NACA 0012 airfoil was 1.4 [27], while the corresponding coefficient of lift for the NACA 0010 airfoil was 1.38 [28]. In the end, the airfoil that was chosen for both for the vertical and horizontal stabilizers was the NACA 0010. This airfoil was chosen because it had a similar drag polar as the NACA 0012, but is an overall thinner airfoil which would reduce the weight of the vertical and horizontal stabilizers and the overall cost of the aircraft.

8.1 Horizontal Stabilizer and Elevator Sizing

To size the horizontal stabilizer, the method presented in Roskam [29] was used. For this method, the historical values of volume coefficients for a variety of military trainer and commercial twin turboprop aircraft were averaged in order to calculate the coefficient for Gunbus, which is a combination of both classes. The moment arm of the horizontal stabilizer was determined by using the measurement tool in NX. This value represented the distance from the aircraft's C.G. to the approximate location of the AC of the horizontal stabilizer. Using the defined volume coefficient and the equation from Roskam [29] the initial horizontal stabilizer surface area was calculated. In order to verify this method, a notch diagram was created and is

shown below in Figure 29.

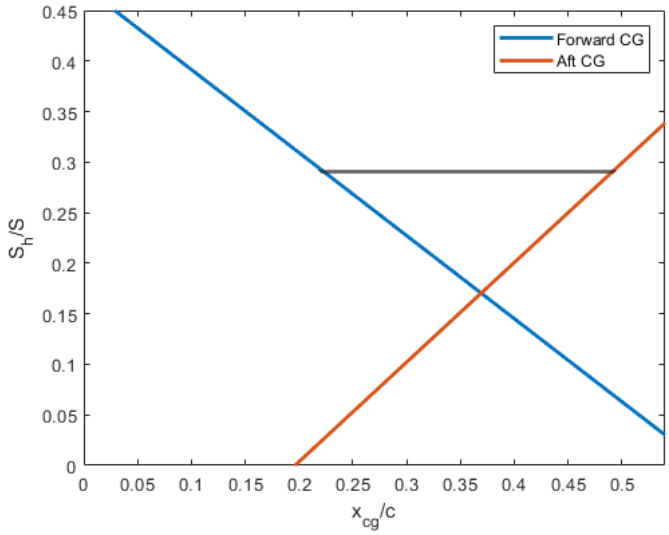

Figure 29: Notch Diagram

From the notch diagram, it was determined that a minimum surface area of 79.8 ft^2 is needed, which is smaller than the surface area that was calculated from Roskam. The increase in area was a result of placing the LE of the elevator at 33% MAC. This diagram verified the method, described above, that was used to size the horizontal stabilizer. Lastly, the span and the root/tip chords were determined with the range of values presented in Roskam. The dimensions of the horizontal stabilizer are listed below in Table 26 and a visual representation is depicted in Figure 30.

The elevator was sized using historical data for the the elevator to stabilizer area ratio which was presented in Roskam [29]. Once the elevator to stabilizer area ratio was chosen, the chord of the elevator was determined to be 33% of the horizontal stabilizer's chord. This allowed the team to efficiently place a spar at the leading edge of the elevator. The resulting elevator parameters are listed below in Table 26. A visual representation of the horizontal stabilizer configuration is shown below in Figure 30.

Table 26: Horizontal Stabilizer Dimensions

Parameter	Value
Span	18.50 ft
Root Chord	6.1 ft
Tip Chord	2.62 ft
Quarter Chord Sweep	13.5^o
Surface Area	83.05 ft^2
Leading Edge Location	31.62 ft
Volume Coefficient	0.79

Table 27: Elevator Dimensions

Parameter	Value
Span	18.50 ft
Span Ratio	1.00
Surface Area	25.44 ft^2
Root Chord	2.0 ft
Tip Chord	0.75 ft
Chord Ratio	0.33
Deflection Angle	$\pm 25^o$

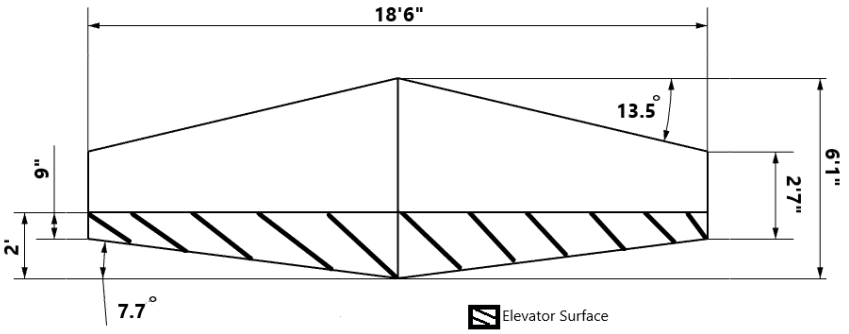

Figure 30: Horizontal Stabilizer and Elevator Sizing

8.2 Vertical Stabilizer and Rudder Sizing

Similar to the horizontal stabilizer sizing, the vertical stabilizer was sized using historical data for military trainers and twin turboprop aircraft presented in Roskam [29]. The chosen values for the vertical stabilizer, shown below in Table 28.

The rudder's dimensions were determined by using historical data found in Roskam [29]. With this data, the area and chord ratios of the rudder were calculated. The Super Tucano's rudder configuration was used to construct the rudder configuration used for the Gunbus aircraft. This configuration was chosen because it provides sufficient rudder surface area without having to increase the height of the vertical stabilizer. This reduction in height reduces the needed structural reinforcements which reduces the weight of the aircraft. If a traditional rudder and vertical stabilizer layout was chosen (vertical stabilizer on-top of fuselage), the overall height of the tail would increase by 2.67 ft, which a 45.71% increase. This increase in surface area could have negative effects since it increases the target area for enemy fire, which could lead to a decrease in survivability of the aircraft. In Table 29, the resulting rudder dimensions are listed. A visual representation

of the rudder is shown below in Figure 31 a visual.

Table 28: Vertical Stabilizer Dimensions

Parameter	Value
Span	8.6 ft
Root Chord	2.75 ft
Tip Chord	1.75 ft
Quarter Chord Sweep	10^o
Surface Area	35.61 ft^2
Leading Edge Location	34.83 ft
Volume Coefficient	0.05

Table 29: Rudder Dimensions

Parameter	Value
Span	8.6 ft
Span Ratio	1.00
Surface Area	21.37 ft^2
Root Chord	3.00 ft
Tip Chord	1.80 ft
Chord Ratio	0.60
Deflection Angle	$\pm 30^o$

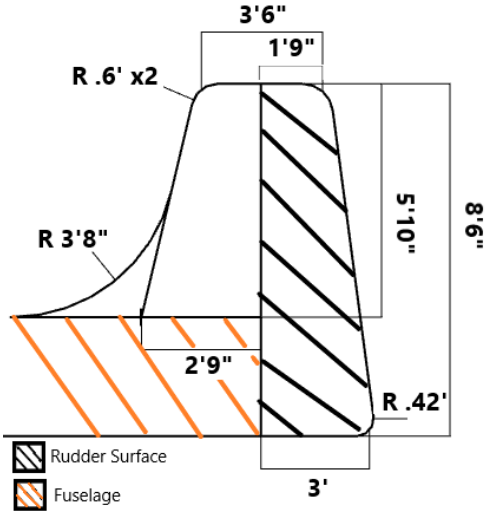

Figure 31: Vertical Stabilizer and Rudder Sizing

8.3 Aileron and Flap Surface Sizing

In order to size the ailerons, the method listed in Sadraey was used. [30]. For this method, historical ratios along with wing dimensions were used to determine the aileron area, span, and chord. The resulting aileron dimensions are listed below in Table 30 and a visual representation of the aileron can be seen in Figure 21. The steps taken to size the flaps are outline in Section 6.

Table 30: Aileron Dimensions

Parameter	Value
Span	13.50 ft
Span Ratio	0.30
Total Surface Area	17.01 ft^2
Root/Tip Chord	1.26 ft
Chord Ratio	0.20
Deflection Angle	$\pm 30^o$

8.4 Trim Diagram

For this aircraft, a variable pitch stabilizer is utilized to prevent the pilot from having to use their surface controls to achieve a desired angle of attack. The incidence of the wing was calculated to be 2.88^o, by using an equation from the University of Hamburg [31]. With this calculated incidence and the equations found in McCormick [17], the desired horizontal stabilizer incidence and elevator deflection angle were determined. To achieve steady level flight at cruise, a horizontal stabilizer incidence of 2.0^o was calculated. In landing and takeoff configurations, a similar approach was used, and the incidence angle for these configurations will be 1^o and 2^o, while the elevator deflection angles will be 2.2^o and 2^o. The coefficient of moment at zero represents the equilibrium trim point where the pitching moment with respect to the C.G. is zero. Additionally, the increase in incidence allows for the pilot to reduce the needed pitch angle leading to a better field of view which is an important feature for a light attack aircraft.

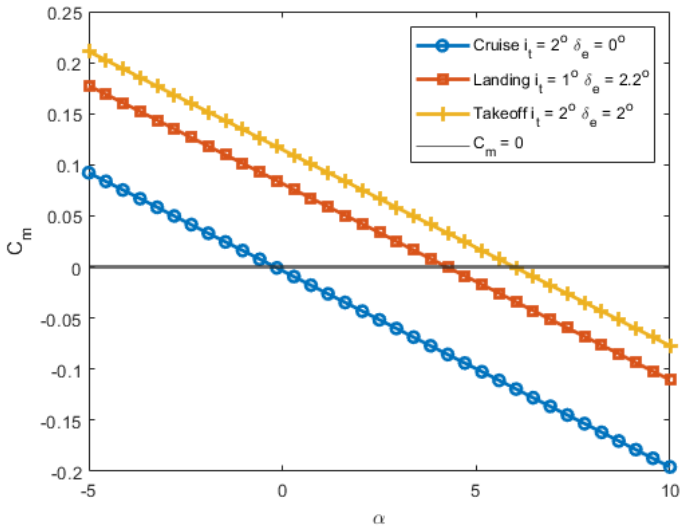

Figure 32: Trim Diagram

8.5 Longitudinal Static Stability

The neutral point was calculated by using wing and horizontal stabilizer dimensions along with equations from MIT [32]. The static margin range was calculated by using the fore and aft C.G. which are described in detail in Section 10. This range represents the pitch stability of the aircraft and a larger static margin indicates a more stable aircraft. Negative and small static margin values indicate that the aircraft may be extremely difficult to fly without the use of computer control systems. Since this aircraft is flown by using computer control systems the static margin of the aircraft can be decreased to improve maneuverability.

Table 31: Longitudinal Static Stability Parameters

Parameter	Value (% MAC)
Static Margin	9.63% - 22.63%
Fore C.G.	17.50%
Aft C.G.	30.50%
Neutral Point	40.13 %

8.6 Stability Control Derivatives

The derivatives listed below in Table 32 were calculated by using equations listed in McCormick [17], while the lift curve slope was calculated by using the equation listed in Raymer [22]. With the known lift curve slope and the position of the neutral point and C.G. points, the pitching moment coefficient curve slope was determined. Since this value is negative, the aircraft is determined statically stable. In order to estimate the pitching moment coefficient of the deflection angle, an assumption for the control surface angle of attack effectiveness parameter was made. Using the chord ratio of the control and lifting surface the value for the parameter was estimated to be 0.5. The aircraft was also determined to have static lateral and directional stability since both the rolling moment coefficient and yaw moment coefficient with respect to the side slip angle were both respectively negative and positive.

Table 32: Stability Control Derivatives

Derivative	Value (rad^{-1})
$C_{L\alpha}$	5.56
$C_{m\alpha}$	-1.1
$C_{m\delta_e}$	-1.65
ϵ_α	0.43
$C_{l\beta}$	-0.07
$C_{n\beta}$	0.18

8.7 Directional and Lateral Stability

The lateral stability of the aircraft was examined by determining the roll rate and roll time through 60^o (-30^o to 30^o) while using 10^o aileron deflection. Using the equations found in McCormick [17] the roll rate for this aircraft was 0.87 rad/s or 49.98 deg/s. This allowed the aircraft to complete the roll in 1.20 seconds which is below the listed requirement of 1.40 seconds for a light utility aircraft. The directional stability was determined by calculating the needed rudder deflection angle for takeoff and landing for a one engine inoperative case. For both landing and takeoff the needed rudder deflection was less than the maximum allowed rudder deflection. This verified that the aircraft is controllable with one engine inoperative, and it also confirmed that the rudder is sufficiently sized.

Table 33: Roll Time Through 60^o

Parameter	Value
Roll Rate	0.87 rad/s
Roll Time	1.20 sec

Table 34: Rudder Deflection for One Engine Inoperative

Mission Segment	Rudder Deflection
Takeoff	26.30^o
Landing	2.40^o

8.8 Longitudinal and Lateral Flight Analysis

Longitudinal flight analysis was conducted by solving the equations of motion associated with the X and Z directions and the sum of the moments about the C.G. These equations of motion were solved by using the stability and control derivatives associated with each equation. The calculated values shown below in Table 35 met the Level 1 requirements listed in McCormick [17] for a medium sized, medium-high maneuverability aircraft.

Table 35: Longitudinal Flight Analysis

	Frequency (rad/s)	Damping Ratio	Requirement Damping Ratio
Phugoid	0.17	0.08	>0.04
Short Period	3.59	0.48	>0.35

In order to further determine the quality of flight of this aircraft, the damping ratio for dutch roll, time constant for roll, and doubling time for spiral modes were calculated. This was done by using the equations of motion, found in McCormick [17], for later-directional motion and by using side force, rolling moment, and yawing moment derivatives. The calculated values, found below in Table 36, satisfied the Level 1 requirements for a medium sized medium-high maneuverability aircraft that were listed in McCormick [17]. The damping ratio for dutch roll did not meet the Level 1 requirements, but it did meet the Level 2 requirements. One way that the damping ratio can be increased is by reducing the dihedral of the wing as this increases Dutch Roll tendencies.

Table 36: Lateral Flight Analysis

Parameter	Value	Requirement
Dutch Roll Natural Frequency	2.10 Hz	>0.4 Hz
Dutch Roll Damping Ratio	0.06	>0.19
Time Constant for Roll	0.41 sec	<1.4 sec
Doubling Time for Spiral Modes	26.2 sec	>20 sec

9 Structures and Loads

9.1 Loads and Dynamics

9.1.1 V-n Diagram

A V-n diagram was made to represent the operating flight strength limitation of the Gunbus aircraft design. The flight envelope is contingent on four design parameters: the aircraft design gross weight, the aircraft configuration, symmetry of loading, and the applicable altitude. The limit airspeed is calculated as a design reference point because exceeding the flight limit could lead to critical gust, destructive flutter, aileron reversal, and wing surface divergence. There are two types of V-n diagrams for military aircraft, the maneuver V-n diagram and the gust V-n diagram. The final strength analysis of the airframe must be based on both the maneuver and gust envelope. Using methods outlined in Roskam [33], the maximum level flight speed (V_H), design maneuver speed (V_A) and the maximum design dive speed (V_L) were calculated at

sea-level in KEAS to provide maneuver V-n diagram airspeed limit. The design maximum load factors are specified in MIL-A 8861(ASG). The design gross weight is estimated using the sum of the aircraft empty weight and 60 percent of the pay load and fuel weight. The stall speed of the aircraft is found when the load factor n is at 1. The gust V-n diagram was constructed to show the envelope of velocities and load factors that the aircraft might encounter through turbulent air in flight. The military gust V-n diagram follows the same guidelines as FAR25. The design speed for maximum gust intensity (V_B) was approximated using numerical methods and it must not exceed the cruise speed (V_C). Figure 33 outlines the combined maneuver and gust flight envelope of Gunbus. It is observed from the combined gust and maneuver V-n diagram that gust loads are defined within the maneuver envelope and would not become a critical concern for the airframe loading. Input values for the V-n maneuver and gust diagram are provided in Table 37.

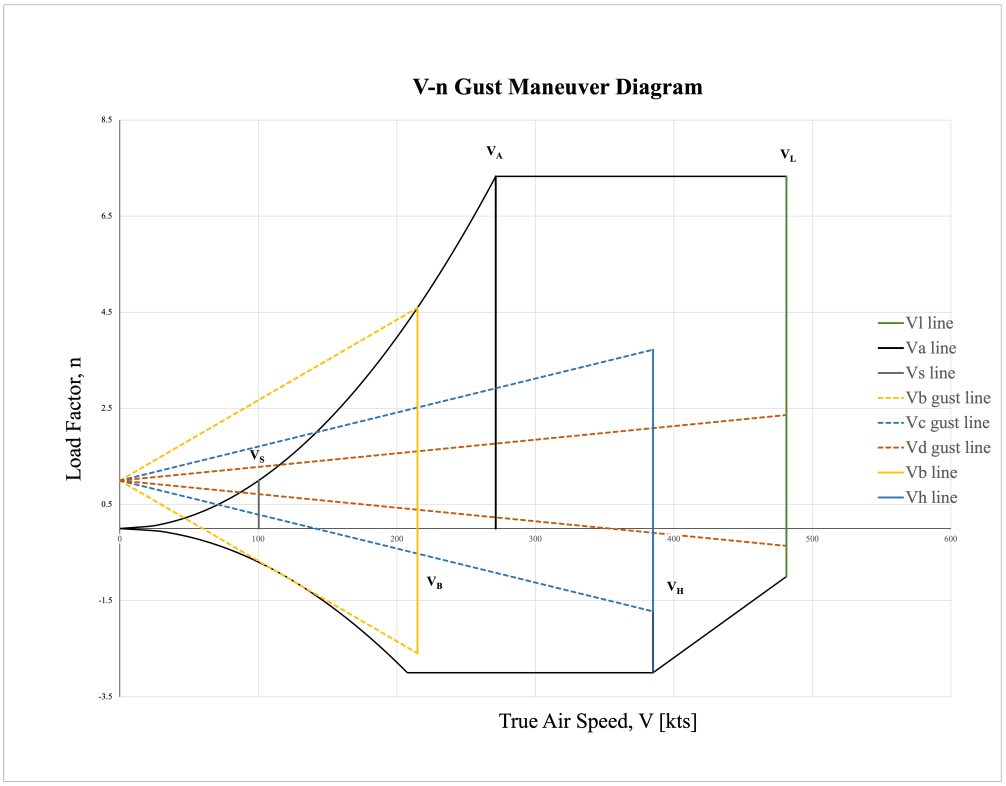

Figure 33: V-n Maneuver and Gust Diagram

Table 37: V-n Maneuver and Gust Diagram Calculations

$V_H(kts)$	$V_l(kts)$	$V_A(kts)$	$V_s(kts)$	$V_B(kts)$	$n_{pos_{max}}$	$n_{neg_{max}}$	Gust Velocity, U_{de}	$C_{L_{max}}$	Alleviation Factor, K_g	Design Gross Weight, lb
385	481	271	215	59.39	7.33	-3	39.1	4.463	0.8332	12,638

9.1.2 Wing Loading

Design wing loads include shear forces, bending moments, and torsions resulting from air pressure and inertial loads. Flight loads are experienced when maneuvering at the limits of the V-n diagram. The spanwise wing loading was approximated using the trapezoid method, the elliptical method, and the Schrenk method. The Schrenk method provides reasonable estimation, especially for non-elliptical wing configuration, by averaging the results from the trapezoid method and the elliptical method to provide an accurate comparison. Spanwise loading from the aforementioned methods are overlaid in Figure 34.

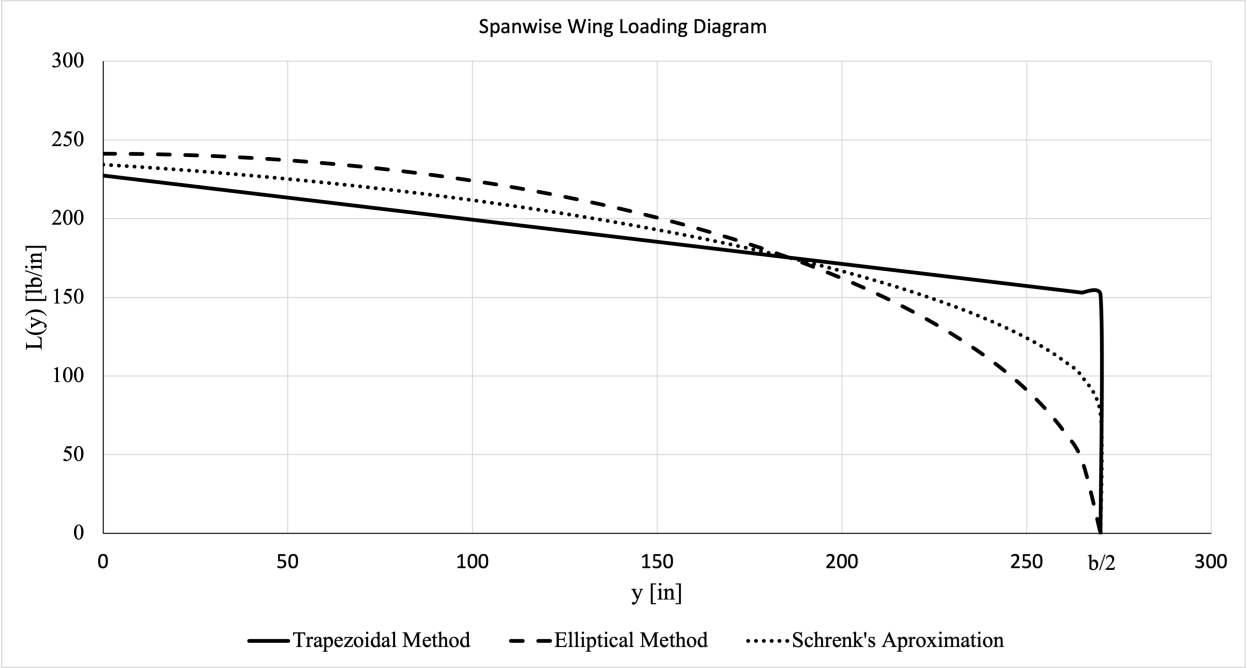

Figure 34: Spanwise Wing Loading

The spanwise wing load is an idealized estimation without considering effects on wing loading from the fuselage, nacelle, and wing stores. The effects of these items are not determined quantitatively. However, in stress analysis, it is necessary to investigate the maximum torsion and compression at the wing cross sections for each item to design the spars accordingly. The overall loading on the wing with effects from structural weight and fuel weight is shown in Figure 35a.

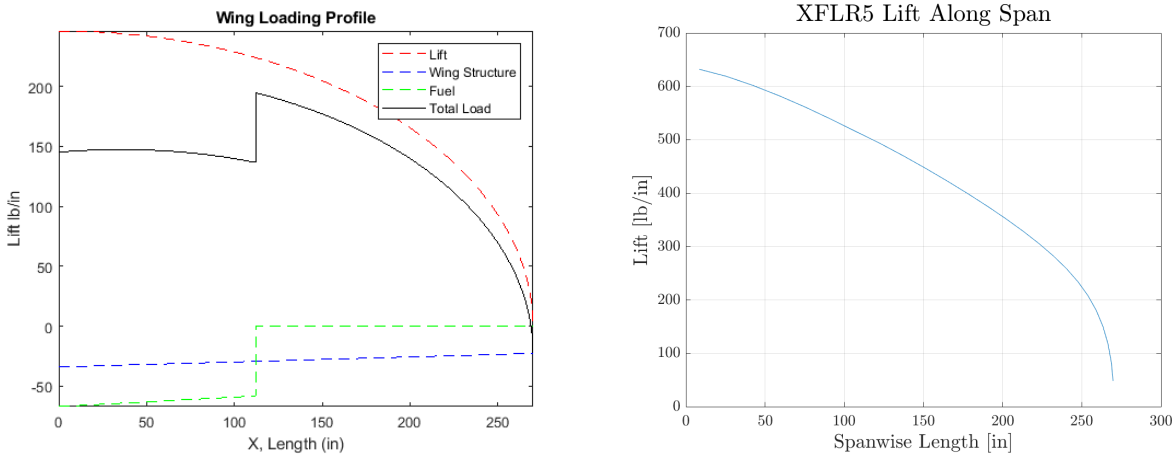

(a) Combined Wing Loading

(b) XFLR5 Spanwise Wing Loading

Figure 35: Wing Loading

Wing loading was also found using analytical methods to provide a comparison to the idealized approximation. Computational fluid dynamics was conducted in XFLR5 software using the vortex lattice method to model the lift distribution on the wing without taking the fuselage into consideration. The resultant spanwise lift distribution is plotted in Figure 35b.

Compared to the spanwise lift distributed calculated using Shrenk's method, the XFLR5 results show a significant higher lift distribution. The cause behind the drastic difference could be attributed to the idealized assumptions made using Shrenk's method.

9.1.3 Bending Moment and Shear Force

The bending moment and shear force from airloads on the wing are numerically approximated as shown in Figure 36. The bending moment and shear force are greatest at the root of the wing and gradually taper off to zero at the tip of the wing. This decrease occurs because the root section produces positive lift while the tip section produces negative lift. The ultimate bending moment and shear force are the largest loads experienced on the wing at the wing span location where the wing box structure is attached to the fuselage, denoted $y(Ult)$. At $y(Ult)$ the ultimate bending moment and shear force were calculated and listed in Table 38. The ultimate shear force and bending moment calculations are crucial in the initial sizing process for the material selections for the wing spars and ribs.

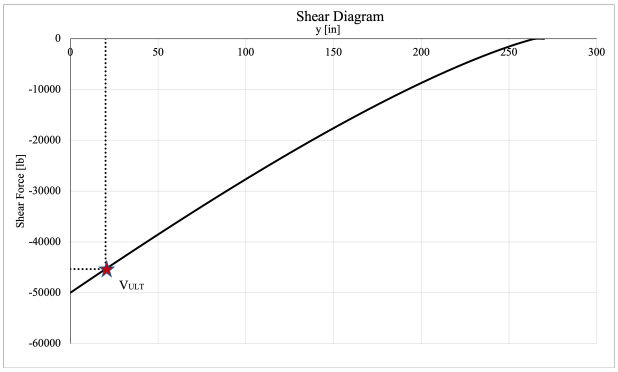

(a) Spanwise Shear Force

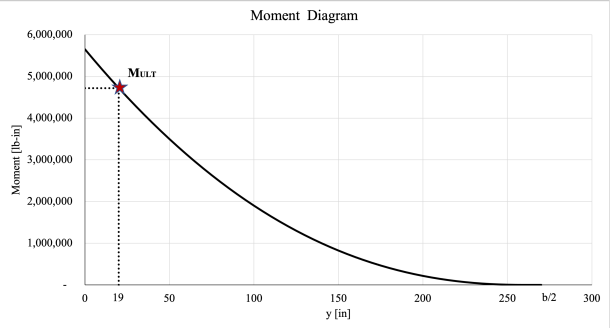

(b) Spanwise Bending Moment

Figure 36: Ultimate Shear and Moment Plots

Table 38: Ultimate Shear Force and Moment

y(Ult), lb	Semi Wing Span, b/2, lb	Ultimate Shear, V_{Ult}, lb	Ultimate Moment, $M_{Ult}, lb - in$
19	270	-45,336	4,720,000

9.1.4 Load Cases and Load Paths

Several load cases are significant factors for structural analysis, namely landing and taxi due to the large concentrated loads applied to the wing from wing-mounted gear and large load factors caused by rough runways. Additional load conditions considered while the aircraft is in flight are cruise load path and max load path. Cruise load condition is assessed when the aircraft is traveling at cruise speed of 330 knots and cruise altitude of 15,000 ft for the design mission. Max load condition is obtained when the load factor is maximum, where $n = 7.33$. The max load factor defines the upper limitation of the flight envelope. Therefore, it is crucial to subject the airframe to structural analysis to ensure the integrity of the structural design at the maximum load case of the flight envelope.

Three load path diagrams with idealized point loads are shown, representing the loads experienced by the aircraft on the ground and in the air. The forces experienced on the ground are the weight of the aircraft, such as fuselage/empennage weight, fuel weight, engine weight, and ordnance weight. The normal force on the landing gear counteracts the weight of the aircraft. Additionally, Gunbus has opted to pressurize the cockpit, which plays an important role in the initial sizing of the fuselage structure. The loads experienced in flight are lift and weight on the wing, torsion on the ribs, pressurization, and weight of the fuselage. The loads on the wing are distributed across the spar and transferred to the fuselage from the wing box.

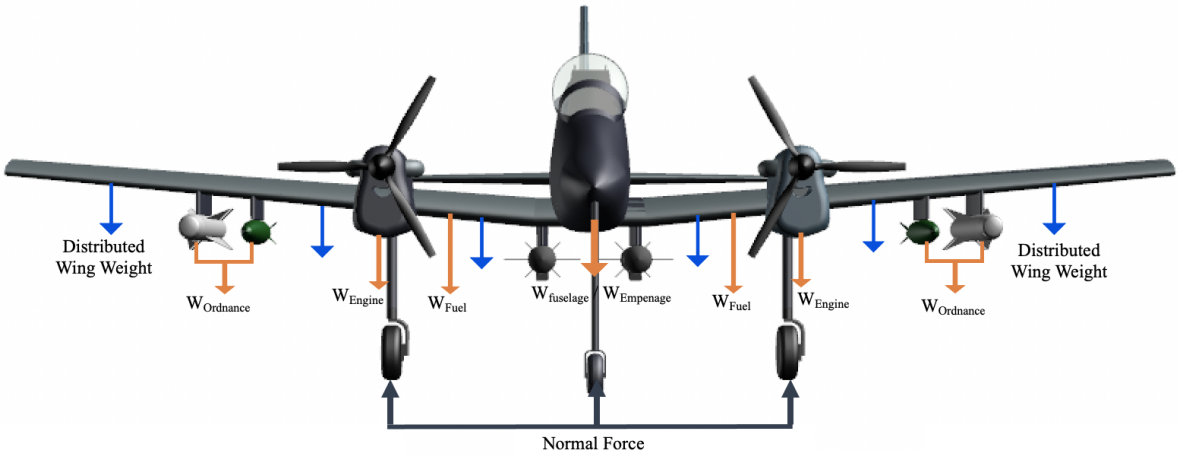

(a) Load Path on the Ground

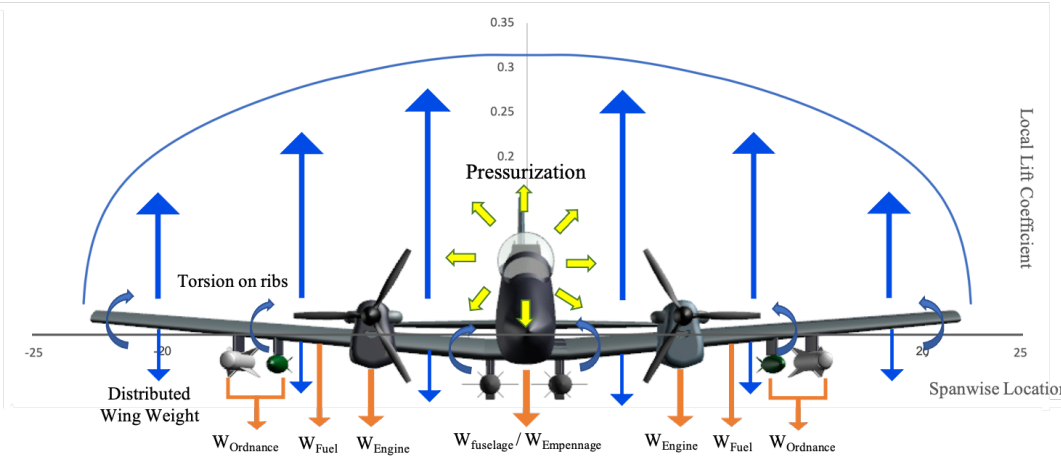

(b) Cruise Load Path

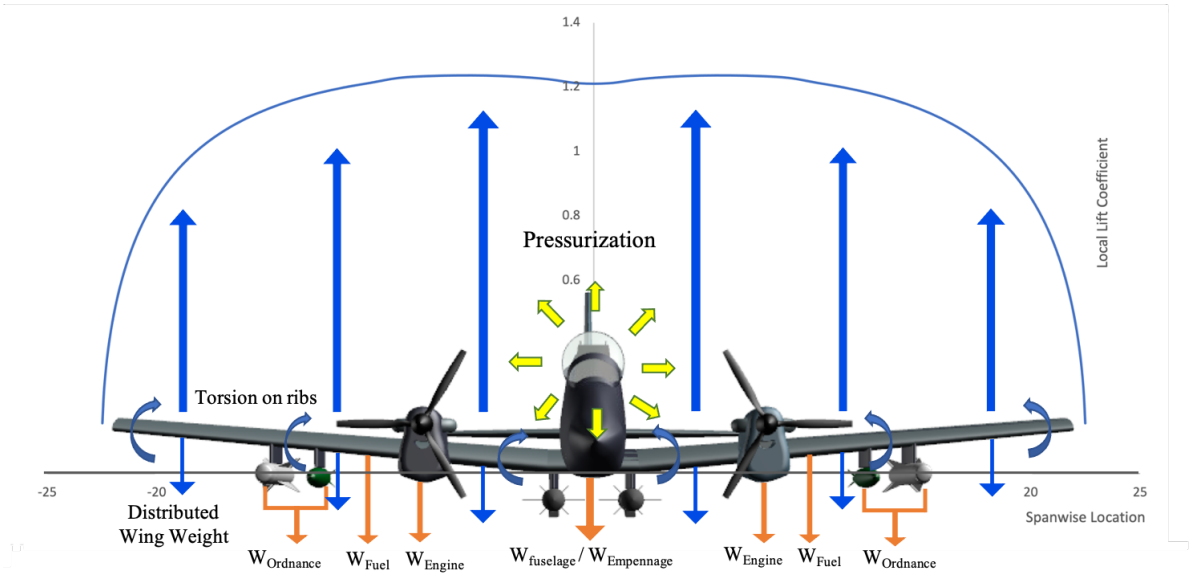

(c) Max Load Path

Figure 37: Load Paths

9.2 Material Selection

Material selection is crucial to ensure the survivability of the aircraft. A few considerations for survivability include an armored cockpit and engine as well as tougher materials to withstand damage. Additionally, survivability includes surviving the elements during the 15,000 hour service life over 25 years. The aircraft is expected to encounter sand, dust, salt spray, heat, ice, and more. Key material properties taken into account are density, tensile strength, elastic modulus, and corrosion. Each material was chosen carefully to account for mechanical, thermal, and environmental conditions.

9.2.1 Aluminum Alloys

Compared to other market-available materials for aircraft construction, aluminum alloys are the most common, and they are a reasonable selection due to their high strength to weight ratio, low cost, and resistance to UV damage. The proposed aircraft must withstand corrosive environments, so high corrosion resistant aluminum alloys appear to be an excellent choice for interior and exterior components. The two main aluminum alloys chosen for the Gunbus structures are aluminum alloy (AL) 6061 and 7075. AL 6061 is common for light aircraft because of its lightweight and high strength [34]. AL 7075 has high strength to mass ratio, which makes it perfect for military aircraft that function in tough conditions. Some material specifications of the aforementioned aluminum alloys are listed below in Table 9. Majority of the aircraft skin is made with AL 6061 while the internal structure of the aircraft, such as wing spars, ribs, fuselage frames, and stringers, are made with AL 7075.

Table 39: Material Selection

Material	Density, lb/in^3	Tensile Strength, KSI	Elastic Modulus, KSI	Thermal Expansion Coefficient, μin/in-°F
AL 7075	0.102	83	10,400	23.2
AL 6061	0.0975	35	10,000	23.6

9.2.2 Composites and Other Metal Alloys

Composites have seen a rise in popularity in recently years as an aircraft construction material. Military aircraft typically have strenuous requirements for mechanical, thermal, chemical and ballistic properties. Composites offer a reduction in weight while maintaining high strength in its structures. Fiber reinforced plastic composites and fiber metal laminates with titanium and carbon are commonly used in aircraft construction. Fiber metal composites have higher thermal properties and are used for high thermal and mechanical loaded components of the aircraft. The downside to using composites as a build material is that

the mechanical treatment and repair of composites is more difficult than common metal material used in aircraft construction. Tooling, machining and cleaning mistakes could cause local delamination and material degradation. From market research on modern light attack aircraft, carbon-plastic reinforced composites are chosen as the build material for the pressure flat plates in the fuselage, the cockpit floor, and the canopy frame. Boron composites are used for the vertical stabilizer to provide greater structural strength because the single-spar design for the vertical stabilizer design prevents structural redundancy. Hence, Boron composites can provide increased structural stability while keeping it lightweight. The canopy material is acrylic polycarbonate composites. [35] Fiberglass is chosen as the nose radome material to protect sensitive instruments inside while allowing electronic signal communication to come through.

Metal alloys other than aluminum are considered, such as titanium for armor and steel for landing gear. Armor is placed around the cockpit to protect the avionic suite and the pilots. Armor around the engine is essential to provide critical protection. The nacelle skin is made with titanium alloy, the same material as the cockpit armor. Because landing gears support the weight from the entire aircraft, steel is chosen as the build material for its robustness and sturdiness. A map of the materials employed and specific skin thickness for each location is shown in Figure 38.

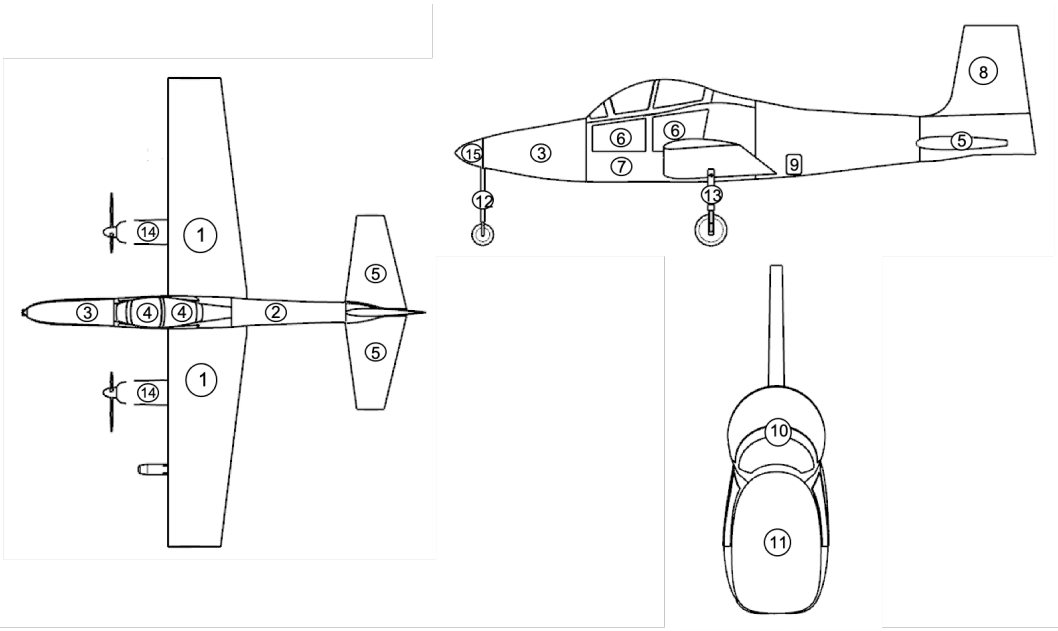

Number	1	2	3	4	5	6	7	8	9	10	11	12	13	14	15
Area	Wing Skin	Aft Fuselage	Nose Fuselage	Canopy	Horizontal Stabilizer	Cockpit Armor	Cockpit Skin	Vertical Stabilizer	Boarding Ladder Cutout	Canopy Frame	Pressure Flat Plates & Floor	Nose Gear Struts	Main Gear Struts	Nacelles	Nose Radome
Material	AL 6061	AL 6061	AL 6061	Acrylic Laminate	AL 6061	Titanium Alloy	AL 7075	Boron Composite	AL 7075	Carbon-Plastic Composite	Carbon-Plastic Composite	Steel	Steel	Titanium Alloy	Fiberglass
Skin Thickness (in)	0.0701	0.068	0.068	0.75	0.06	0.25	0054	0.05	0.25	0.06	0.24	3	5	0.25	0.1

Figure 38: Aircraft Skin Thickness and Build Material Map

9.3 Structural Arrangement

A detailed Computer Aided Design (CAD) model was constructed with complete internal structural components, such as the fuselage, wing, horizontal stabilizer, and vertical stabilizer. The initial sizing process of critical structural components was completed using numerical estimation. The first iteration of structural design was then be improved using analytical methods, such as finite element analysis to substantiate the results of aircraft structural integrity. Each of the structural component is expected to satisfy the success criteria through the full flight envelope.

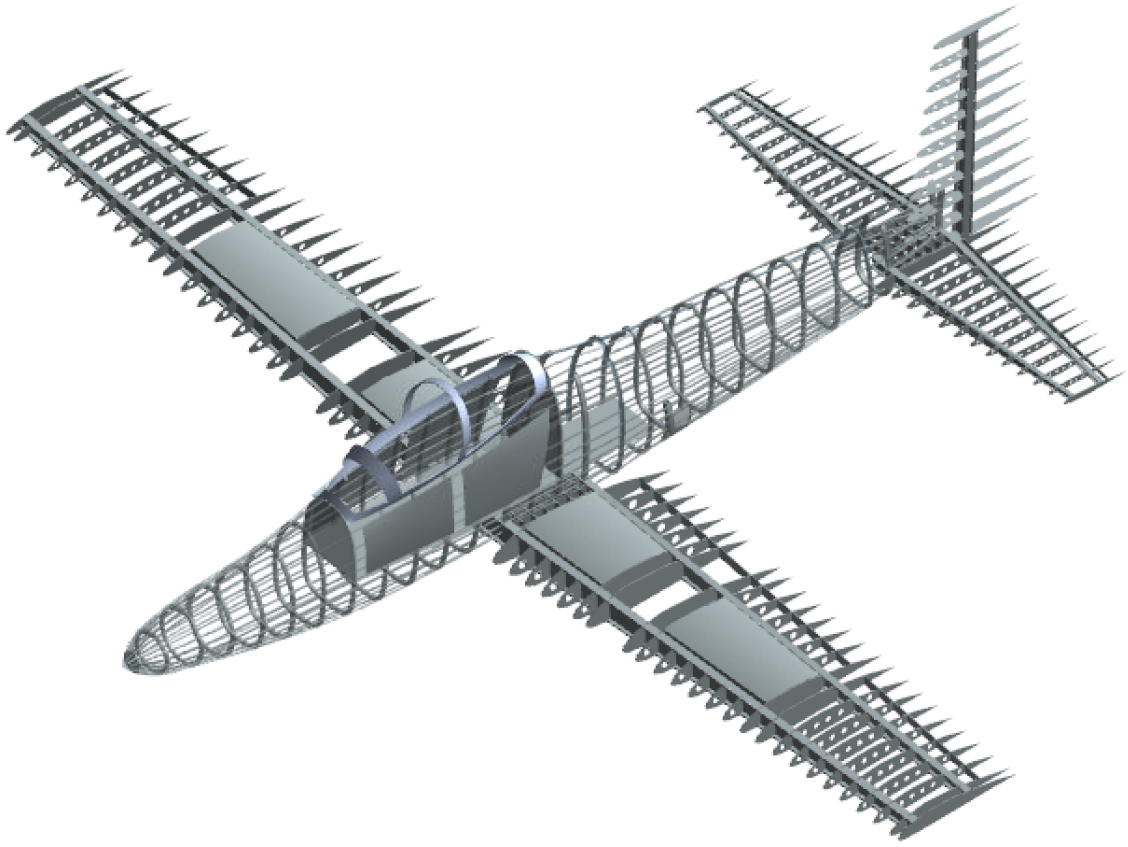

Figure 39: Complete Aircraft Internal Structure

9.3.1 Wing Structure

The primary structural design objective is to define the general layout. The wing box structure consists of the front spar, the rear spar, and ribs as shown in Figure 40. The ribs are designed in the direction of the flight path in order to ensure a smooth aerodynamic shape between the spars. Reinforced ribs are place at attachment points along the wing for control surfaces, torque box, fuel tanks, and nacelles. The spar location is approximated during the initial design phase to accommodate for requirements from the control

surfaces, electrical systems and hydraulic systems design. Fuel tanks take up approximately 40 percent of the wing volume to accommodate for 2,020 lb of JP-8 fuel (density 6.47-7.01 lb/gallon). The front spar is located at 15 percent chord and the rear spar is located at 60 percent chord, leaving sufficient space behind the rear spar for the aileron and flaps and between the front and rear spar for fuel tanks.

I beam geometry is chosen for the spars. The I beam cap experiences bending stress and the I beam web experiences shear stress. The spars are initially sized using methods outlined in Howe chapter 15 [36]. Spar size can be approximated by idealizing the wing box as a rectangular cross section where the airfoil depth at front and rear spars are denoted as h_1 and h_2 respectively. The load distribution on the front and rear spar can be calculated around the centroid of the wing box. It was found that the front spar carries 58 percent of the vertical load while the rear spar carries the other 42 percent. Using the ultimate moment value calculated previously for airloads and the maximum allowable bending stress, and the maximum tensile stress of the airframe build material, an optimal spar flange area is found. The spar web thickness is approximated using the net shear flow in the webs and the maximum shear stress of the material. The bending stress on the spar cap and shear stress on the spar web have to be less than the ultimate tensile strength of the spar material. The initial theoretical size was then substantiated through an iterative process using Matlab. The spar geometry is outlined in Table 40.

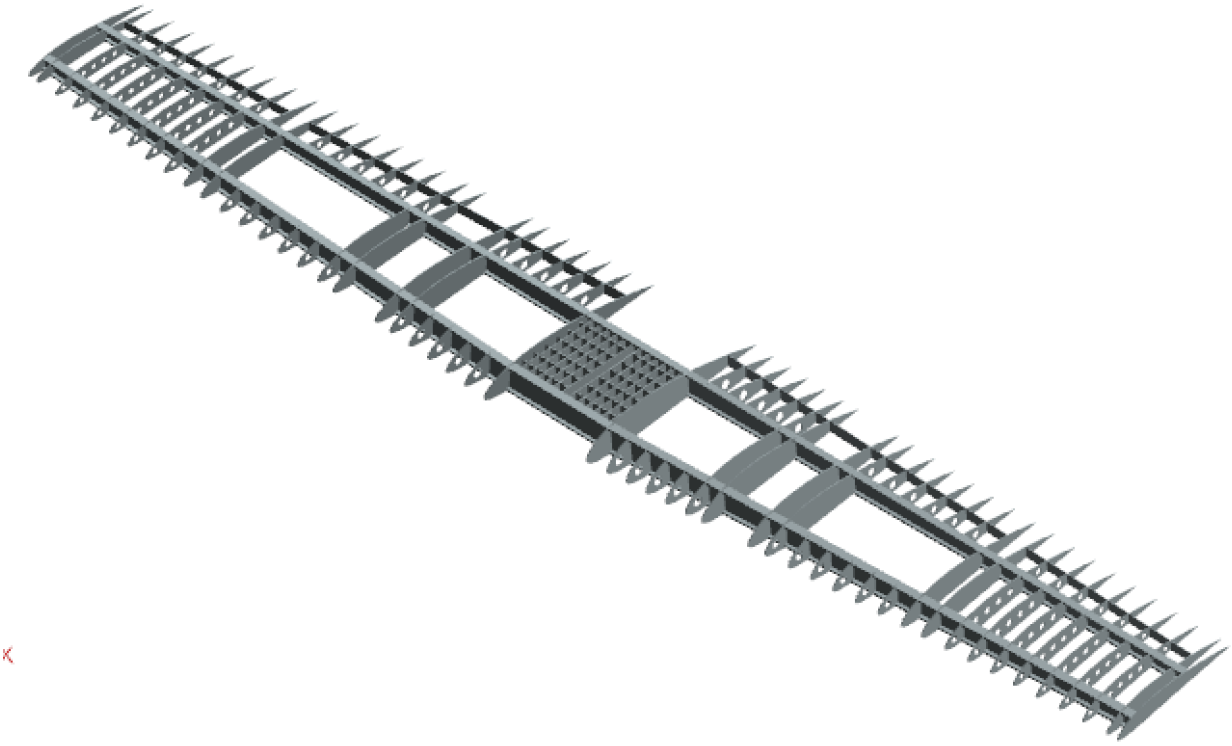

Figure 40: Wing Structural Layout

Table 40: Spar Sizing

	Spar Cap Width, in	Spar Cap Depth, in	Spar Web Thickness, in	Spar Height, in
Front	1	4.465	0.865	12.1
Rear	1	3.801	0.415	10.3

Table 41: Rib Sizing

Rib Thickness, in	Reinforced Rib Thickness, in	Average Rib Spacing, in	Lightening Hole Diameter, in
0.250	0.353	9.487	2.5

Wing bulkheads are constructed as solid ribs or ribs with access holes and trusses. Wing ribs are support members but also carry external air loads, inertial loads and crushing loads due to flexure bending. The wing structure has 50 ribs, and the rib spacing is non-uniform to accommodate the attachment points for control surfaces, engine mounts, as well as fuel tanks. Reinforced ribs are placed at those attachment points to provide structural support. The thickness and spacing of the ribs was determined using methods outlined in Howe chapter 17 [36]. Lightening holes were implemented to reduce weight of the wing while maintaining the structural integrity of the component. Rib geometry can be found in Table 41. A diagram of the wing cross section is shown in Figure 41 to provide visualization of the spar and rib sizing.

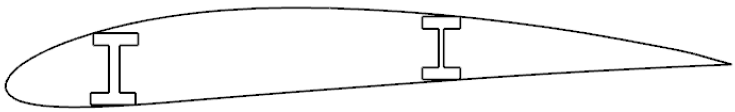

Figure 41: Wing Cross Section

The wing skin thickness is 0.0701 inches, determined from methods in Niu [37] as an initial estimate for structural design. Wing skin thickness take into account of the skin and the stringer structure. Typically the effective skin thickness due to the stringers is between 50 and 100 percent of the skin, depending upon the form of construction and the load intensity. Assuming the lower value, the actual skin thickness needed in the bending case is approximated using Equation 3, where h is the wing box depth, w is the wing box width, and σ_b is the maximum allowable stress of the wing skin material. Finite element analysis was conducted to determine the minimum skin thickness at critical locations.

$$t_{skin} = \frac{0.5 M_{ult} y}{h w \sigma_b} \tag{3}$$

9.3.2 Fuselage Structure

The fuselage structure consists of the fuselage skin, frames, frame bulkheads, pressure bulkheads, and stringers, as shown in Figure 42. Stringers carry the majority of the bending moment on the fuselage. The fuselage skin carries the shear from external transverse and torsional forces, as well as cockpit pressure. The frames are used to maintain the fuselage shape and are generally much smaller in size when compared to fuselage bulkheads. Frame bulkheads are placed along the fuselage at attachment points where concentrated loads from the wing, tail, and landing gear are located. The bulkheads redistribute the applied load onto the fuselage skin. Two flat-plates are used as pressure bulkheads at the front and rear of the cockpit to carry the pressurization loads onto the fuselage. The cockpit is pressurized to δ_P at cruise altitude of 15,000ft. The required thickness for the pressure plates to carry the pressurization load is calculated using equation 4.

$$t_{plate} = \sqrt{0.71\Delta_P^2(n^3/(n^3+1.5))\sigma_a} \tag{4}$$

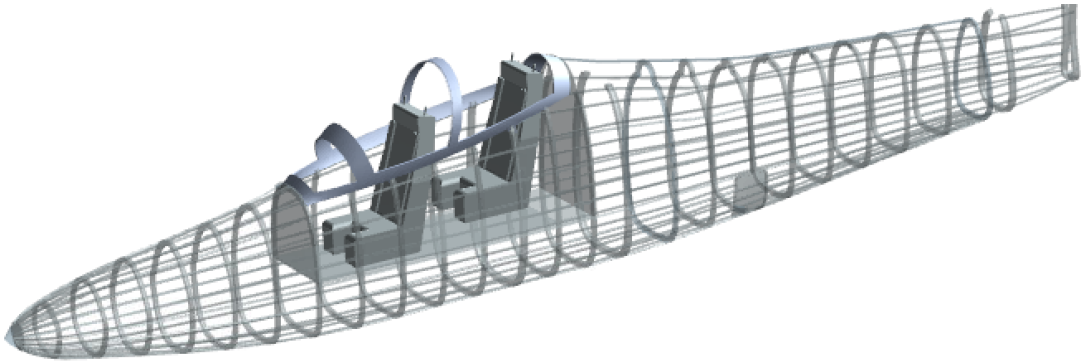

Figure 42: Fuselage Structural Layout

The fuselage frame sizing parameters were determined using imperial methods from Howe chapter 15 [36] for initial structural design. Bulkhead frames are used in the fuselage structure at locations where the wing and the horizontal stabilizer are attached. These locations have large concentrated loads, therefore requiring hefty frames to carry the extra loads. The most common stringer shapes are Z shape and I-blade shape, the latter is especially associated with simple integrally machined panels. Stringer pitch is conventionally between 1.5 and 5 times the stringer height, the lower values is typically associated with blade stringers. The Z stringer configuration is chosen for the fuselage. In the case of separate Zed-section stringers the width of each of the shorter flanges is often about 40 percent of stringer height, giving a total cross-section area of $(1.8 * h * t)$ where h and t are the stringer height and thickness, respectively. The fuselage frame and stringer geometry is outlined in Table 42.

Table 42: Fuselage Sizing

Frame Cross Sectional Area, in^2	Frame Spacing, in	Bulkhead Cross Sectional Area, in^2	String Cross Sectional Area, in^2	Stringer Spacing, in
2.24	15	4.20	1.44	6

9.3.3 Empennage Structure

The empennage structure was constructed similarly to the wing structure. Preliminary sizing process used similar methods as the wing structure. The front and rear spars are located at 15 percent and 60 percent of the horizontal stabilizer chord respectively, leaving sufficient space for control surfaces. However, a structure design risk was made for the vertical stabilizer to accommodate for the rudder geometry. The rudder surface area would account for roughly 50 percent of the vertical stabilizer; therefore, a single spar configuration was chosen for the vertical stabilizer structural. The main spar is placed at 42 percent chord to accommodate the rudder design and leave sufficient space for control surface electrical system. The vertical and horizontal stabilizer are mounted onto the tail through bulkhead frames in the fuselage structure. The empennage structure is shown in Figure 43. The horizontal and vertical stabilizer are shown separately in Figure 44.

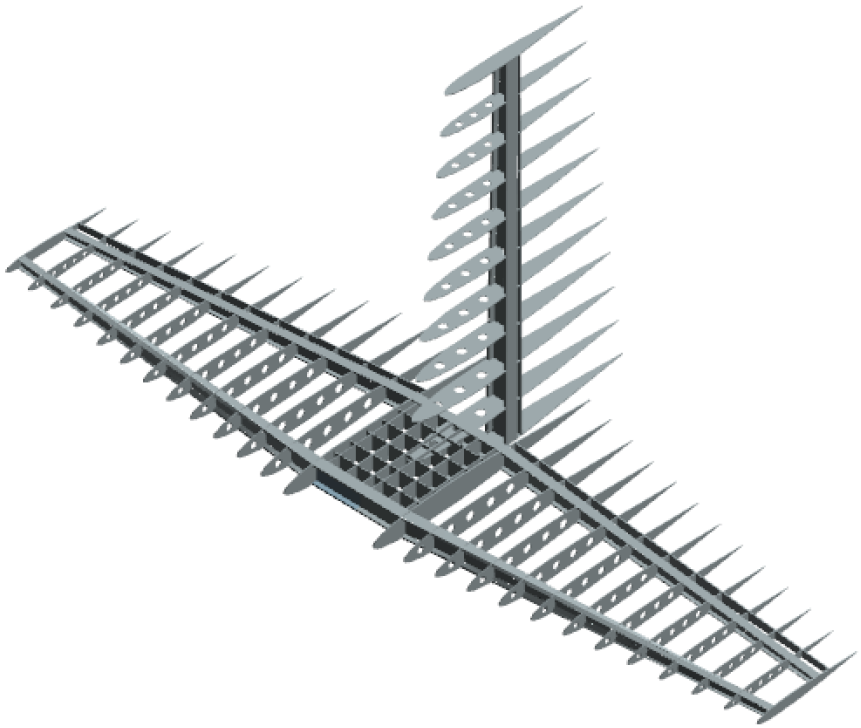

Figure 43: Empennage Structural Layout

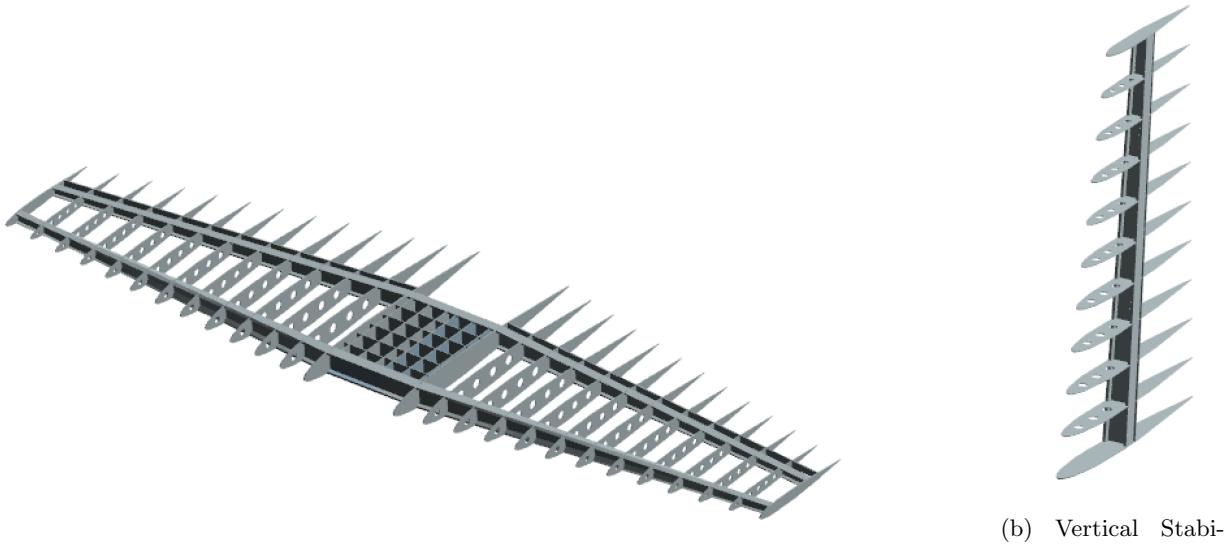

(a) Horizontal Stabilizer Structure

(b) Vertical Stabilizer Structure

Figure 44: Empennage Layout

9.3.4 Attachment Points and Mounting Mechanism

Several attachment points are critical in structural design of the aircraft. The front and rear spars of the wing are extended through the fuselage and mounted to the fuselage frame bulkheads. At this attachment point where the wing is bolted to the fuselage, the aircraft experiences the largest bending moment and shear force. Similarly, the horizontal stabilizer has a wing box design that goes through the fuselage. At those attachment points for the empennage to the fuselage, bulkhead frames are used to ensure the structural strength. The nacelle and fuel tanks are mounted on the wing. At the points where the fuel tanks and the nacelle are mounted, solid reinforced ribs with a bigger thickness are used to take on higher concentrated loading.

9.4 Landing Gear

The landing gear configuration was chosen to be a tricycle setup. This is the best option for both missions because of good visibility during taxi and enhanced handling, particularly on paved runways. While the RFP dictates the need for operation on austere fields, a tricycle gear arrangement performs well enough on unpaved runways and is much better than possible alternatives on paved runways, which will still see major use. A tricycle gear also allows for easier loading of ordnance as the aircraft is in a level attitude on the ground, which enhances mission readiness and reduces unloaded scramble time. This configuration also allows for main gear stowage in the engine cowlings, taking advantage of otherwise unused space.

The length of the gear was dictated by specific constraints, the most important of which is the tipback

angle. This angle ensures tail ground clearance during the takeoff and landing phases, and should be no less than 15 degrees [17]. Similarly, the turnover angle is the maximum lateral angle that the aircraft is able to tip without striking the ground. This angle is equal to 55 degrees for our aircraft, which is below the 63 degree maximum [38]. Tire sizing was determined after research into the tire dimensions of aircraft with similar austere field performance.

Table 43: Gear Specifications

Parameter	Value
Nose Wheel Diameter, in.	17.50
Nose Wheel Width, in.	6.75
Nose Strut Length, in.	54.00
Nose Tire	Type III
Main Wheel Diameter, in.	26.56
Main Wheel Width, in.	8.70
Main Strut length, in.	37.00
Main Tire	Three-Part

Because of the fuel tank configuration, it was not possible to retract the gear sideways into the wings. It was therefore deemed necessary to stow them inside the engine nacelles. For proper stability on the ground, the gear also needed to be mounted 15 degrees or more behind the aft C.G. limit.

To adequately fit into the nacelles, the gear retracts forward and features a 90 degree rotation about the strut axis using two ball joints, coming to rest under the engines with the wheels facing downwards. The extended and retracted main gear positions are shown in Figures 45 and 46 below.

For minimum acceptable steering, the nose wheel static load should be no less than 8% of MTOW [33]. This was achieved by placing the nose gear directly under the nose of the aircraft. In this position, the nose wheel load is 1,155 lb and the main wheel loads are 6,646 lb each.

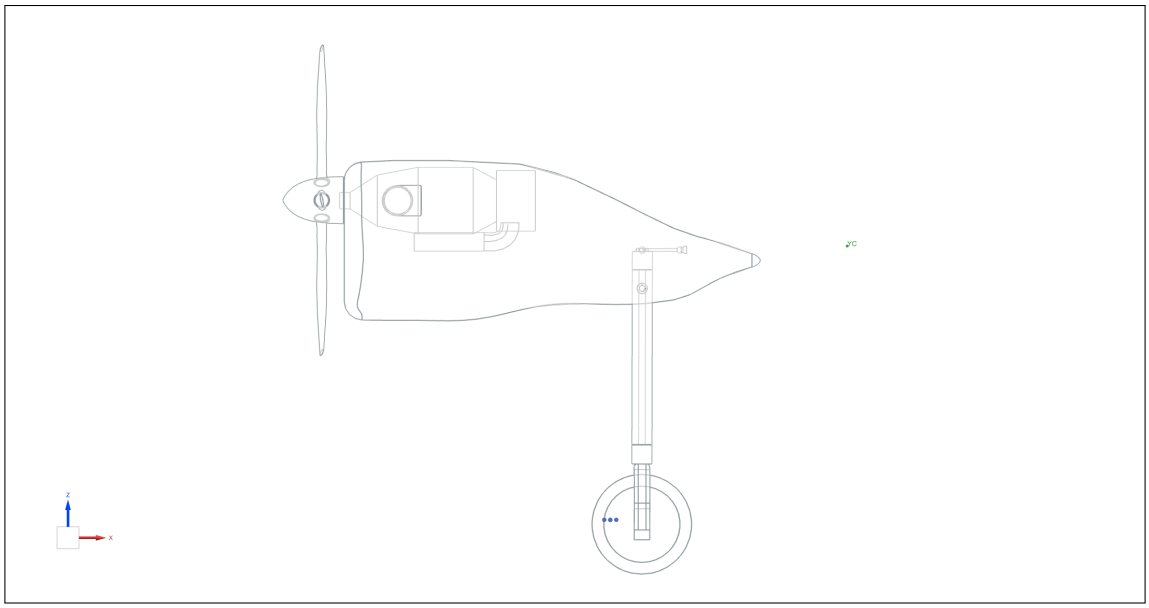

Figure 45: Extended Main gear

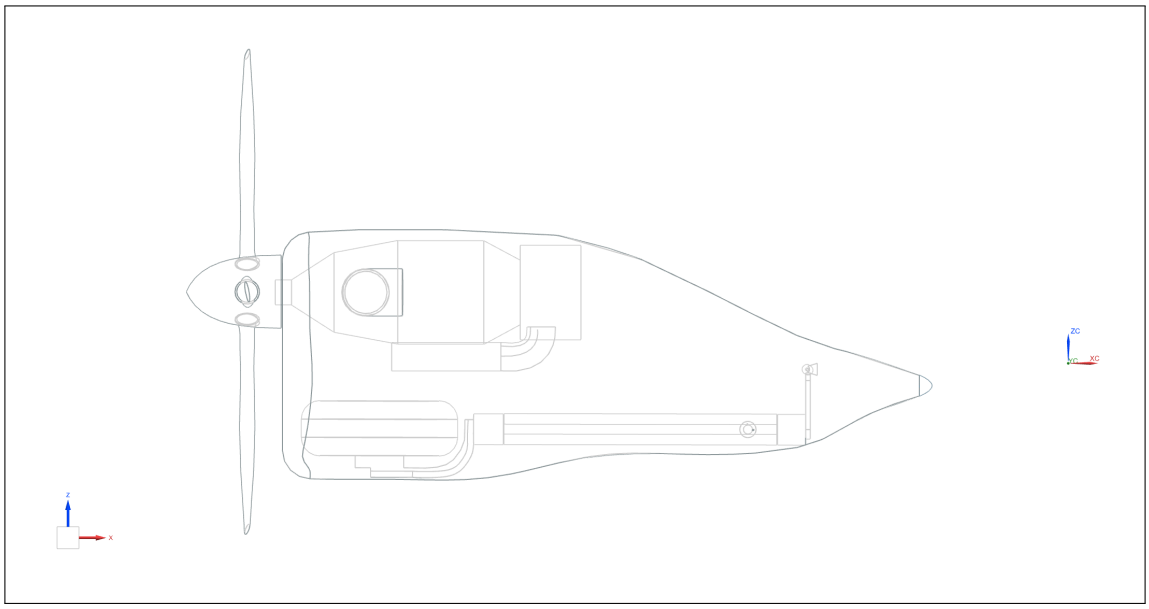

Figure 46: Retracted Main gear

9.5 Finite Element Analysis

As mentioned in previous sections, the internal structure preliminary sizing were approximated values dependent on the idealized wing box ultimate bending moment and ultimate shear stress. Using the Shrenk's method calculation for lift, a theoretical deflection plot was generated across the the spar, shown in 47. This theoretical value was obtained by idealizing the wing structural as a simple cantilevel beam where the moment

of the inertia of the wing is obtained using equations 5 and 6. Modeling the deflection of the wing provides analysis into the structural integrity of the wing design. If the theoretical results look unreasonable, it would warrant further investigation into the structural preliminary sizing process to ensure no mistakes were made. Therefore, the theoretical delfection along the spar serves as a sanity check as well. The max deflection is 16.62 inches located at the tip of the wing. The results do not account for the effects from wing skin on the overall wing structural deflection.

$$\sigma_b = \frac{M_{ult} y}{I} \tag{5}$$

$$\tau_b = \frac{V_{ult}}{t_{web} h} \tag{6}$$

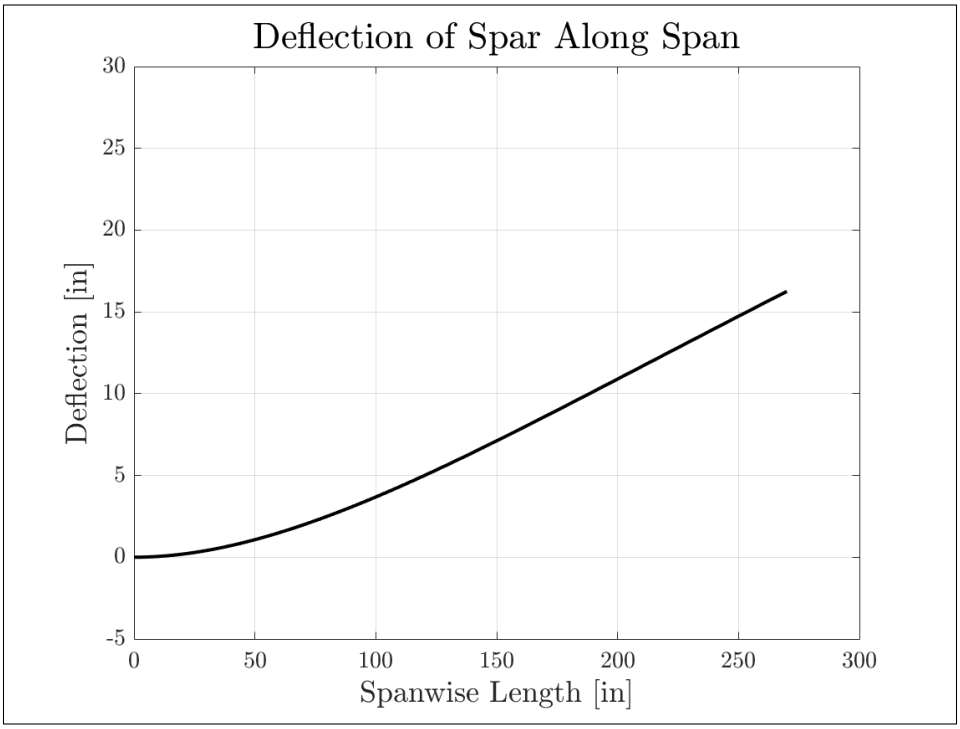

Figure 47: Theoretical Wing Deflection

To substantiate that the theoretical geometry calculations could withstand the maximum amount of load expected in the maneuver V-n diagram, a finite element analysis was conducted. The wing structure on the right side of the aircraft from the fuselage to the wing tip was extracted and imported into Siemens NX for stress and displacement analysis. As shown previously in section 9.1.2 the wing structure experiences the most bending moment and shear stress at the location where the wing interfaces with the fuselage. Thus, only structure from the interface point to the wing tip was necessary for analysis. A fixed constraint was

placed at the wing root to emulate the constraint from fuselage on the wing. The max load lift distribution outlined in section 9.1.4 was modeled as a pressure field in NX and applied to the top surface of the wing skin. Along with lift, point forces were placed at the location of the nacelle, fuel tanks, and ordnance to represent their effects on the structure during flight. A visual representation of these forces on the wing can be found in 37c from section 9.1.4. The wing deflection and stress throughout the wing span were then obtained using the Nastran Solver as shown in Figures 48 and 49. The finite element analysis results shows that wing deflection is greatest at the wing tip and and the shear stress is the greatest at the root of the wing, similar to that of the theoretical results. The deflection at wing tip seen in the wing deflection plot is 7.135 inches.

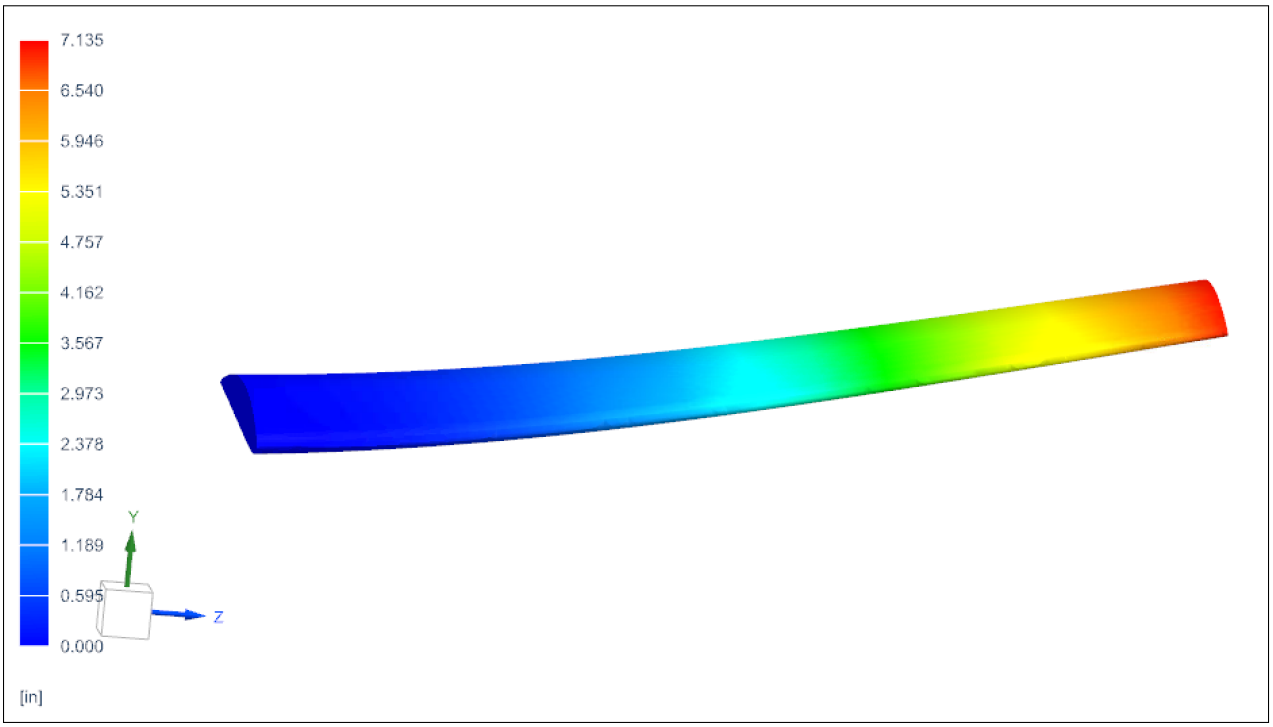

Figure 48: FEA Wing Deflection Plot

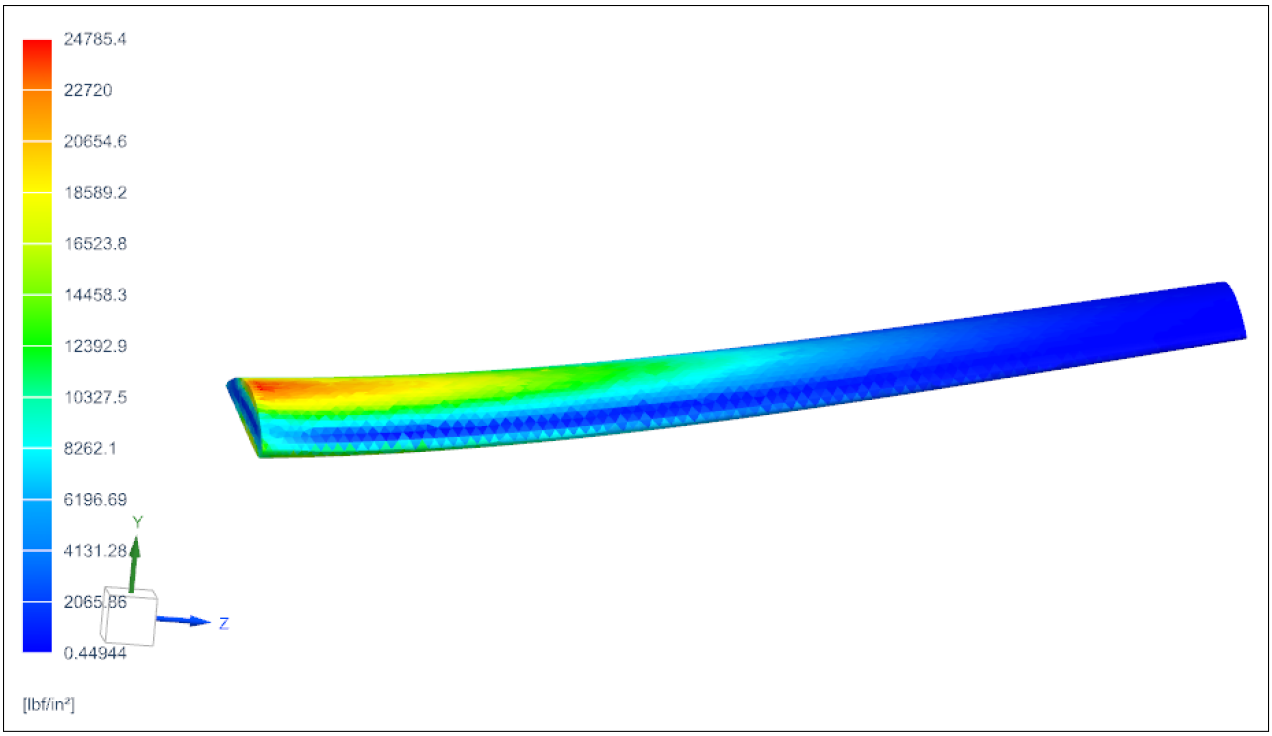

Figure 49: FEA Stress Plot

Compared to the deflection results from finite element analysis, the theoretical calculation has a 132 percent error. A few things could attribute to the high percent error. First, the theoretical calculation only take into account of the wing internal structure while the finite element analysis computer aided design model is the overall structural including internal components and the wing skin. As explained in Roskam [39], the wing skin is responsible for carrying up to 50 percent of the wing loading. Secondly, the theoretical calculation assumed a simple cantilever beam geometry and excluded effects from wing stores; therefore, the center of gravity calculation and weight of the wing structure would be inaccurate.

10 Mass Properties

10.1 Weight Buildup and Analysis

At this stage in the design process, a complete weight buildup of all major assemblies and their respective center of gravity locations is necessary. This exercise allows the team to understand where the major contributors of weight are and if the aircraft is properly balanced under worst case conditions. Three methods were used to gather weights for the reported weight buildup. The first method is with direct usage of existing components, where exact weights are known. This method was used for the fixed engine, ordnance, and some subsystems. The second method is with empirical calculations, primarily using equations found in

chapter 15 of Raymer [22]. This method was useful for the landing gear, avionics, and other miscellaneous components. The last method is direct measurement in CAD. Components were given material assignments, and weight was directly found. This technique was especially useful for structural components and the horizontal and vertical tail. A summary of the aircraft weights and C.G. locations is provided in Table 44.

Table 44: Weight and C.G. Estimates

Component	**Quantity**	**Total Weight, lb**	**C.G. (x), in**	**C.G. (y), in**	**C.G. (z), in**
Fixed Components					
Wing Structure - Including Flaps	1	2,088	197	0	2
Fuselage Structure	1	1,196	190	0	7
PT6A Engines with Propellers	2	916	130	0	6.5
Fuselage Skin and Paint	1	478	190	0	7
Fuselage Armor	1	450	140	0	5
Aft Landing Gear (In Flight)	2	408	205	0	-6
Engine Gearboxes with Accessories	2	390	154	0	7
Wing Skin and Paint	1	384	197	0	2
Horizontal Tail	1	327	433	0	4
Ejection Seats	2	300	140	0	25
Integrated Gun	1	250	80	0	0
Avionics	1	250	138	0	18
Front Landing Gear (In Flight)	1	220	50	0	-6
Hinged Canopy	1	204	140	0	30
Hydraulic Controls	1	200	214	0	2
Nacelles	2	180	146	0	6.5
Vertical Tail and Rudder	1	157	429	0	31
Engine Armor	1	150	190	0	5
Ordnance Mounting	5	150	200	0	-6
Auxiliary Power Unit	1	100	300	0	0
Oil and Lubricants	1	51	195	0	6
Heat Exchanger / AC	1	30	240	0	4
Electrical Controls	1	60	214	0	2
Nose Cone	1	20	4	0	0
Fuel Lines	2	20	200	0	4
Removable Components					
Full Fuel Tanks	4	2020	200	0	-1
M3P Gun Pods (With Missiles)	4	1404	199	0	-10
Delilah Missiles	2	1000	186	0	-22
Integrated Gun Ammunition	750	450	80	0	0
Crew	2	340	140	0	25
Crew Baggage	1	50	80	0	3
Aircraft (Empty)	**1**	**9,183**	**187**	**0**	**5.5**
Aircraft (MTOW)	**1**	**14,447**	**185**	**0**	**1.5**

The weight buildup shows the aircraft has a MTOW of 14,447 lb and an empty weight fraction of 63.5%. This is consistent with the estimations in Raymer, chapter 3, for a twin turboprop aircraft. For reference, the Super Tucano has an empty weight fraction of 59%.

The next step was to analyze every possible aircraft C.G. as the removable components are added or removed. At every combination, the aircraft must stay within its acceptable C.G. range. The envelope for worst case C.G. combinations are shown in Figure 50.

Simultaneously, the C.G. envelope was verified to fall within acceptable limits. The C.G. must be forward of both the neutral point and the rear landing gear. If the aircraft C.G. falls aft of the neutral point, it will become unstable during pitch. If the C.G. is aft of the rear landing gear, the aircraft will tip while on the ground. Oppositely, the aircraft C.G. cannot be too far forward, or else the aircraft cannot pitch upwards during takeoff. The aircraft neutral point was found using the aerodynamic model in XFLR5, the landing gear position was verified with CAD, and the maximum forward C.G. limit was found using the aircraft moment equation with a flap angle of 30 degrees. The results are shown in Figure 50.

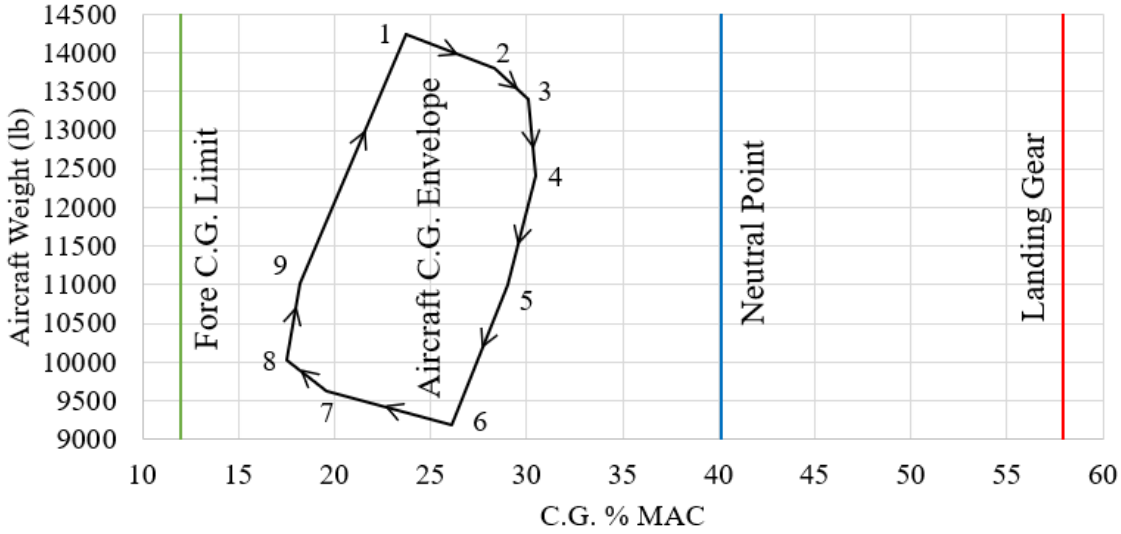

1	MTOW	6	Empty Weight
1 – 2	Remove M-197 Ammunition	6 – 7	Add M-197 Ammunition
2 – 3	Remove Crew / Baggage	7 – 8	Add Crew / Baggage
3 – 4	Remove (2) 500 lb Missiles	8 – 9	Add (2) 500 lb Missiles
4 – 5	Remove Wing Mounted Ordnance	9 – 1	Add Ordnance and Fuel
5 – 6	Remove Fuel		

Figure 50: C.G. as a Percentage of MAC for All Combinations

As shown, the current configuration is viable. The C.G. location falls within the acceptable limits during worst case loading conditions as shown in Figure 50. The MTOW C.G and C.G. limit locations are shown on the aircraft in the following figure as a reference.

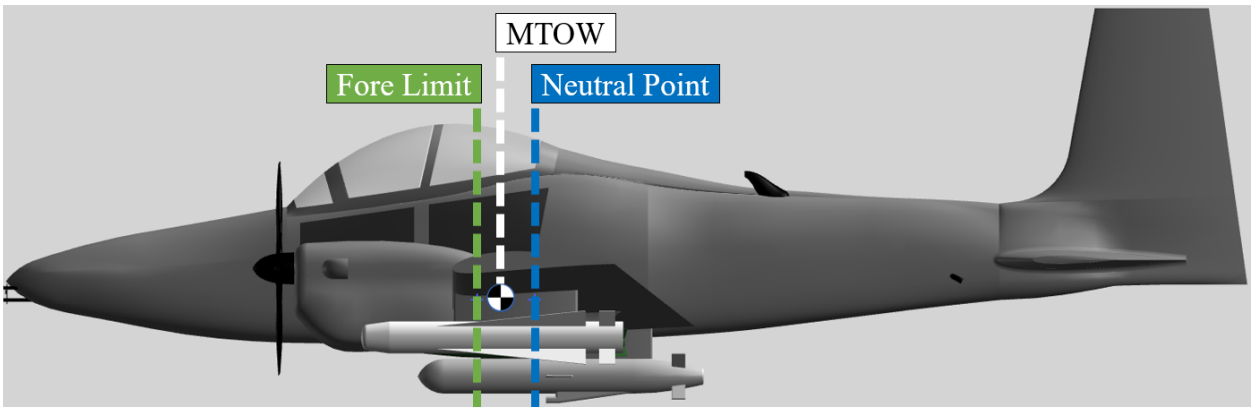

Figure 51: Aircraft MTOW C.G. and C.G. Limit Locations

10.2 Wing Positioning Design Process

The aircraft C.G. is currently in an acceptable position, but this was not the case during early analysis. The C.G. was originally found to be too far aft when empty, as it was behind the rear landing gear. This led to a study on wing and landing gear placement. The landing gear was generally constrained, as it was constrained to being positioned on the wing and retracted into the nacelle. Thus, it was necessary to move the wing. However, the engines were relatively fixed with respect to the wing, and the turboprop propeller blade could not be less than 5 degrees forward of the canopy due to safety concern. This meant the wing could only move so far aft before encountering safety issues. As a compromise, the wing was moved aft 2 ft, the engine was moved 1 ft forward with respect to the wing, and the landing gear was moved aft 1 ft with respect to the wing. Table 45 shows the original configuration vs the current configuration.

Table 45: Original vs. Current C.G. and Landing Gear Position

	Empty Weight C.G. (x), in	Landing Gear Position (x), in
Original Design	185	179
Current Design	187	205

11 Auxiliary Systems

11.1 Flight Controls

For flight controls, a primary and secondary system were chosen to provide continuous and reliable control for the aircraft even in the event of failures. For the primary system, fly-by-wire control was chosen for a variety of reasons with the main reasons being weight savings and increased reliability. A fly-by-wire system

is different from traditional flight control which relies on mechanical interfaces between pulleys and cables or push-rods to actuate the control surfaces based on pilot input. For fly-by-wire, the system takes the input that the pilot gives to the stick, and turns it into an electric signal which is processed by a series of flight computers and then sent as signals to the appropriate actuator. These computers, three in this case, consider the state of the aircraft, as well as the air conditions, to provide a calculated actuation of the control surfaces that lead to more efficient and safer flight. More than one computer is necessary for this process in order to provide redundancy in the calculations, as well as a double backup in the case of a single computer failure. Now that the system is defined, its benefits can be accessed starting with weight savings. The replacement of the mechanical components with small signal wires throughout the aircraft leads to considerable weight savings of an estimated 58% for fighter aircraft [40]. Another benefit to fly-by-wire is the reliability and survivability of the system. This benefit is brought about by an increase in the redundancies provided by the computers as well as the opportunity to have multiple wires paths to the actuator in the case of FOD or other types of failure. These wires do not take up the large amount of space that is occupied by pulleys and cables and hydraulic lines and thus provide less chance of being damaged, increasing survivability. The last major benefit is the reduced cost of the system over time. With the lack of mechanical components, the wear and tear on components is reduced, and maintenance difficulty is reduced as the primary location of repair will be only at the actuators. Not only will maintenance cost be reduced but the maintenance difficulty will as well. In most cases, an individual actuator can be easily replaced by "unplugging" the failed actuator and a whole new system may be inserted. This method for repairs also allows for easier operation from austere airfields where large amounts of maintenance equipment may not be available.

As for drawbacks of the FBW system, the main downside is the increase in upfront cost per unit of the aircraft. Because the FBW system is more complex and technologically advanced, the initial cost of installation of the system is much more than traditional, "low-tech" systems. This downside creates a trade off of between the initial cost versus the long-term cost which must be considered. Over a long service life, the initial, increased cost will be negated as the maintainability and upgradability of the aircraft is greatly reduced.

For the secondary system, a two traditional centralized hydraulic systems will be incorporated as it is necessary to incorporate the chosen Electrical Backup Hydraulic Actuators (EBHA) actuators that use a localized hydraulic system which takes input from the FBW signals and has the capability to operate using conventional hydraulics. The incorporation of this secondary system into the overall flight control system, as well as the EBHA actuator system, are shown below in Figures 54 and 52 respectively. Ample redundancy can be seen as the two actuators at each surface draw from different hydraulic systems. This allows the continued operation of any given surface in the case that one of the hydraulic systems fail.

Lastly, in the case that there is a triple flight computer failure, the system will automatically switch to proportional direct control to each actuator as well as to the hydraulics. This fail-safe allows the pilot to bypass the computers and maintain control. This bypass method can be seen in Figure 53.

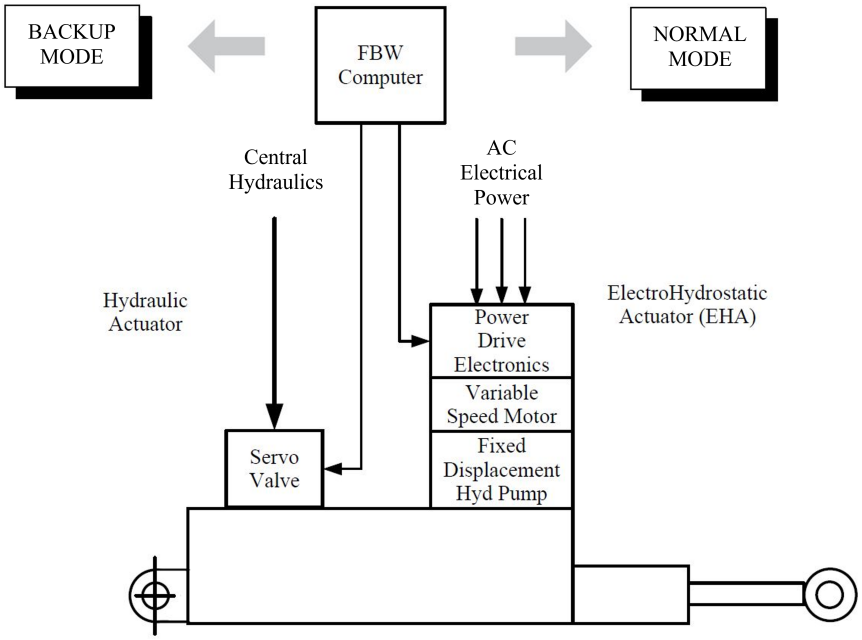

Figure 52: EBHA Actuator Diagram

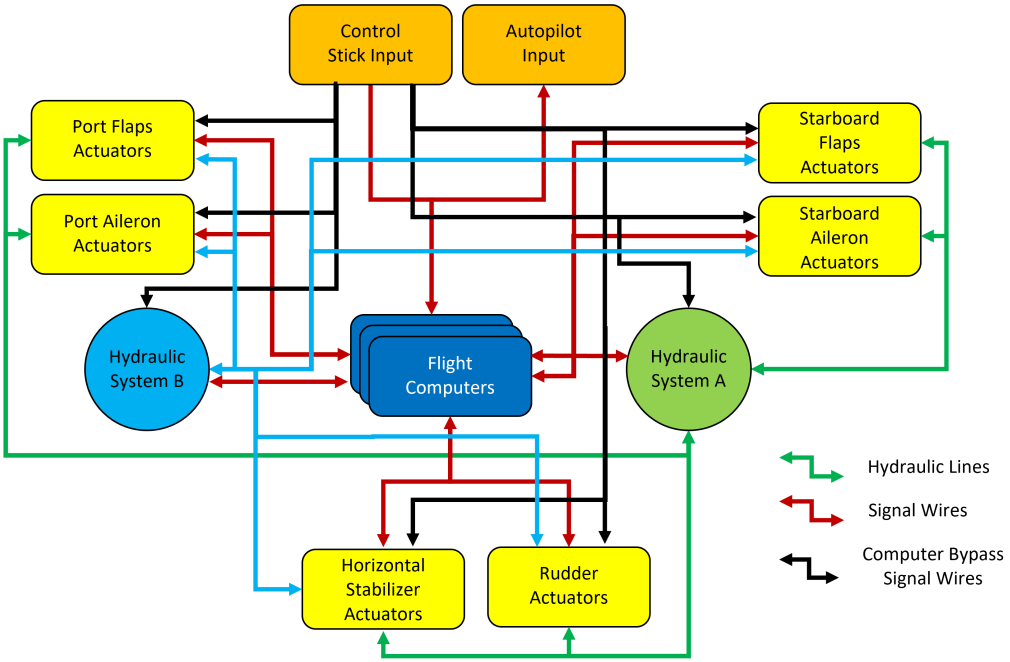

Figure 53: Fly-By-Wire System Diagram

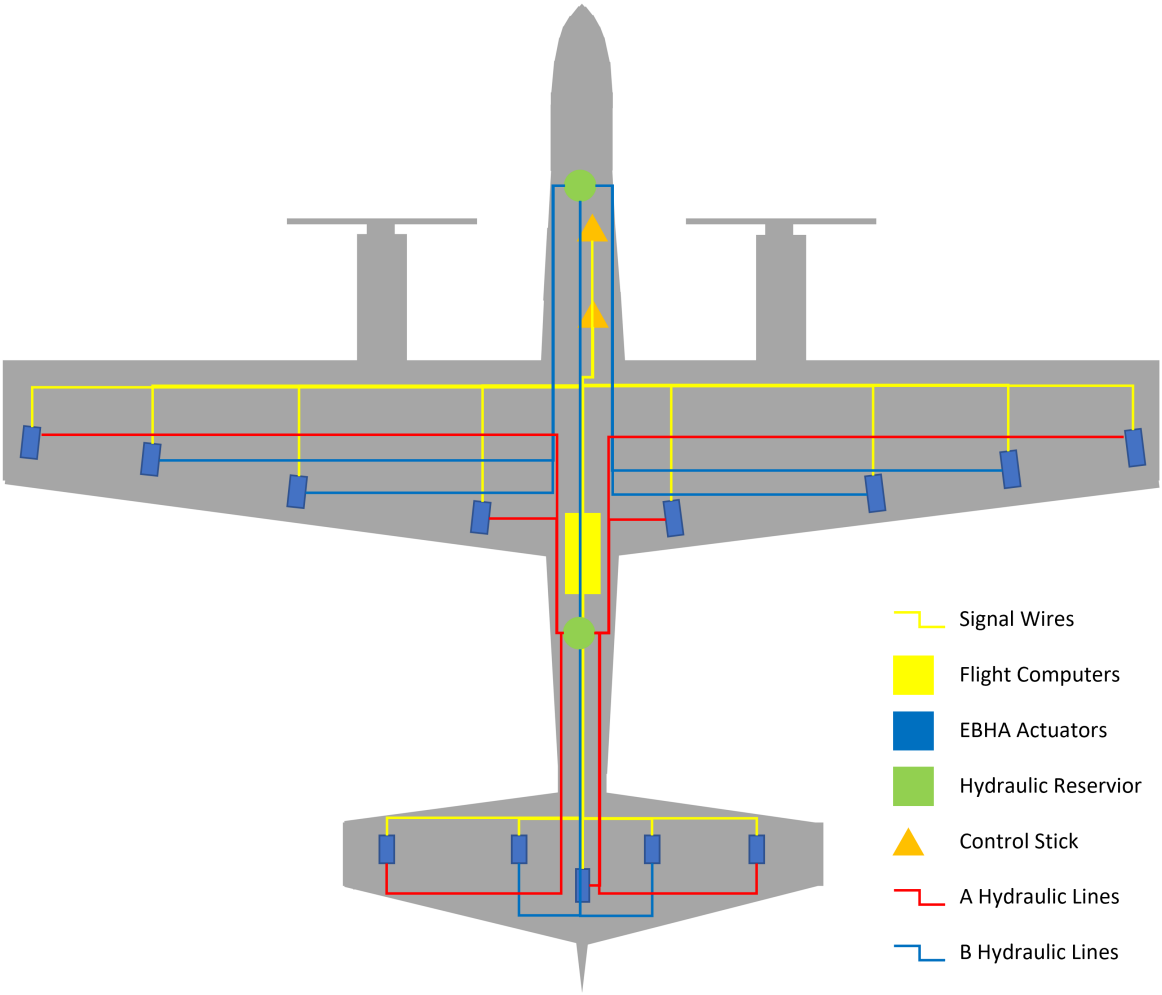

Figure 54: Aircraft Flight Control System Diagram

11.2 Fuel System

The aircraft fuel system is comprised of the fuel tanks that store the fuel during flight as well as the components that monitor and transport the fuel to the engines. Based on the required amount of fuel necessary and the space available in the aircraft, two tanks on each wing were chosen, placed on either side of the engines. This creates a shorter path to the engines as well as provides close placement to the center of gravity, allowing for easy changes to the sizing and placement of the tanks. To provide increased reliability, the fuel from any tank is able to be transferred to any tank as well as able to travel to either engine. The paths that the fuel may travel along as well as the interfaces with the tanks are detailed in Figure 55. A path for fuel to travel to the APU is additionally provided for when the aircraft is on the ground or emergency power from the APU is required. The function of the APU is discussed further in the

electrical system. The other components in the fuel system include volume sensors in the tanks and pumps along every fuel path for the ability to move fuel effectively. Also, for safety, shutoff valves will be placed on the fuel lines throughout the system in order to isolate failures and prevent the leakage of fuel. Additional measures for safety include pressure, temperature, and flow rate sensors throughout the system to allow for accurate monitoring of the system and give the ability to quickly identify failures. In the event of the needing to dump fuel, the fuel system also has the capability to carry fuel to under the tail where fuel can be dumped without interfering with other systems. Due to ever changing mission requirements, the aircraft will be capable of accommodating 50 gallon drop tanks on the outer pylons. The fuel tanks have a combined capability to carry 2,020 lb of fuel which is a volume of 297 gallons. One survivality measure for the fuel system is to add foam to the inside of the tanks, preventing the build up of vapor and mitigating ignition from bullets or FOD entering the tanks. This foam takes up about 5% of usable space, increasing the fuel volume to 312 gallons or 41.7 ft^3. [22]

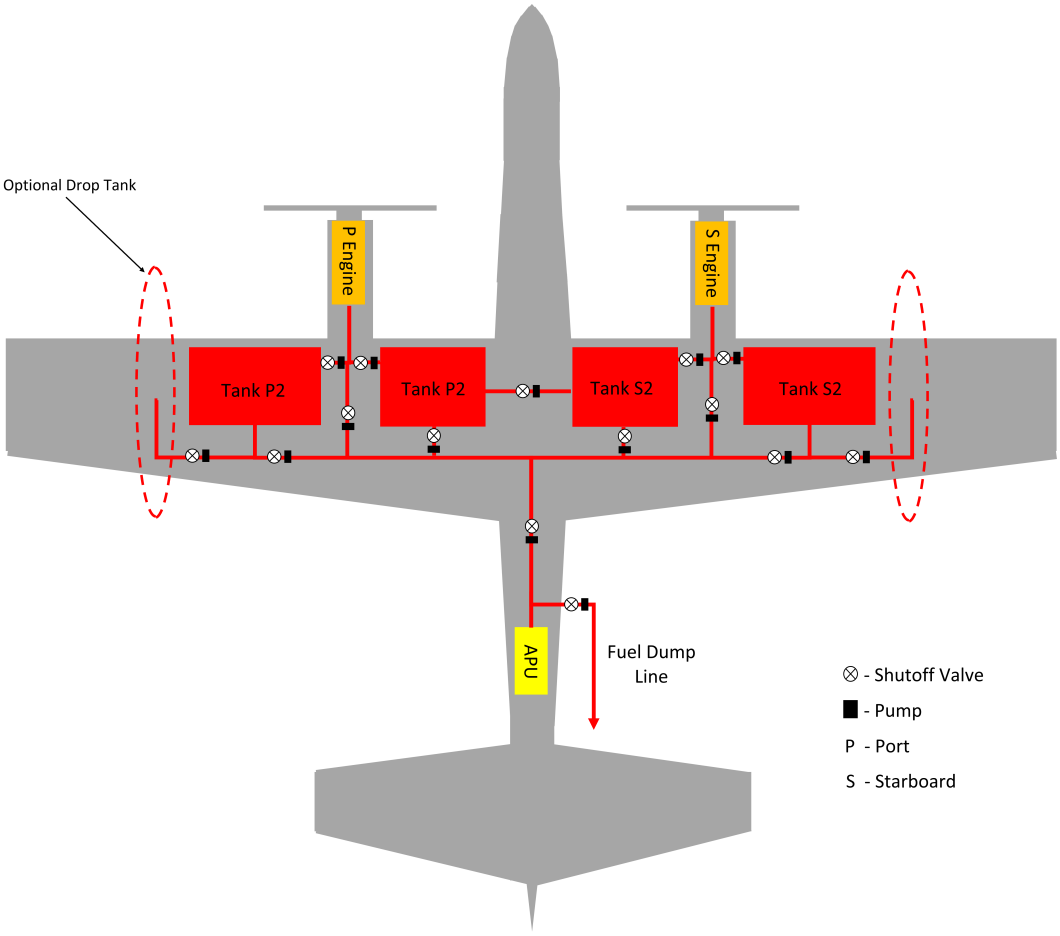

Figure 55: Aircraft Fuel System Layout

11.3 Electrical System

The electrical system for the aircraft is responsible for generating and providing the electrical power to all of the systems throughout the aircraft. These systems include the avionics, the various sensors throughout the aircraft, actuators and pumps. The primary electrical generation source comes from a generator on each engine which convert some of the mechanical energy from the engines and turn it into 115 VAC electrical power. This AC current can be sent to so systems requiring AC power or it can be converted to 28 VDC power through the use of Transformer Rectifier Units (TRU). The secondary method for power generation will come from the installed Auxiliary Power Unit (APU) which serves as a method of power generation when the aircraft is on the ground, enabling power without having to run the engines. The APU is a small jet engine that produces 28 VDC electrical power by consuming some of the aircraft fuel. For this aircraft, the Honeywell Micro Power Unit [41] will be used for its reduced weight and low fuel consumption. This capability leads to fuel savings and increases the ability to operate on austere airfields where ground power may not be available. As a secondary power source, the APU stands as a backup source of electrical power in the case that engine or generator failures occur. Additionally, in the case of double engine failure, a ram air turbine or RAT can be deployed to provide additional power. Under normal flight conditions, the RAT is retracted into the aircraft and is only exposed in case of emergency. Also as a means of emergency power, a primary and backup battery has been sized for the case of needing to perform a controlled glide to the ground from cruise altitude. To do this, only the critical systems such as actuators, lights and communications can be powered to perform an emergency landing. For a glide duration of 30 minutes, two lithium-ion batteries were sized to approximately 75 lb combined based on existing systems [42]. The electrical system and its major components are shown in Figure 56.

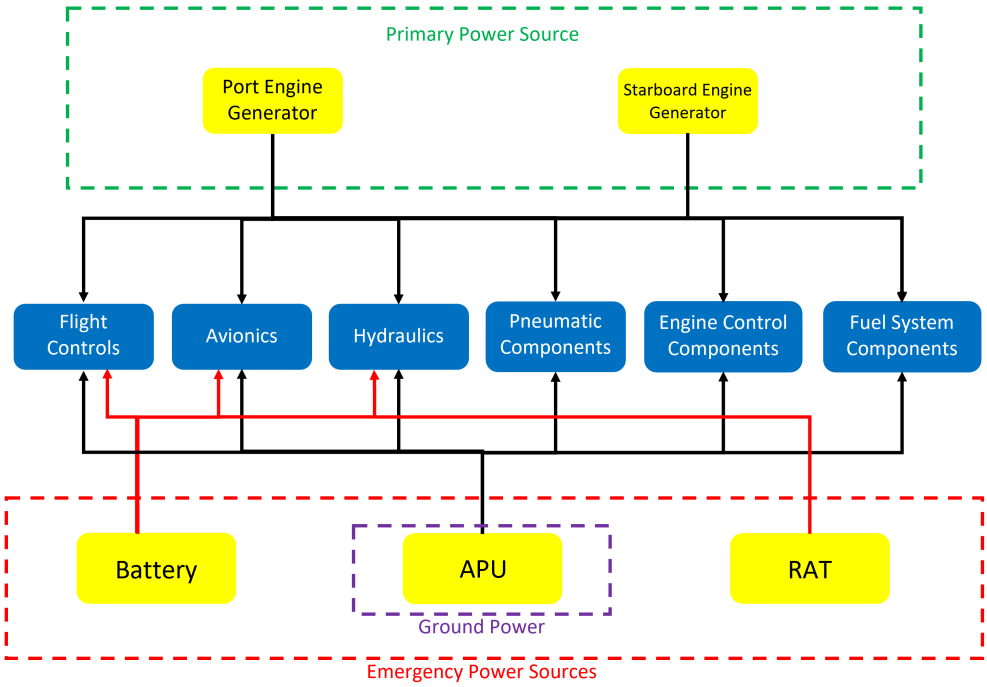

Figure 56: Aircraft Electrical System Diagram

11.4 Engine Control System

The aircraft engine control system is responsible for converting the pilot's input for a desired engine level into the appropriate actions inside the engine. The engine control system primarily deals with throttle input, bringing fuel into the engine, delivering the engine environment status to the pilot, taking in air data, monitoring engine health and starting and stopping the engine [43]. This aircraft will use a Full Authority Digital Electronic Control (FADEC) system, shown below in Figure 57 as the primary source of engine control. The FADEC, or engine control unit, takes in all of the input information, much like the flight computers in the flight control system, and provides the pilot's desired output. The engine control unit provides adjustments to parameters like the fuel flow rate and shaft rotation speed and presents the pilot with only the necessary information in order to reduce the amount of information that a pilot takes in. This allows the pilot to spend less attention on controlling the engine. The engine control unit also interacts with systems such as fire detection and temperature monitoring to track engine health or warn the pilot when something is wrong, using warnings through the instrumentation. The FADEC system is ideal for modern aircraft as it reduces the weight from mechanical linkage, as well as increases reliability and survivability due to the use of redundancies and the ability for the system to self-monitor [43].

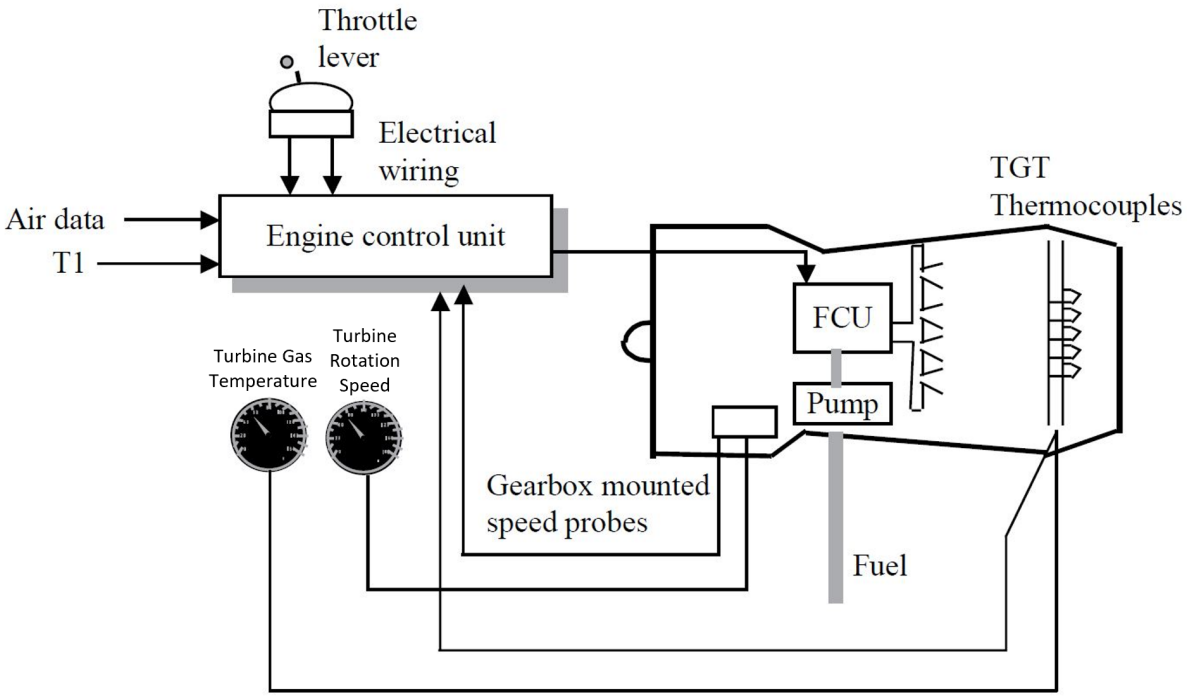

Figure 57: Aircraft Engine Control System Diagram

11.5 Hydraulic System

In this aircraft, the hydraulic system serves many functions such as wheel braking, front wheel steering, and control surface and high lift system actuation. Shown in Figure 58, the hydraulic system relies on a centralized hydraulic fluid reservoirs from which hydraulic lines flow. In order to create redundancies in the system, the two systems work independently to insure one failure does not eliminate hydraulic power. Other redundancies come in the form of multiple lines with shut-off valves and backup pumps in order to provide fail-safes and continuous hydraulic power to components. Due to aircraft operations, hydraulic fluid can get hot or cold and therefore, part of the hydraulic system involves maintaining safe operating temperatures. This is done by interacting with the heat exchanger.

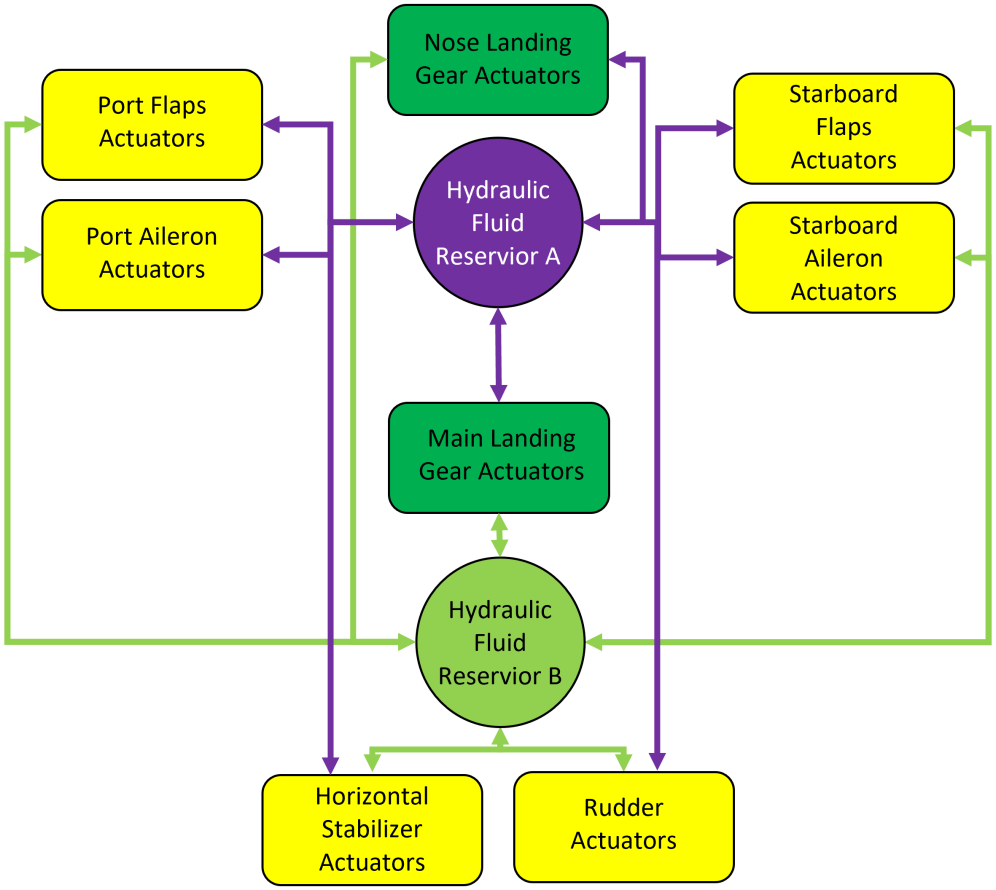

Figure 58: Aircraft Hydraulic System Diagram

11.6 Pneumatic System

The pneumatic system is the system that delivers air to different parts of the aircraft. Air is taken from outside the aircraft and fed through bleed air ducts connected to the engines. Then the air is distributed to the Environmental Control Unit and heat exchanger to be used for pressurizing the cabin, cooling various systems throughout the aircraft, and de-icing the aircraft. The diagram in Figure 59 shows how the pneumatic system is implemented in the aircraft. Adjacent to the pneumatic system is the Environmental Control System. This system provides a suitable environment to the pilots by controlling the temperature and pressure in the cabin, as well as providing supplemental oxygen if necessary. Additionally, it is necessary to control the temperatures that are experienced by some components such as the fuel, the engines, hydraulics, avionics, and the leading edges of the aircraft. This method of control revolves around the environmental control unit which takes RAM and bleed air in and distributes it out to the aircraft. Another main component of the environmental control is the heat exchanger which is used to either heat or cool air flowing through it.

A very important part in maintaining efficient and safe flight is to ensure the ice does not build up on the leading edges of the wings, tail, windscreen and on the propeller. This can be mitigated by passing warm air through channels in the leading edges which warms the skin of the aircraft and eliminates the ice buildup. Throughout pneumatic system, the flow of air is controlled by Shut-off Valves (SOV) and Pressure Relief Shut-off Valves (PRSOV) which are able to stop the air flow or control the pressure. The pneumatic system and the leading edge de-icing method are shown in Figures 59 and 60 respectively.

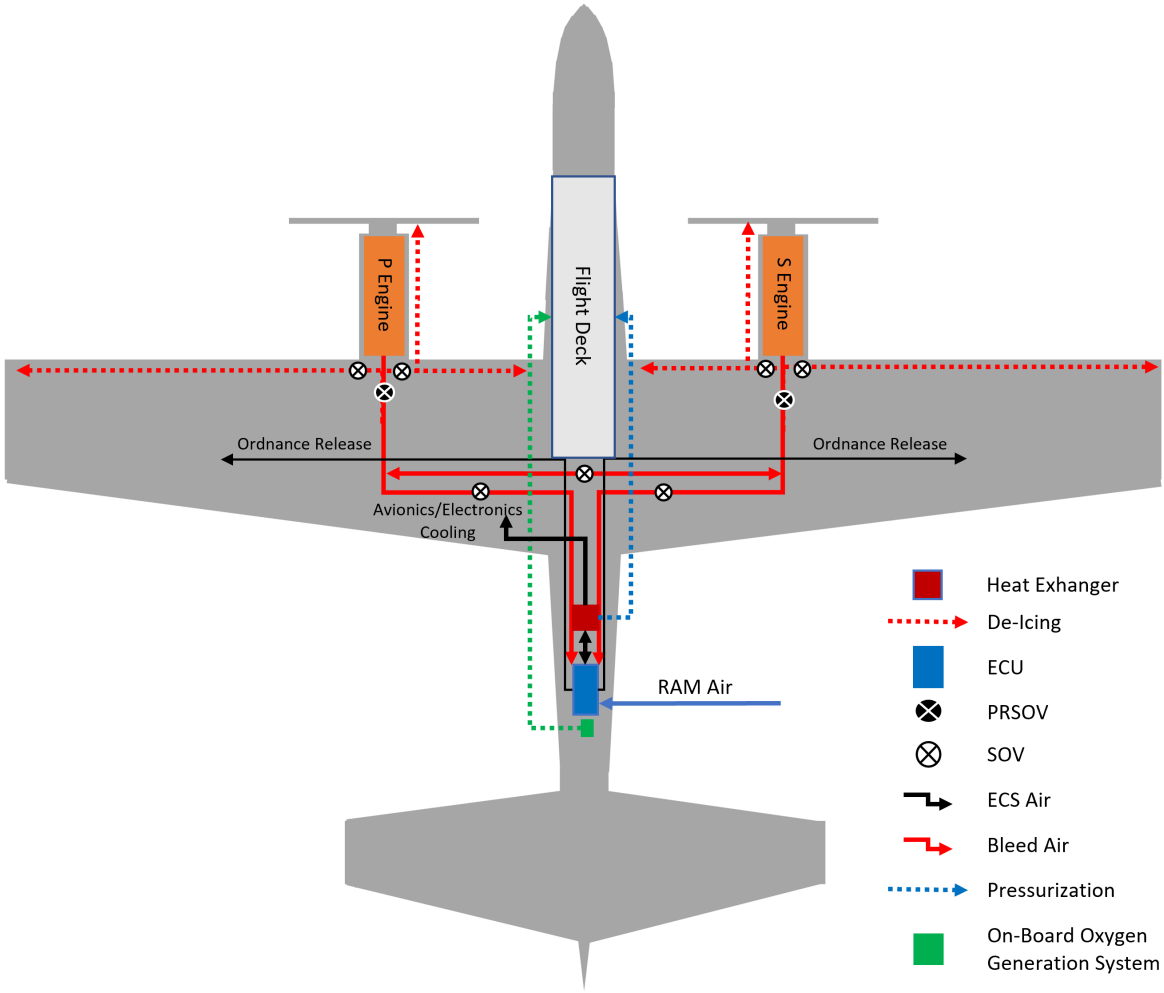

Figure 59: Aircraft Pneumatic System Layout

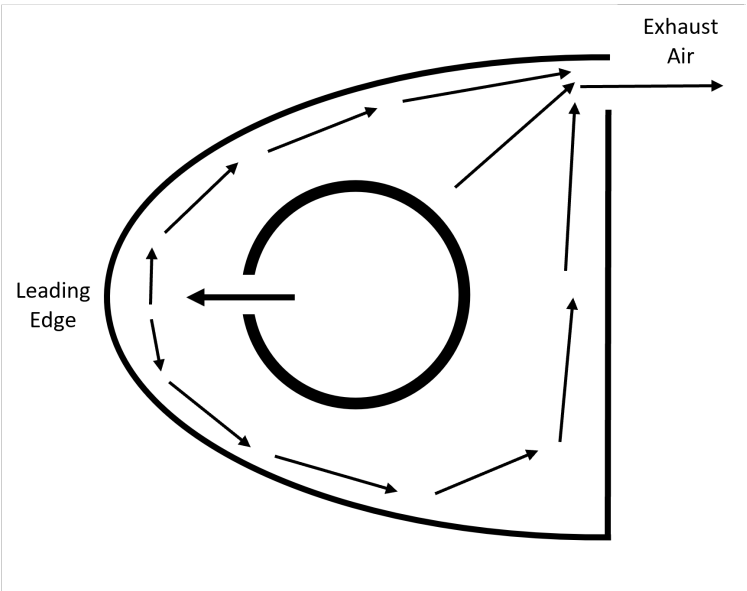

Figure 60: Aircraft Leading Edge De-Icing System Diagram

11.7 Emergency System(s)

Since there are only two occupants inside the aircraft, passenger egress protocols and systems are unnecessary and the primary emergency systems are the ejection seats. In the case that a pilot needs to evacuate the aircraft, installed ejection seats allow the pilot to safely evacuate the aircraft and away from potential harm. Reasons for needing to eject could be an eminent collision, loss of aircraft control or to escape any other danger that could cause loss of life. After conducting research on modern seats with such capabilities, the Martin Baker US16T seat was chosen as it has bottled emergency oxygen, fits inside the aircraft flight envelope, and is zero-zero capable [44]. This seat option was also chosen for the fact that it is already in service inside the T-38 Talon, a similarly sized, light aircraft.

Other emergency systems that will be included in the aircraft include fire prevention and suppression in the form of firewalls, temperature gauges and smoke detectors in the engine areas as well as areas with critical systems. Warning systems shall be used throughout the aircraft in order to effectively allow the pilot to identify potential failures. As a military aircraft, counter-measure systems will be used in the form missile warning systems aw well as chaf and flare launchers located at the wing tips.

Although it is not necessarily an emergency system, the crew boarding is conducted through the use of a telescopic boarding ladder that is housed in the fuselage, just behind the wing. Using this ladder, the pilot may step onto the wing and climb into the cockpit. To assist the forward pilot in boarding, an additional pop-out door will open and act as a step to get the pilot closer to their seat. The boarding ladder can be seen below in Figure 61.

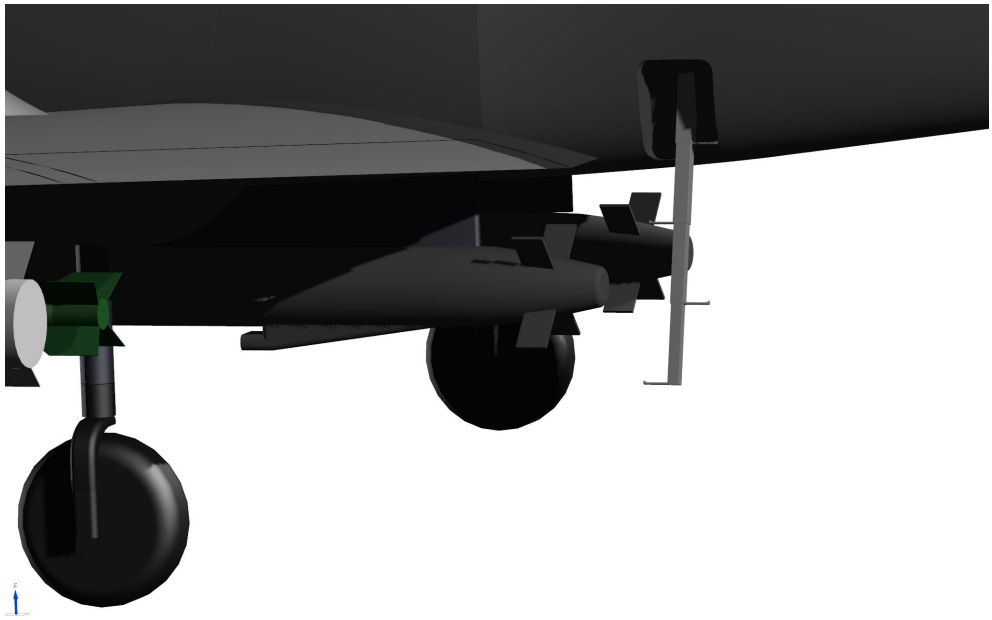

Figure 61: Telescopic Boarding Ladder

11.8 Avionics

To simplify the avionics integration within the aircraft, an avionics package was chosen. For this application the CMC Electronics Cockpit 4000 was chosen [45]. This avionics package features a modular glass cockpit that allows operators to customize instrument layouts and capabilities. An example of a possible cockpit/avionics layout is given in Section 4.5. The system is equipped with a primary flight display, tactical situation displays, and engine displays for pilot situational awareness. Additionally, the Cockpit 4000 is equipped with a stores management system and multiple air-to-ground and air-to-air targeting modes. For further combat situational awareness, the system is also capable of integration with a multimode Radar Warning Receiver (RWR).

11.9 Systems Certification Compliance

The systems that have been defined in this section have all been designed in order to meet the applicable certification requirements under MIL-STD-516C [46] which includes sections: 4.6.4, 6.1, 6.2.4.4, 7.2.4, 7.2.5, 8.1, 8.2, 8.3, 8.4, 8.6, 8.8, 9.1, 9.5, 12.1, 12.2 and 14. These sections coincide with certifications applicable to the respective systems design disciplines: configuration management, ice prevention, gas turbine engine application, hydraulic and pneumatic systems, environmental control system, fuel system, fire and hazard protection, auxiliary power and emergency power systems, mechanisms, escape and egress systems, life support, transparency integration, electrical power generation, electrical wiring, hazard/risk tracking and

subsystem protection. Upon further analysis and detailed design, these certifications have a high confidence of being met.

12 Ordnance

12.1 Ordnance Configurations

Choosing effective ordnance for the Gunbus aircraft is vital, as the purpose of the RFP is to design an aircraft that can support ground forces. The primary design constraint was the requirement for 3,000 lb of armament, with 500 lb being either rail launched missiles, rockets, or bombs. The secondary constraint was to include an integrated gun for ground targets. With these considerations, team Gunbus decided on multiple possible ordnance layouts to complete a variety of missions. These layouts are combined with an integrated gun and shown on the hardpoint diagram and in Table 46 below.

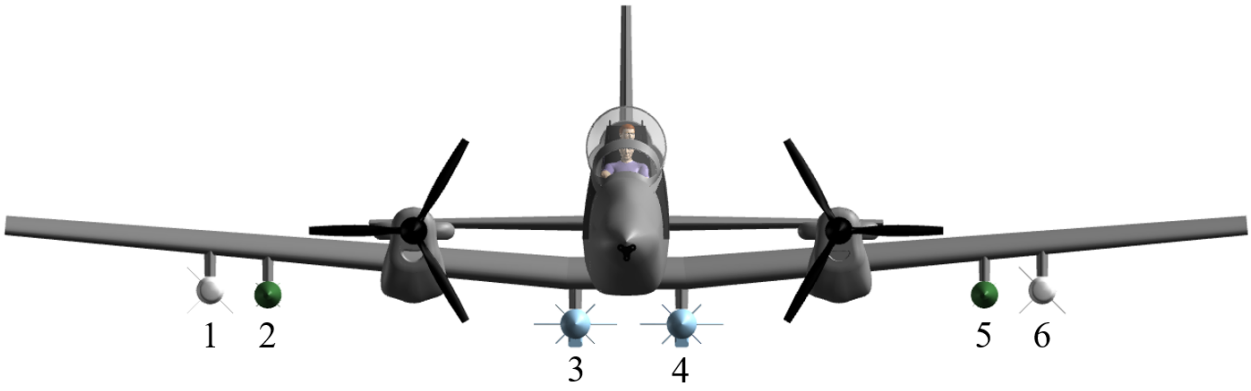

Figure 62: Hardpoint Identification

Table 46: Hardpoint Configuration Options

	Hardpoints					
Mission Type	1	2	3	4	5	6
Support (shown)	Maverick	MK-82	Delilah	Delilah	MK-82	Maverick
Attack	M3P	M3P	Delilah	Delilah	M3P	M3P
Bombing	M3P	MK-82	MK-82	MK-82	MK-82	M3P
Precision Attack	-	Delilah	Delilah	Delilah	Delilah	-
Hybrid	M3P	MK-82	Maverick	Maverick	MK-82	M3P

12.2 Ordnance Descriptions

The integrated gun is chosen to be the General Dynamics 20mm M-197 Gatling Gun with 750 rounds of ammunition [47]. This gun is chosen because it is lightweight, highly reliable, can be electrically or

hydraulically driven, and can fire in burst segments. The gun is placed at the nose of the aircraft, so the internal structure can withstand the 1,300 lb recoil force.

Next, the Delilah is a highly maneuverable, turbojet powered missile which can loiter prior to engaging targets [48]. This loiter ability fulfils the RFP requirement for the aircraft to complete some missions only a helicopter can. The aircraft can fly near a battle zone and release the Delilah missiles without having a locked on target. The missiles can cruise until a target is detected, and then proceed with attack. Helicopters today, including the UH-60 Blackhawk, are currently using the Delilah missile, proving its effectiveness in helicopter missions.

Additionally, wing mounted FN M3P .50-caliber machine gun pods are used in multiple ordnance configurations [49]. Each of these pods can carry 250 rounds of ammunition with three 70mm rockets. They are useful for engaging lightly armored vehicles and suppressing ground or aerial attacks. Plus, the ability to "soft mount" the pods onto the wing reduces fatigue stress and ultimately maintenance costs.

The other two pylon mounted ordnance options include the AGM-65 Maverick air to ground missile, and the MK-82 general purpose bomb. Both have extensive field history and are used on the Super Tucano. A summary of the ordnance options are shown in Figure 63.

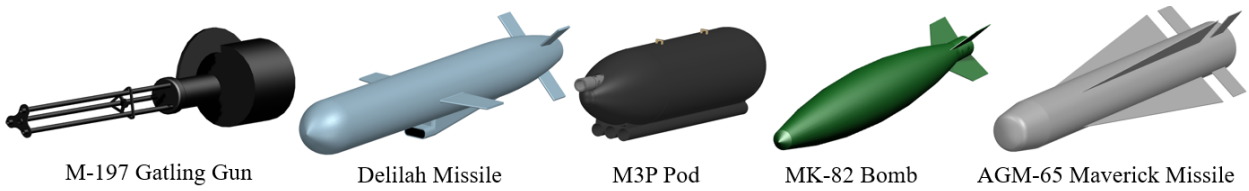

Figure 63: Ordnance Summary

12.3 Ordnance Mounting

Besides the integrated gun, all ordnance is pylon mounted and released through the use of pneumatic release systems that take air from the pneumatic system. Using pneumatic releases are better than small pyrotechnic explosions as it is reusable and reduces cost over the aircraft service life and reduces the amount of time to rearm the aircraft. It is also worth noting that every pylon is designed to support the weight and size of each ordnance option.

12.4 Future Ordnance

The missions of tomorrow will likely be different from today. One potential future ordnance option could be a modification of the AeroVironment Switchblade 600 loitering missile [50]. Similar to the Delilah missile, the Switchblade offers loiter capability prior to attack, but at a relatively light weight of 120 lb. One major

benefit would include the ability to carry more missiles and support ground troops for a longer time period. Plus, the ability to loiter would satisfy the requirement to perform similar missions to attack helicopters. The Switchblade could be easily integrated into the current pylon system. However, it is currently limited by its operating altitude and speed. Both would need to be addressed prior to usage on the Gunbus aircraft.

13 Acoustics and Survivability

13.1 Acoustics and Emissions

The engine that is being used in this aircraft configuration is the PT6A-135A, which is discussed above in Section 5. From the EASA noise level certification document the limits for take-off and overflight noise levels were listed as 88 dB and 80 dB. This engine meets the requirement noise levels as it produces 82.6 dB as it takes-off and 72.9 dB as it flies over [51]. Using the data provided from the United States Air-force [52], the estimated amount of carbon dioxide that will be emitted during the plane's life cycle is 65,880 US tons. The estimated amount of carbon monoxide that will be emitted is 5938 US tons.

13.2 Survivability

When designing the aircraft there were many considerations, such as redundancy, damage suppression, and armor placement, that are accounted for in order to increase the aircraft's survivability. When starting the design process, a twin engine configuration was chosen because it ensured that if one engine became inoperative, flight would still be possible. Additionally, three flight control computers will be unitized ensuring that if one were to fail, the aircraft would still be controllable. Lastly, for redundancy, multiple fuel pumps along with fuel valves will be used in case a fuel line or tank is breached [53].

In the case of fuel tank puncture, reticulated polyurethane foam will be used on the outside and inside of the fuel tanks to reduce possible damage by preventing an explosion and the spread of fire. The foam limits the mixture of air that is present in the fueling, leading to a lower probability of an explosion occurring. Furthermore, a fire suppression system, outlined in Section 11 will be used to contain and extinguish an on-board fire [54].

To protect key components on the aircraft from enemy fire, titanium armor will be placed around the cockpit, fuel tanks, flight control systems, and the engines. Located around the A-10 cockpit, this armor underwent testing and was able to weather strikes from a 23mm cannon and 57mm rounds. This aircraft will be agile enough to evade these firearms if they are not guided by radar. With this being said, the customer will be able to determine the armor thickness that is necessary for their desired use [55]. Additionally, a

stretched acrylic canopy will be used to ensure that the canopy will not shatter if struck by flying debris. The survivability of an aircraft not only ensures that the aircraft can maintain flight after taking damage, but that it can also avoid being detected by enemy technology [56]. In the sections found below, the different steps taken to ensure the long term survivability of the aircraft, in terms of the aircraft's susceptibility, are described.

13.2.1 Radar Signature

To reduce the radar signature of the aircraft, a gold tint, along with a indium-tin-oxide film layer, will cover the canopy. This will reduce the radar signature by preventing the radar signals from traveling through the canopy and into the cockpit [57]. This survivability method will not come standard in the aircraft configuration as it is an extra cost. If this meets the customers stealth needs, they may purchase it.

13.2.2 Infrared Signature

As of 2006, 60 percent of all combat aircraft losses resulted from infrared missile strikes [53]. With this statistic in mind it is extremely important to reduce an aircraft's infrared signature. For this aircraft, a key method in reducing the infrared signature is low emissivity paint. This paint decreases the thermal radiation that is emitted by the material which makes up the aircraft's skin. The paint, AMS-STD-595 36375, was selected because as shown in Figure 64, when compared to other low emissivity paint colors, it had the lowest emissivity over a variety of wavelengths [58]. This paint will be offered to the customer and will be utilized if they choose to include it. Additionally, to decrease the infrared signature of the aircraft a CIRCM system will be put beneath the fuselage. This system uses laser pulses to deter the infrared missiles from hitting the aircraft. Furthermore, a Missile Approach Warning (MAW) system will be implemented to indicate that a heat seeking missile was fired towards the aircraft and will give the pilot ample time to evade the incoming missile [59]. Lastly, flares and chaffs will be placed on the wing tips in order to help the pilot avoid heat seeking and radar guided missiles.

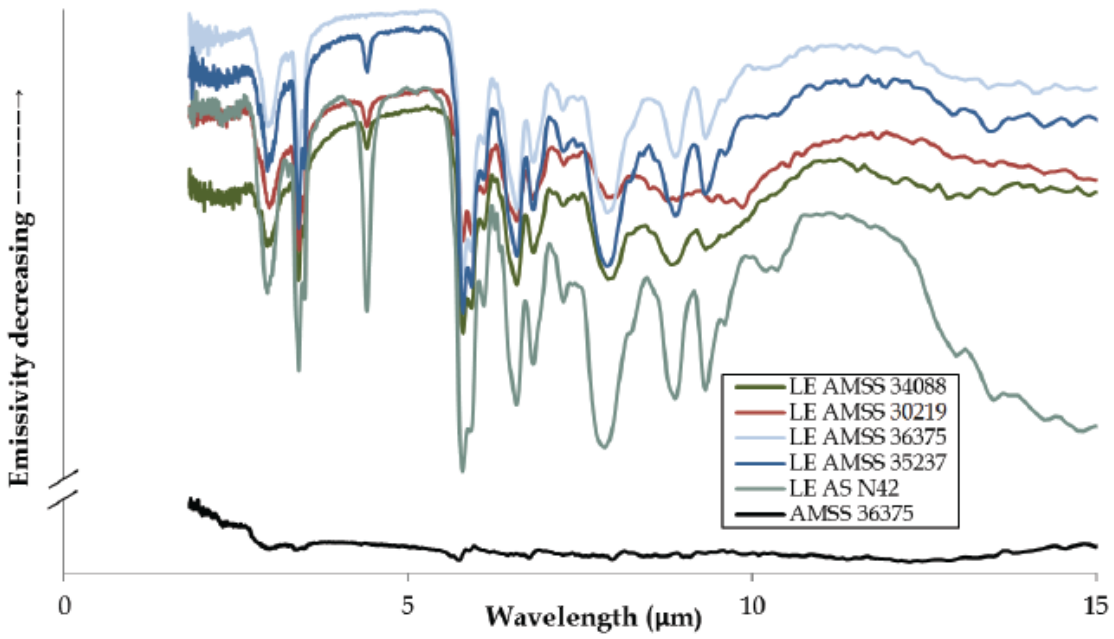

Figure 64: Emissivity of Different Paints

13.2.3 Visual Signature

Because this aircraft is being designed for low altitude support missions, it's visual signature is large. A way to reduce the visual signature is to carry out the missions at night. With lowered visibility at night, along with a decrease in the aircraft's radar and infrared signatures, the aircraft's survivability chances increase. Additionally, the mission profile can be adjusted to utilize the surrounding terrain to screen the visibility of the aircraft [53].

14 Cost Analysis

14.1 DACA IV Cost Model

The ticket price for the aircraft is $30,472,000. The breakdown is seen in Table 47. A starting production of 500 aircraft were chosen due to similar light attack aircraft models. Both the A-10 and A-29 have approximately 250 planes in service at any given point. The production is over the span of 5 years. Given a turn over rate of 50 planes a year, 500 production in a 5 year time frame would constrain the minimum amount of aircraft sold.

Table 47: DACA IV Cost Per Category

Engineering Hours	$239,720,000
Tooling Hours	$187,948,000
Manufacturing Hours	$1,013,000,000
Quality Control Hours	$13,216,000,000
Development Support Cost	$35,275,000
Flight Test Cost	$38,397,000
Materials Cost	$398,495,000
Engine Production	105,533,000
RDT & Flyaway Total	$15,236,000,000*
Per Aircraft Cost	$30,472,000

*For a production of 500 planes

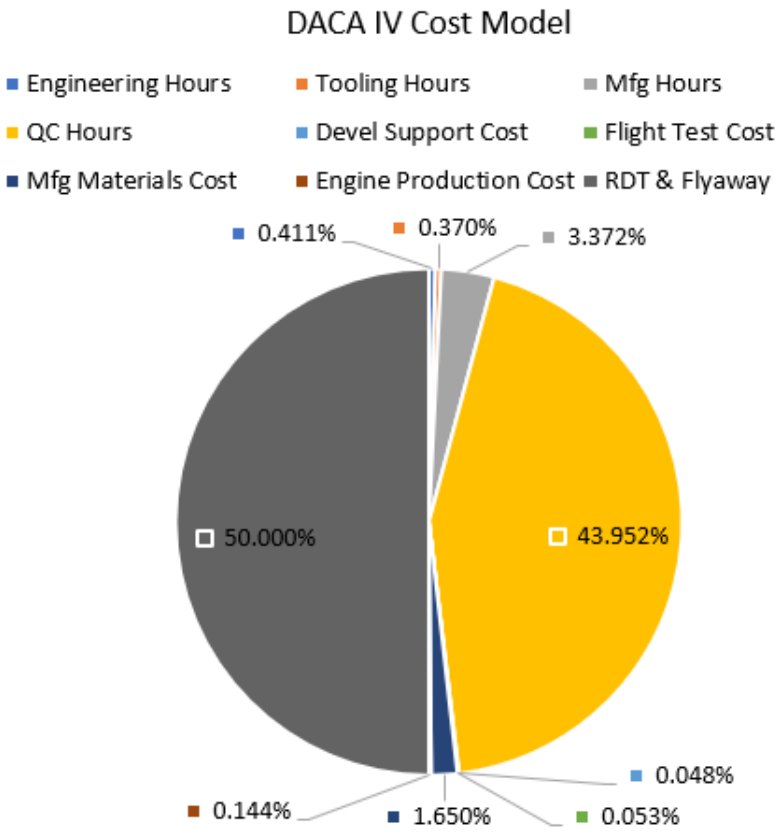

Figure 65: DACA IV Model Distribution

14.2 Production Cost

The number of production aircraft over a fixed time span has a large impact on cost per aircraft. As production increases, it is expected that the cost per unit is reduced. Data is shown in Table 48

Table 48: Unit Cost Based on Production

Units Produced	Cost per Unit
250	$35,548,000
500	$30,472,000
1000	$22,684,000

14.3 Comparison Model

While the DAVA IV model was primarily used for commercial vehicles, the breakdown per section cost comprised of relatively the same categories and held the same fraction of the overall cost. A direct comparison was done with the Carichner Nicolai cost model which focuses more on military aircraft. Most of the equations to calculate each section were similar and less aggressive when compared to the DACA IV model.

Table 49: Units Produced Cost per Unit

Units Produced	Cost per Unit
250	$22,961,000
500	$13,344,000
1000	$8,111,000

14.4 Direct Operating Costs

The average flight hours per year per aircraft is 400 for military aircraft. [22] Using engine SFC and average thrust used throughout the design mission, the cost of fuel per year for one aircraft is $715,000. The crew salary cost are estimated based on how many flight-crew members need to be kept on the active duty roster. As a preliminary calculation, the engineering hourly wrap-rates multiplied by 2,080 hours a year can be used to estimate the crew cost with the ratio of fighters as 1:1. The crew cost per member is $263,000 per member including a rough estimate for benefits and other costs outside of salary alone. With a crew of two, the yearly costs is $526,000. [22] Maintenance man-hours for military fighters average to 12.5 for every flight hour. The maintenance for flight hour can be estimated using the manufacturing cost per hour. The cost of maintenance is $490,000 a year. Table 50 shows the data calculated per different time intervals.

Table 50: Cost Estimates

Category	Per Year	Per Month	Per Hour
Fuel	$715,000	$59,500	$1,780
Crew Salary	$526,000	$43,800	$1,310
Maintenance	$490,000	$40,800	$1,220
Total	$1,731,000	$144,000	$4,320

14.5 Cost Reduction

Cost per unit can be reduced by producing more units in a shorter amount of time. Although the overall costs will increase, if the customer can sustain the higher costs, their cost per unit can be significantly reduced. The largest percentage of flyaway cost is quality control. If cost of quality control per hour is reduced, the cost per unit can be reduced significantly. The cost per flight hour can feasibly only be reduced through an increase in engine efficiency.

14.6 Uncertainties & Inaccuracies

Any model will face uncertainty and accuracy. This issue can be mitigated by referencing historical data for similar aircraft as the model develops. Another source of error is the performance parameters of the aircraft. If another discipline estimates a parameter incorrectly, error will be multiplied by the time it reaches the cost. The realistic way to prevent this is through numerous cycles of design iteration in the efforts of a converging accurate number or tests with modeling the aircraft.

15 Conclusions

At this stage in the design process, team Gunbus is confident in its ability to fulfill all requirements and objectives for the 2021 AIAA undergraduate design competition RFP. The Gunbus light attack aircraft features a low-wing, twin engine design which fulfils the requirements for payload capacity, takeoff and landing distance, and range. Key differentiators from similar aircraft include powerplant redundancy and ordnance loadouts with the capability of performing missions similar to those of attack helicopters, all while remaining affordable. Most importantly, the pilot is well protected through countermeasures, titanium cockpit armor, and zero-zero ejection seats for the worst case scenarios.

References

[1] Abbott, I. H., and von, D. A. E., *Theory of wing sections: incl. a summary of airfoil data*, Dover Publ., 1959.

[2] Lednicer, D., Sep 2010. URL https://m-selig.ae.illinois.edu/ads/aircraft.html.

[3] M., W., "The Case for Light-Attack Aircraft," , 2019. URL https://www.militarytimes.com/opinion/commentary/2019/10/29/the-case-for-light-attack-aircraft/, last accessed 16 February 2021.

[4] MilitaryTimes, "The case for light-attack aircraft," , 2019. URL https://www.militarytimes.com/opinion/commentary/2019/10/29/the-case-for-light-attack-aircraft/, last accessed 15 February 2021.

[5] Brodo, "MB-339 Basic Course," , 2021. URL https://www.openflightschool.de/course/view.php?id=139, last accessed 17 February 2021.

[6] Compare, A., "North American Rockwell OV-10 Bronco," , 2021. URL https://www.aircraftcompare.com/aircraft/north-american-rockwell-ov-10-bronco/, last accessed 17 February 2021.

[7] Rackley, D., "Giving History a Hand with Vintage Aircraft Restoration," , 2021. URL https://www.kcet.org/shows/blue-sky-metropolis/giving-history-a-hand-with-vintage-aircraft-restoration, last accessed 17 February 2021.

[8] Embraer, "Super Tucano," , 2021. URL https://defense.embraer.com/global/en/super-tucano, last accessed 17 February 2021.

[9] FAS, "https://fas.org/man/dod-101/sys/ac/a-10.htm," , 2016. URL http://w3techs.com/technologies/overview/content_language/all, last accessed 17 February 2021.

[10] SKYbrary, "FAIRCHILD A-10 Thunderbolt 2," , 2015. URL https://www.skybrary.aero/index.php/A10, last accessed 17 February 2021.

[11] HAL, "LCA," , 2021. URL https://hal-india.co.in/Product_Details.aspx?Mkey=54&lKey=&CKey=20, last accessed 17 February 2021.

[12] Nonothai, "Thai Military and Asian Region," , 2020. URL https://thaimilitaryandasianregion.wordpress.com/author/nonothai/, last accessed 17 February 2021.

[13] Gerzanics, M., "FLIGHT TEST: Upgraded Pilatus PC-12 powers ahead," , 2016. URL https://www.flightglobal.com/flight-test-upgraded-pilatus-pc-12-powers-ahead/120807.article.

[14] Federal Aviation Administration, "TCDS No. E4EA, Rev. No. 28, Pratt Whitney Canada Corp." , 2020. URL https://rgl.faa.gov/Regulatory_and_Guidance_Library/rgMakeModel.nsf/0/A263F0CCA46E0180862585AB005B6255?OpenDocument&Highlight=pratt,&,whitney,canada.

[15] Federal Aviation Administration, "TCDS No. E26NE, Rev. No. 17, Pratt Whitney Canada Corp." , 2020. URL https://rgl.faa.gov/Regulatory_and_Guidance_Library/rgMakeModel.nsf/0/9F350983B6694F4486258523005D478B?OpenDocument&Highlight=pratt,&,whitney,canada.

[16] Federal Aviation Administration, "TCDS No. E4WE, Rev. No. 34, Honeywell International Inc." , 2020. URL https://rgl.faa.gov/Regulatory_and_Guidance_Library/rgMakeModel.nsf/0/8552B469CED9E1E886257D310056EA65?OpenDocument&Highlight=tpe331-10.

[17] McCormick, B., *Aerodynamics, Aeronautics, and Flight Mechanics*, 2nd ed., Aerodynamics, John Wiley and Sons, Inc., 1995.

[18] "Gas Turbine Engines," , 2008.

[19] Federal Aviation Administration, "TCDS No. P15EA, Rev. No. 31, Hartzell Propeller, Inc." , 2020. URL https://rgl.faa.gov/Regulatory_and_Guidance_Library/rgMakeModel.nsf/0/5B8869AFEA22ABCB86258367005A438A?OpenDocument&Highlight=p15ea.

[20] of Technology, W. U., "Wing: Airfoil Selection," , 2014. URL https://itlims-zsis.meil.pw.edu.pl/pomoce/BIPOL/BIPOL_1_handout_8A.pdf, last accessed 30 April 2021.

[21] Carmen Sanchez, "Control Surfaces and High Lift Devices Modeling and Sizing Program," , 2018. URL https://www.icas.org/ICAS_ARCHIVE/ICAS2018/data/papers/ICAS2018_0627_paper.pdf, last accessed 15 March 2021.

[22] Raymer, D., "Aircraft Design: A Conceptual Approach, Sixth Edition," 2018. https://doi.org/10.2514/4.104909.

[23] Roskam, J., *Airplane Design Part VI: Preliminary Calculation of Aerodynamic, Thrust and Power Characteristics*, Vol. 6, Roskam Aviation and Engineering Corporation, 1987.

[24] ProsAndCons, "Pros and Cons of T-Tail," , 2019. URL https://prosancons.com/aircraft/pros-and-cons-of-t-tail/, last accessed 15 March 2021.

[25] Tom Benson, "Vertical Stabilizer," , 2021. URL https://www.grc.nasa.gov/www/k-12/VirtualAero/BottleRocket/airplane/rud.html, last accessed 15 March 2021.

[26] Air, "NACA 0009," , 2021. URL http://airfoiltools.com/airfoil/details?airfoil=n0009sm-il#polars, last accessed 15 March 2021.

[27] Air, "NACA 0012," , 2021. URL http://airfoiltools.com/airfoil/details?airfoil=n0012-il, last accessed 15 March 2021.

[28] Air, "NACA 0010," , 2021. URL http://airfoiltools.com/airfoil/details?airfoil=naca0010-il, last accessed 15 March 2021.

[29] Roskam, J., *Airplane Design Part II: Preliminary Configuration Design and Integration of the Propulsion System*, Airplane Design, Vol. 2, DARcorporation, 1997. URL http://gen.lib.rus.ec/book/index.php?md5=c9256c0d4fdb38b8493caf93189a23a9.

[30] Sadraey, M., *Aircraft Design: a systems engineering approach*, 1st ed., Aerospace, John Wiley Sons, Ltd, 2013.

[31] Dieter Scholz, "Wing Incidence Angle and Twist Estimation of the Current Box Wing Configuration," , 2011. URL https://www.fzt.haw-hamburg.de/pers/Scholz//Airport2030/Airport2030_M_BoxWing_IncidenceTwist_11-12-05.pdf, last accessed 15 March 2021.

[32] MIT, "Basic Aircraft Design Rules," , 2006. URL https://ocw.mit.edu/courses/aeronautics-and-astronautics/16-01-unified-engineering-i-ii-iii-iv-fall-2005-spring-2006/systems-labs-06/spl8.pdf, last accessed 15 March 2021.

[33] Roskam, J., "Airplane Design Part IV: Layout Design of Cockpit, Fuselage, Wing and Empennage," , 1989.

[34] Gabrian, "Aluminum Alloys: Get to Know its Properties and Uses," , 2020. URL https://www.gabrian.com/6061-aluminum-properties/, last accessed 17 February 2021.

[35] Reddy, G. J., "Mechanical Working of Aluminum–Lithium Alloys," , 2014. URL https://www.sciencedirect.com/science/article/pii/B9780124016989000070, last accessed 30 March 2021.

[36] Howe, D., "Aircraft Loading and Structural Layout," , 2004.

[37] Niu, M., "Airframe Structural Design," , 1988.

[38] Currey, N. S., "Aircraft Landing Gear Design: Principles and Practices," , 1988.

[39] Roskam, J., "Airplane Design Part IV: Layout Design of Landing Gear and Systems," , 1989.

[40] Sutherland, M. J., "Aircraft Systems: Mechanical, electrical, and avionics subsystems integration," 1968.

[41] Honeywell International Inc., "Micro Power Unit," , Unknown. URL https://aerospace.honeywell.com/en/learn/products/auxiliary-power-units/micro-power-unit, last accessed 10 March 2021.

[42] True Blue Power, "DHC-8 100 / 200 / 300 Series Certified Lithium-ion Aircraft Battery Upgrade," , 2020. URL https://www.truebluepowerusa.com/pdfs/TB44_DHC-8Brochure.pdf.

[43] Seabridge, A., *Aircraft Systems: Mechanical, electrical, and avionics subsystems integration*, 3rd ed., John Wiley Sons, Ltd., 2008.

[44] Martin-Baker Aircraft Co., "MK16 EJECTION SEAT FOR T-6 TEXAN II," , 2017.

[45] "Products amp; Services," , ???? URL https://cmcelectronics.ca/productsservices/cockpitsystemsintegration/cockpit4000.aspx.

[46] "MIL-HDBK-516C - Department of Defense Handbook: Airworthiness Certification Criteria," , 2014.

[47] General Dynamics, 2014. URL https://www.gd-ots.com/armaments/aircraft-guns-gun-systems/m197/, last accessed 15 March 2021.

[48] IMI Systems, 2016. URL http://www.imisystems.com/wp-content/uploads/2017/01/delilah.pdf, last accessed 15 March 2021.

[49] FN America, 2021. URL https://fnamerica.com/products/fn-airborne-pod-systems/fn-rmp/?referrer=military, last accessed 15 March 2021.

[50] AeroVironment, "Switchblade 600 Loitering Missile," , 2020. URL https://www.avinc.com/images/uploads/product_docs/Switchblade_600_FutureState_Datasheet_11042020.pdf, last accessed 29 April 2021.

[51] EASA, "EASA certification noise levels," , 2020. URL https://www.easa.europa.eu/domains/environment/easa-certification-noise-levels, last accessed 15 March 2021.

[52] Wade, M., "Emissions Measurement Program Study," , 2002. URL https://apps.dtic.mil/dtic/tr/fulltext/u2/a412301.pdf, last accessed 29 April 2021.

[53] Nicolai, L., *Fundamentals of Aircraft and Airship Design*, Aircraft Design, Vol. 1, American Institute of Aeronautics and Astronautics, inc., 2010.

[54] Donald Nieser, "Deterioration of Explosion Suppressant Fuel Tank Foam Revisited," , 2010. URL https://www.mydigitalpublication.com/article/Deterioration+of+Explosion+Suppressant+Fuel+Tank+Foam+Revisited/351824/34476/article.html, last accessed 15 March 2021.

[55] Warcosts, "Fairchild Republic A-10 Thunderbolt II," , 2012. URL http://www.warcosts.net/wp-content/uploads/us-navy/417JZ_1_2012_U.S._Air_Force_A_10_Thunderbolt_II_Wikipedia_Website_May_23_2012.pdf, last accessed 15 March 2021.

[56] MECAPLEX, "Aircraft and helicopter glazing," , 2021. URL https://www.mecaplex.ch/en/transparencies.html, last accessed 15 March 2021.

[57] Stijn Vanhauwaert, "F-16 Rear Canopy," , 2021. URL http://www.aviation-collector.be/F-16_rear_canopy.html, last accessed 15 March 2021.

[58] Lance Kelly, "Low-Emissivity Topcoats for the Reduction of Thermal Infrared Emissions from Military Platforms," , 2020. URL https://www.paint.org/coatingstech-magazine/articles/low-emissivity-topcoats-for-the-reduction-of-thermal-infrared-emissions-from-military-platforms/, last accessed 15 March 2021.

[59] Kamal Chopra, "A Short Technical Note on the IR Signatures Studies and Designing Aspects of the IR Technology Devices for Defence Aircraft," , 2020. URL https://www.longdom.org/open-access/a-short-technical-note-on-the-ir-signatures-studies-and-designing-aspects-of-the-ir-technology-devices-\\for-defence-aircr.pdf, last accessed 15 March 2021.